Design and Metrology of a Precision XY Planar Stage

by

Jeffrey Michael Gorniak

A thesis
presented to the University of Waterloo
in fulfillment of the
thesis requirement for the degree of
Master of Applied Science
in
Mechanical Engineering

Waterloo, Ontario, Canada, 2010

AUTHOR'S DECLARATION

I hereby declare that I am the sole author of this thesis. This is a true copy of the thesis, including any required final revisions, as accepted by my examiners.

I understand that my thesis may be made electronically available to the public.

Jeffrey Michael Gorniak

Abstract

In recent years, the manufacturing industry has seen an increase in demand for micro-components in biomedical, opto-mechatronics, and automotive applications. Traditional machine tools are no longer a viable solution to meet the tolerances required by the customers. Hence, new ultra-precision machine tools have emerged with nanometer level accuracy in response to these demands. This thesis presents a novel ultra-precision machine tool with the intent to bridge the gap between traditional machine tools with larger work volumes and lower accuracy, and ultra-precision machine tools with high accuracy and small work volumes. The machine was designed using a T-type gantry and worktable configuration with a precision ground granite base, to achieve a work area of 300x300 mm^2, with a maximum velocity of 1 m/s and a maximum acceleration of 10 m/s^2. Actuation is provided by direct drive linear motors with high resolution feedback supplied by 4 μm grating linear encoders with 4096x interpolation. Aerostatic porous bearings are employed to reduce the effect of friction while maintain high stiffness of the guideways and structure. A Vacuum Pre-Loaded (VPL) air bearing supports the worktable on the granite, decoupling vertical load from the gantry. Thermal error reduction is achieved using environmental temperature control (20 ± 0.2°C) to help reduce thermal errors. As well, internally cooled couplings were designed to remove heat generated by the motors, thus further reducing the effects that contribute to thermal error.

The target static stiffness of the machine was 50 N/μm and was measured to be 22.2 N/μm and 23.9 N/μm in the x and y axes respectively. Frequency response experiments were used to identify the open-loop transfer functions for each axis. A multivariable framework was implemented for the y-axis due to the cross coupling between the primary and secondary motors of the gantry. Two prominent vibration modes were identified at 68 Hz and 344 Hz. The first mode is attributed to the rigid body yaw mode of the gantry while the higher frequency is related to the bending mode of the beam. The first mode of the x-axis is seen at 220 Hz. A state space, active mode compensation control law was developed for the y-axis, in collaboration with Mr. Daniel Gordon, which eliminates the effects of the 68 Hz mode, allowing for high performance from the motors. The following error during a high speed (200 mm/s) test was measured at 2.74 μm and 2.41 μm in the x and y axes respectively.

Metrology tests using laser interferometry were performed in accordance with international and American metrology standards for linear positioning, vertical and horizontal straightness, and yaw and pitch errors. The results will be used for geometric error compensation in future work. Finally, an overall error budget is presented with focus on the geometric, dynamic, servo, and thermal errors,

where the maximum static resultant error of the machine was estimated to be 1.44 μm, and the maximum dynamic resultant error of 3.69 μm.

Acknowledgements

This research is supported by the Canadian Foundation of Innovation (CFI), AUTO21, and the Ontario Ministry of Research and Innovation granting agencies in Canada. Industrial contributions were provided by New Way Precision, Heidenhain, ETEL, and Rock of Ages.

A special thanks to the machinists who provided quality products, valuable manufacturing lessons, and guidance in the design of the machine. I would specifically like to mention the help of Mr. J. Benninger and Mr. R. Wagner who not only assisted in every way possible, but were always there to provide valuable insight to the machine's design, as well as a good laugh. Thank you for all your help gentlemen.

D. Gordon contributed to Chapter 4 with material from his Masters research in mode compensating controller design.

I owe a lot of gratitude to Dr. Alkan Donmez, Dr. Shawn Moylan as well as many others at the National Institute of Standards and Technology (NIST) for Chapter 5. Thank you for all your help in machine tool metrology.

Thank you to Prof. F. Ismail and Prof. S. Lambert for reading this thesis and providing valuable feedback.

And finally, I would like to thank my supervisor, Prof. K. Erkorkmaz. His devotion to research and the success of his students is seen is everything he does. There are few words that can fully express my gratitude for his guidance and the experience he has provided over these past years. Thank you.

Dedication

To my parents and Elisa.

†

Table of Contents

List of Figures

List of Tables

Chapter 1

Introduction

The manufacturing industry has seen a growing demand for precision components in recent years. Biomedical devices, automotive components and micro-optical moulds are some examples of these precision manufactured components. Traditional milling practices have reached the limit of the machines' accuracy and cannot achieve the high tolerances now demanded in the micro-machining field. In parallel with this limitation is the ability to machine complex three-dimensional surfaces of micro components. These limitations coupled with the high demand from industry have created a need for new multi-axis ultra-precision machine tools capable of creating complex geometry while achieving the difficult tolerances required.

Typically, machine tools can achieve positioning accuracies on the order of tens of microns or even microns. The new tolerances require positioning accuracies 100x more accurate, which is tens o hundreds of nanometers. To achieve nanometer accuracy, machine designers need to identify the sources of error and develop solutions to eradicate or minimize their effects. Previous research has highlighted several key areas which yield the highest level of error for precision machines [1]. The effect of thermal variation of the machine's structure, as well as its environment, incorporates a large amount of uncertainty in the position of the cutting tool relative to the workpiece. Thermal error alone has the potential to yield parts which are beyond the specified tolerances for a micro-component. By removing the heat generated from sources such as the cutting process, electric motors, friction, and environmental changes, the repeatability of the machine will improve and positioning uncertainty reduced.

Another source of error is the mechanical error of the guideways for a machine. The goal is to move the tool in a specified motion without deviating from its desired path. However, all guideways will contain some amount of error. There are several methods to minimize this error. One offline method is to map all geometric errors within the work volume of the machine tool and record the repeatable mechanical error [1]. Once the map is known, the toolpath can be shifted according to the map to compensate for the error. A metrology frame is an example of an online compensation technique, where positional deviations from the ideal location are measured in real-time. The reference position is adjusted to compensate for the measured error, thus, applying active geometric compensation [1].

To obtain a high dynamic response from the machine, the system must be designed for high stiffness for several reasons. The first is to reduce the flexibility of the machine structure, which causes positioning errors and is difficult to measure and compensate. The second is to shift vibration resonances to a range of frequencies that will not be affected during normal operation of the machine. It is a challenge to design a machine with high stiffness while keeping the mass and size of the machine at an acceptable level. Precision machine design principles can be used to increase the stiffness and improve the dynamics of the machine [1]. However, once the machine is built, it is natural for vibrations to still occur. The drive system, with advanced control algorithms, can be used to actively dampen the vibrations.

The objective of this research is to develop a novel 5-Axis ultra-precision machine tool for the micro-machining industry to create products such as micro-optic moulds, impellers for continuous flow heart pumps and Micro-Electrical-Mechanical-Systems (MEMS). However, due to the size of the project, the scope of this thesis will focus on the design, metrology, and controller design for two linear, orthogonal axes which comprise the planar stage of the machine. The proposed planar stage will be the base of the machine to which the remaining linear and two rotary axes will be attached. The machine is required to have a larger work area than most precision machines with greater dynamic capabilities. However, its positioning accuracy should be on the same order as previous precision machines, which were around 10 – 100 nm. Cutting loads during a micro machining process are expected to be no more than 20 N, which should not induce errors greater than 0.4 μm. Therefore, the target stiffness of the stage should be greater than 50 N/μm.

Chapter 3 discusses the design of the stage, as illustrated in Figure 1-1, which consists of a gantry and worktable configuration commonly seen with Coordinate Measurement Machines (CMM) where a linear guideway is present on one side of the gantry with a bridge extending over the work area (300x300 mm^2) of the machine.

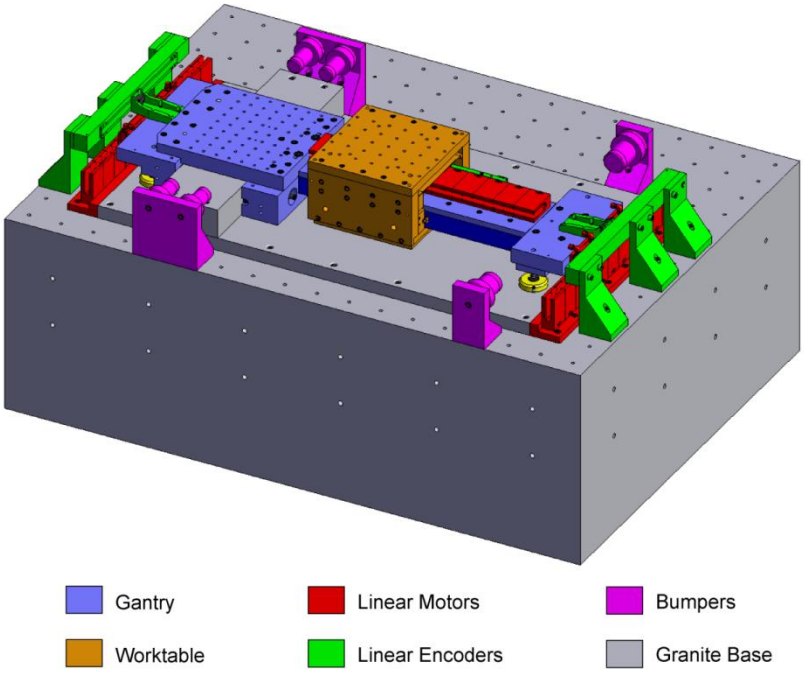

Figure 1-1. Conceptual design of the precision stage

The bridge is orthogonal to the granite guideway and performs as a subsequent guideway for the worktable. The weight of the worktable is traditionally supported by the gantry bridge, which leads to deformation of the beam. This can cause positioning errors and decrease the stiffness of the machine. Alternatively, a Vacuum Pre-Loaded (VPL) air bearing, commonly seen with photolithography machines, is used to support the worktable on the granite base of the machine. The granite is precision ground to accommodate the flatness of the VPL. The underside of the VPL consists of a pneumatically pressurized region which lifts the worktable off the surface, while a vacuum region preloads the bearing to the granite. This produces a stiff design which is resistant against vertical and pitch loads. Another desired effect of the VPL is the negligible coefficient of friction between itself and the granite. Aerostatic bearings are used to support the gantry on the granite base, and by preloading the bearings, a high stiffness design with a negligible friction effect is achieved. To realize high dynamic performance, direct drive linear motors are used to actuate the axes which will accelerate the stage at 10 m/s^2 to a maximum speed of 1 m/s. To reduce flexibility of the gantry and actively compensate for structural vibrations, two motors are used to actuate the gantry located at opposite ends of the beam.

Control laws are developed in Chapter 4 to position the stage with sub-micron to nanometer level accuracy while also providing robust tracking performance during high transient motions. A multivariable control law framework was used for the y-axis due to the cross coupling dynamics

between the two gantry motors. Identification of system parameters was completed by a Frequency Response Function (FRF) measurements, which pass open loop sine wave inputs to the motors and measures the relative magnitude and phase of the output from the encoders. These tests also helped to identify the resonance frequencies and aided in advanced controller designs.

In Chapter 5, quasi-static metrology measurements are collected to map the geometric errors of the stage. A laser interferometer was used to measure the linear positioning, vertical and horizontal straightness as well as yaw and pitch rotational errors. The measured repeatable errors can be used to improve the accuracy of the machine through geometric compensation.

Chapter 6 presents the conclusions of the thesis along with a final error budget and future work for the project. Recommendations are listed for future design considerations.

Chapter 2

Literature Review

2.1 Introduction

This chapter presents a review of literature and industrial state-of-the-art in the areas of precision machine design and machine tool metrology. Section 2.2 presents the principles of precision design with its implementation on machine tools. Machine tool metrology using laser interferometry techniques are defined and their principles of operation are explained in Section 2.3. Conclusions for the chapter are presented in Section 2.4.

2.2 Precision Machine Design

Precision machine tools have become highly prominent in manufacturing practices to alleviate the demand from industry for complex micro-components. Traditional machine tools have reached their limit in terms of accuracy (1 μm). Hence, new machine tool designs were required to satisfy the new fabrication tolerances. In response to this demand, researchers successfully developed ultra-precision machines capable of nanometer level accuracy [2], [3], [4], [5]. Additionally, commercial designs of precision machines were built, which offered a practical solution for achieving high accuracies [6], [7], [8], [9]. A common denominator to all designs is the reduction of errors such as geometric, thermal, and friction, while maintaining high stiffness of the structure.

Geometric error is comprised of error in the machine's guideways, drive system such as ball-screws and timing belts, and misalignment of components. This results in positional deviations of the workpiece or tool tip, leading to errors during the machining process. These errors are often predictable due to their mechanical nature and can be reduced by using proper compensation techniques. A guideway for a machine tool is often precision ground or hand scraped, and is capable of maintaining a straightness error less than one micron over a distance of 1 m. However, if nanometer level accuracy is desired, compensation of geometric error can reduce the guideway error to nanometer levels [1], [10]. Further explanation of geometric error compensation by laser interferometry is explained in Section 2.3. Drive systems which include ball-screw drives, timing belts, and mechanical bearings are prone to geometric errors. Lead error of ball-screws is periodic and is dependent on the quality of the groove on the shaft. Compensation of the lead error was performed by Kamalzadeh by comparing the rotational position of the drive motor and the linear displacement of

the work table [11]. A sinusoidal error emerged with a period identical to that of the ball-screw. A model-based compensation was used to predict the error and adjust the trajectory input accordingly. However, future changes to the drive system setup would require a re-measurement of the lead error, which can be time consuming and not practical. Ironless direct drive linear motors are a popular alternative to actuating machine tools, due to their minimal cogging effect and absence of lead errors [4], [12], [13]. They also provide a non-contact, high dynamic response over large travel ranges. Shinno et al. used voice coil motors to actuate an X-Y Planar Motion Table System, which was capable of positioning the table within one nanometer and providing high stiffness during cutting tests [2]. However, voice coil motors have limited range of travel, only 10 mm for the motion system in [2].

One of the largest sources of error for a precision machine is thermal error. Fluctuations or gradients in temperature of a machine's components cause materials to expand and contract, causing positioning errors. Temperature throughout the machine is difficult to measure, since it can be different at various locations, and is even more difficult to predict. Research studying the thermal properties of machine tools has been widely studied [1], [14]. It was found that regulating the temperature of the environment reduced changes in the machine's temperature, thus increasing the repeatability of the machine. The material to build the machines has also been analyzed. Materials that have low or negligible coefficients of thermal expansion, such as Invar or Zerodur, expand less under similar temperature conditions than regular engineering materials like steel or aluminum [15]. For example, a 1 m piece of steel will expand 12 μm for every 1°C increase of temperature. Invar will expand only expand 1.3 μm in the same scenario. However, Zerodur and Invar are higher in cost and are not practical for the average machine shop. Therefore, more emphasis is directed to controlling the temperature of the environment and the machine. A major source of thermal energy is produced by the electric components of the machine, such as the servo motors, and mechanical components, for instance the ball-screw nut interface or roller bearings. Some servo motors are now supplied with the option of liquid cooling channels which surround the motor and remove thermal energy [16]. The heat generated by roller bearings is created from the friction of the rollers against the guideway or raceway.

Friction is a difficult effect to predict and compensate, due to its non-linear nature. Its compensation requires accurate modeling, which in servo control practice can be achieved using a disturbance observer [2], [17]. Another disadvantage of friction is the creation of heat during motion, causing the guideways to expand or warp leading to larger, less repeatable positional errors. It is common practice for machine tool operators to perform a warming routine in order for the machine to reach thermal equilibrium [1]. Aerostatic bearings are often used to reduce or even remove friction as

shown in [3], [18]. A thin, pressurized film of air between the bearing and guideway create a nearly frictionless ($\mu \sim 10^{-5}$) contact, while maintaining high stiffness. Typical roller bearings have a friction coefficient of $\mu \sim 10^{-3}$. In parallel with aerostatic bearings are hydrostatic bearings, which use a thin film of oil between the bearing and guideway. They provide higher stiffness than aerostatic bearings; however it can be difficult to control the oil flow and leaks. Aerostatic bearings are much cleaner, environmentally friendly and economical. They are commonly used in CMM and photolithography machines, since they are ideal for clean room and high accuracy applications. A disadvantage to aerostatic bearings is their unidirectional stiffness. To achieve bidirectional stiffness, a preloaded air bearing arrangement is used. Recently, a new type of aerostatic bearing was designed, which uses vacuum pressure between the bearing and the guideway along with the pressurized air to create two counteracting forces. Such bearings are called Vacuum Pre-Loaded (VPL) bearings and have high bidirectional stiffness properties [19]. As well, the air gap between the bearing and guideway can be controlled by adjusting the two pressures. VPL technology was used by Shinno to provide a vertical stiffness of the machine of 84 N/μm [20]. VPL technology is also seen in photolithography machines to support and accurately position ∅300 mm Silicon wafers.

Cortesi developed a single axis drive system with many of the principles mentioned above [21]. The Axtrusion machine, as seen in Figure 2-1, uses a precision ground granite base, aerostatic bearings, and a direct drive linear motor. The machine has a range of 320 mm.

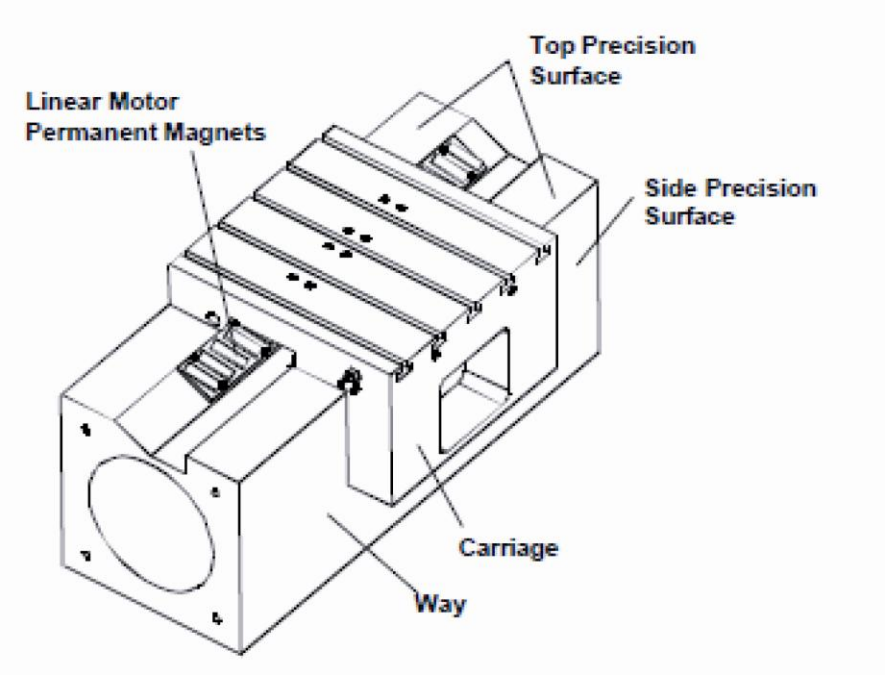

Figure 2-1. Axtrusion machine schematic [21]

The linear motor has a dual purpose as it provides linear positional actuation, as well as a preloading force for the air bearings. The motor is angled such that the vertical and horizontal force it applies preloads the bearings to achieve the recommended fly height for the air bearings. The average vertical stiffness was measured to be 422 N/µm.

Shinno developed an XY positioning table using an alumina ceramic base with 5 vacuum preloaded aerostatic bearings, and 8 voice coil motors [2]. The schematic of this machine is shown in Figure 2-2.

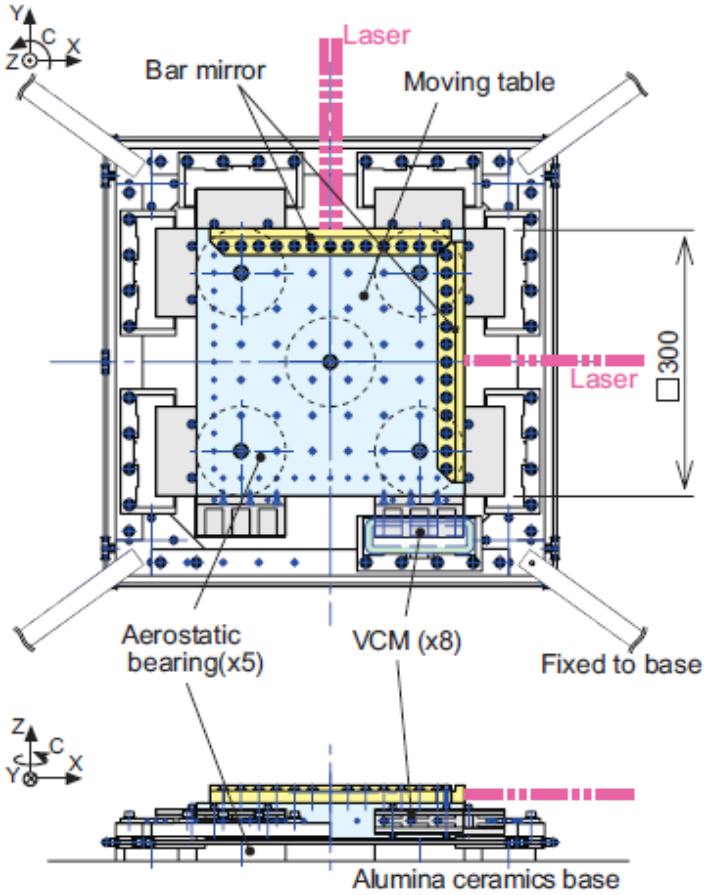

Figure 2-2. Precision XY Stage with nanometer positioning [2]

The machine has a work area of 20x20 mm^2 with a maximum acceleration of 1.6 m/s^2. The vertical stiffness is 191 N/µm and is capable of 1 nm positioning in both axes. Sub-nanometer resolution is achieved by laser encoders and plane mirrors, that are located such that measurement errors is negligible. The coils of the motors are located on the base to minimize thermal energy from reaching the stage. The stage is in a non-contact environment, thus removing any non-linear effects. Cutting tests of Tungsten Carbide (WC) at 1mm/s were performed with tracking errors during cutting of 2 nm and 5 nm in the x and y axes, respectively. The remarkable results show the high accuracy potential for ultra-precision machines.

CMM machines are known for their sub-micron positioning capabilities. They are required to be accurate and highly repeatable in order to verify tolerances of a component are within their specification. An example of a CMM is shown in Figure 2-3.

Figure 2-3. Example of T-type CMM machine [22]

The CMM above has a T-type gantry design with a guideway on one end and the gantry beam extending over the workspace. The beam of the gantry operates as a guideway for a second axis. Actuation of the gantry is provided by one motor next to the guideway on the base.

A XY stage was developed by Heidenhain at the National Institute of Standards and Technology (NIST), which consists of a XY grid encoder and voice coil motors. Figure 2-4 shows a picture of the stage. The encoder head is located directly in line with the tool above the worktable (not shown in the figure). The motors actuate near the center of mass of the stage, causing minimal moment loads. The intention of the design is to minimize Abbe errors.

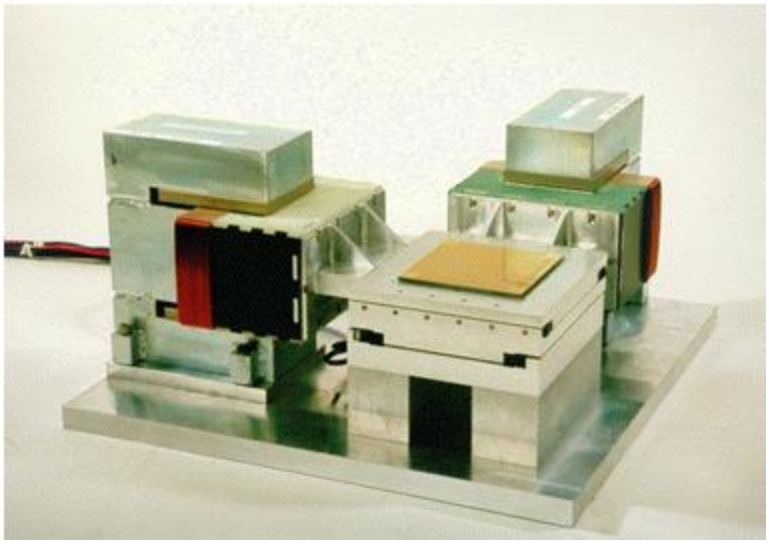

Figure 2-4. XY stage designed to minimize Abbe error [23]

The stage has a work area of 50x50 mm^2 and uses cross-roller bearings and rails as guideways. The machine shows the potential for larger work areas while maintaining high positioning accuracies.

2.3 Machine Tool Metrology

Metrology of machines tools is common practice to measure the mechanical accuracy of a machine. It provides the user with detailed information about the actual location and orientation of the machine throughout its work volume. This information is highly valuable to both the machine tool builders and customers for various reasons. The builder can provide the results of the measurements to authenticate the accuracy of their machine and provide this to a customer as a confirmation of the machine's accuracy. The customer is able to compare different machines and review the metrology results of each machine and use their engineering judgment when deciding which machine to use for their application. Most customers look for an overall accuracy value called the *volumetric error*, as explained in [24], for a machine as a simple yet effective way to compare each machine. However, there are many measurements required to calculate this value. The international machine tool metrology standard ISO-230-1 [24] along with ASME B5.54-2005 [25] are used for definitions, terminology and analysis methods.

For each axis, there are six degrees of error; three linear and three rotational error motions. For multi-axis machines, an additional error value is included, which is the angular deviation from the desired orientation between each axis. For a two-axis planar stage, there exist 13 error motions: six linear errors, six rotational errors, and one orientation error. The definition of each error is dependent on the direction of travel and its relation to the machine's coordinate frame. The linear errors are defined as linear positioning displacement, horizontal straightness and vertical straightness. The

rotational errors are defined as yaw, pitch and roll. Since a machine's axes are typically setup to be orthogonal to each other, the orientation error of axes is often called the squareness error. The following figure outlines the error definitions for a single axis.

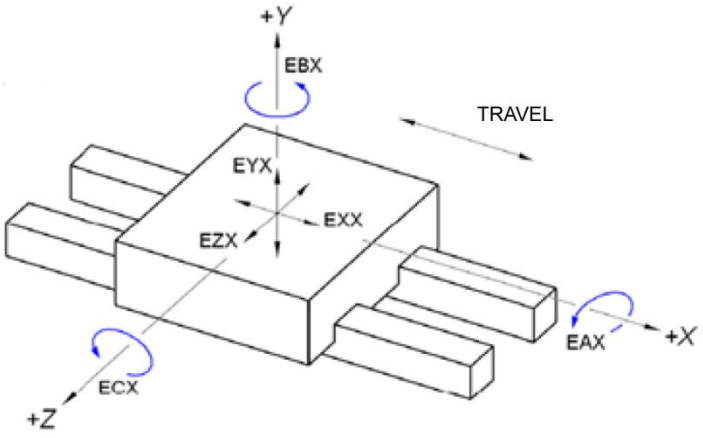

Figure 2-5. Error Definitions [24]

Where

EAX angular error motion around A-axis (Roll)

EBX angular error motion around B-axis (Yaw)

ECX angular error motion around C-axis (Pitch)

EXX linear positioning error motion of X-axis positioning deviations of X-axis

EYX straightness error motion in Y-axis direction

EZX straightness error motion in Z-axis direction

Laser interferometry is an accurate and reliable method for machine tool metrology and is used for the measurements presented in Chapter 5. The laser interferometer uses a beam with a known wavelength and the principles of wave interference to determine the desired error value. The signal is interpolated to produce measurement resolutions less than one nanometer. A laser beam is emitted from the laser head, which is then sent through a series of optical mirrors and reflectors. The signal is returned to the laser head where the interference signal is detected. For linear displacement measurements, the initial beam is sent through an interferometer where it is split. One beam is sent to a stationary reference retro-reflector and the other is sent to a retro-reflector on the moving object. The beams from the two reflectors return to the interferometer where they recombine, forming an interference pattern and are sent back to the laser for counting the number of fringes. Figure 2-6 shows the setup.

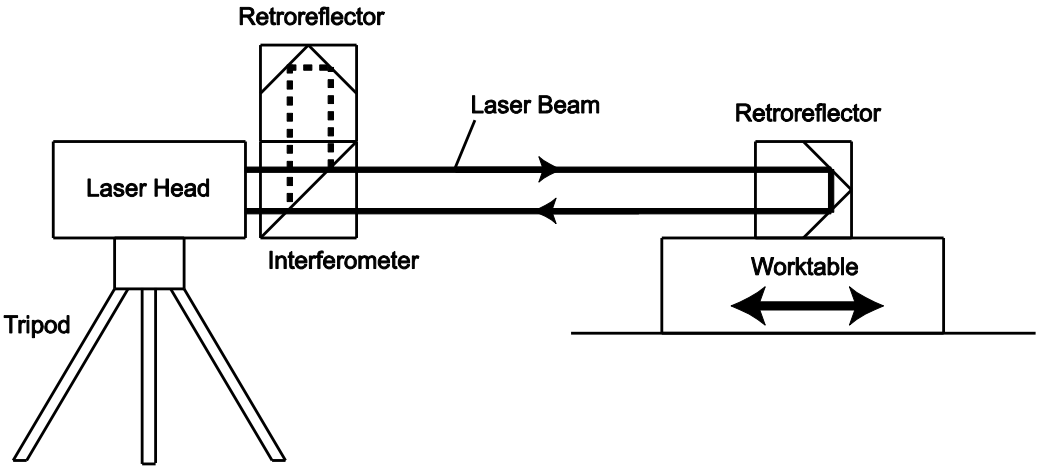

Figure 2-6. Linear positioning error setup using a laser interferometer

The medium in which the beam travels can shift the wavelength of the laser from its nominal value. The nominal wavelength is accurately measured in a vacuum to eliminate environmental effects. When measurements are performed on a machine, the environment has temperature, pressure and humidity levels which slightly decrease the wavelength. Sensors are situated within the machine and in close proximity to the laser, to measure the environment properties. Differences from the nominal wavelength measurement conditions are collected and the actual wavelength is calculated using the modified Edlén formula [26]. This process is called environmental compensation. Compensation is only required for linear displacement tests and not for straightness or angular measurements. During straightness and angular tests, the difference between the beam lengths is measured. The influence of environmental changes is negligible compared to the measured value, therefore it is not required.

The setup for straightness measurements requires optics designed specifically for this test. The optics includes a straightness interferometer (Wollaston prism) and bi-mirror straightness reflector. The beam is sent to the prism where it is split at an acute angle and both beams are sent to the reflector. The reflector returns the beams to the prism where they are re-joined and sent back to the laser head. The prism is located on the moving object while the reflector is stationary. Deviations of the prism from the straight line path will alter the lengths of the two beams sent to the reflector. One beam will increase in length while the other decreases. The change in lengths will result in a changing interference pattern registered at the laser head. From this, the amount of straightness error can be calculated. Two tests must be completed with the optics turned 90^{o} between each test to collect all of the straightness error. Figure 2-7 illustrates the straightness setup for one orientation.

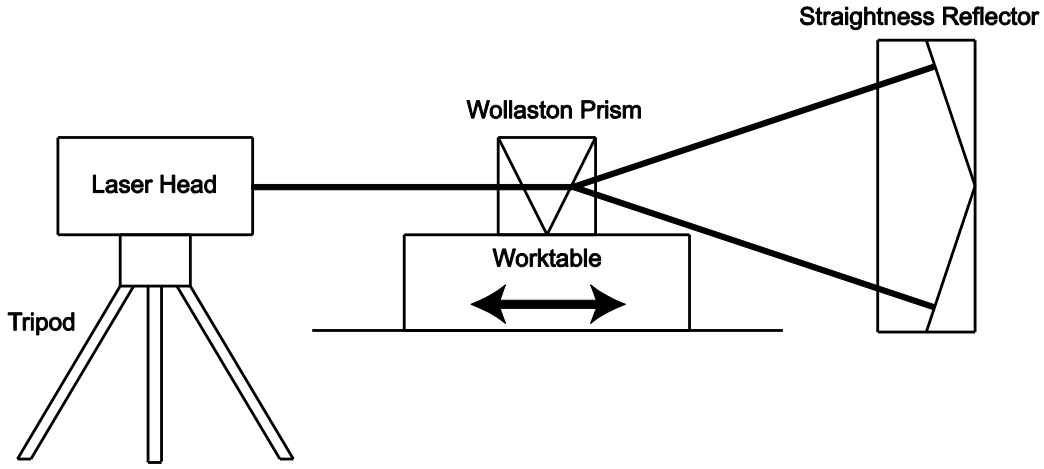

Figure 2-7. Straightness error setup using a laser interferometer

Laser interferometry cannot measure all angular errors. Roll cannot be measured, as its axis of rotation is parallel to the direction of travel and the laser path is insensitive to this motion. Roll is typically measured using a precision angular level and compared to a reference level. The setup for yaw and pitch includes an angular interferometer and angular reflector. The beam is emitted from the laser head to the interferometer, where it is split. One beam passes straight through while the other is reflected orthogonal to the original beam. The second beam is sent to an angle mirror, which directs the beam to be parallel with the first beam. Both beams are now parallel to the direction of travel. They are sent to the reflector, which consists of two retro-reflectors. The beams are sent back to the laser head along the same path. Rotation of the reflector will alter the lengths of the two beams. The change in lengths will result in a different interference pattern read at the laser head. From this, the amount of angular error can be calculated. Two tests must be completed with the optics turned 90° between each test to collect all of the angular error data. Figure 2-8 illustrates the angular setup.

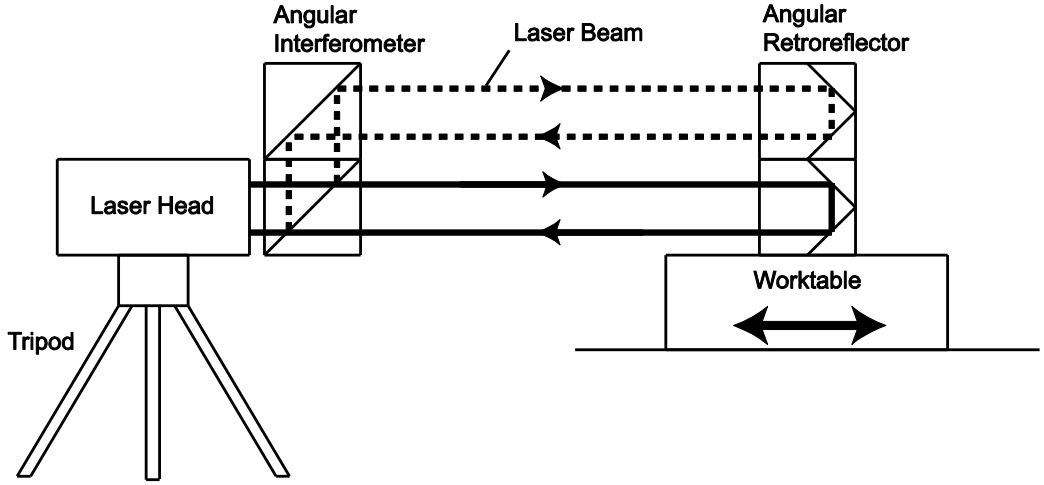

Figure 2-8. Angular error setup using a laser interferometer

Squareness of two orthogonal axes can be measured using a laser by a couple of methods. The first is using laser interferometry with specialized optics, however, the optics are expensive and were not available to the author. A second method is to use the linear positioning setup and measure the displacement along the two diagonals of the workspace. Figure 2-9 demonstrates the measurement paths and the geometry characteristics for a setup with actual squareness.

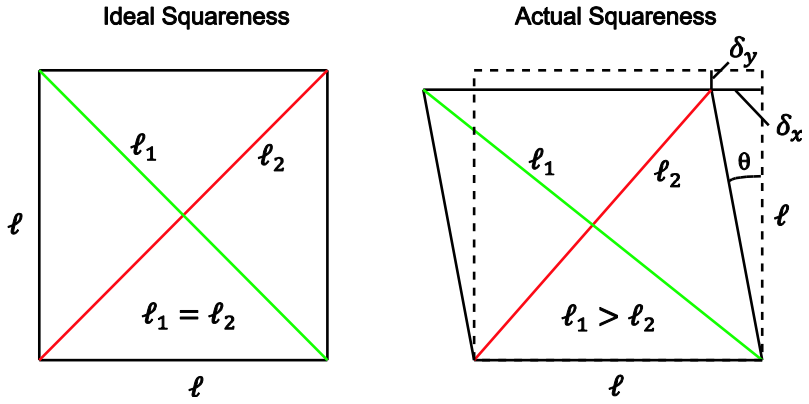

Figure 2-9. Diagonal test for squareness of a planar stage

The squareness error is the value of θ, which can be calculated by measuring the diagonals ℓ_1 and ℓ_2. The two lengths can be calculated analytically with Equations (1.1) and (1.2).

$$\ell_1^2 = (\ell + \delta_x)^2 + (\ell - \delta_y)^2 \tag{1.1}$$
$$\ell_2^2 = (\ell - \delta_x)^2 + (\ell - \delta_y)^2 \tag{1.2}$$

Subtracting Equation (1.2) from (1.1) and solving for δ_x results in Equation (1.3).

$$\delta_x = \frac{\ell_1^2 - \ell_2^2}{4\ell} \tag{1.3}$$

Expanding the numerator in Equation (1.3) and simplifying gives,

$$\delta_x = \underbrace{\frac{(\ell_1 + \ell_2)}{2}}_{\sqrt{2}\ell} \frac{(\ell_1 - \ell_2)}{2\ell}$$
$$\delta_x = \frac{(\ell_1 - \ell_2)}{\sqrt{2}} \tag{1.4}$$

The squareness error is calculated using the arcsine of δ_x/ℓ, shown in Equation (1.5).

$$\theta = sin^{-1}\left(\frac{\delta_x}{\ell}\right) \tag{1.5}$$

Substituting for δ_x, Equation (1.5) becomes,

$$\theta = sin^{-1}\left(\frac{(\ell_1 - \ell_2)}{\sqrt{2}\ell}\right) \tag{1.6}$$

This method is further explained in the international standard ISO-230-6:2002 [27] as an acceptable means of measuring squareness of machine tool axes.

2.4 Conclusions

This chapter has presented a survey of academic literature and industrial practice relevant to precision machine tool design and metrology. The design of a precision machine uses precision engineering principles to reduce the effect of errors on the positional accuracy of the machine. Geometric, thermal and friction errors are designated as the largest contributors to the error on a machine tool. Most geometric errors are repeatable in nature and can be predicted. Compensation of these errors is common practice to improving the accuracy of a machine. Thermal errors remain as one of the largest and most difficult sources to eradicate. Temperature fluctuations of the environment and concentrated heat sources expand and contract the machine's components, causing positional deviations. Temperature controlled laboratories and cooling circuits help reduce warping of the machine and lead to better accuracy. Errors due to friction tend to be non-linear in nature and can be difficult to predict and compensate. Hydrostatic and aerostatic bearings and non-contact motors are emerging as popular solutions to reduce and even eliminate friction errors, leading to better positional accuracy.

Metrology covers the analysis of a machine tool's accuracy, since it produces profiles of each type of error, which can be measured accurately and applied in geometric error compensation. Laser interferometry uses the wavelength of the beam and interpolation of wave interference to produce resolutions of less than one nanometer. The subsequent Chapters utilize many of the design and measurement techniques that were covered in this literature survey.

Chapter 3

Mechanical Design of the Precision Stage

3.1 Introduction

In this chapter, a novel design of an ultra-precision planar stage is presented. In Section 3.2, the initial concept and prototype design is developed which highlights key areas and sizing of components. The design is separated into two individual axes and is discussed in Section 3.3, which focuses on the design of the Y-axis (gantry) and the X-axis (work table). Dynamic and static analyses are presented in Sections 3.4 and 3.5 respectively. A thermal analysis of the machine is completed; the effects of temperature fluctuations and gradients are discussed in Section 3.6. Finally, an error budget of the stage is developed in Section 3.7, which outlines the major sources of error and possible methods to reduce the error of the machine. The conclusions for the design are outlined in Section 3.8.

3.2 Proposed Conceptual Design and Specifications

The ultra-precision planar stage was designed with the intention of bridging the gap between traditional machine tools, which have a large work area (1 – 2 m) and moderate level accuracy (1 – 10 μm), and nanometer (1 – 10 nm) accuracy machines with small work areas (< 20x20 mm^2). Designing a machine with a large work area and nanometer level accuracy opens up new opportunities in the micro machining industry, to fabricate macro components with micro features using one machine and one setup. The stage presented in this chapter has a work area of 300 mm x 300 mm with nanometer position feedback and is capable of motion transients with high speed (1 m/s) and high acceleration (1 g). Figure 3-1 details the conceptual design of the machine.

The stage incorporates a T-type gantry and worktable configuration which is adapted from CMM designs. The gantry provides motion in the y-axis while the worktable realizes motion in the x-axis with respect to the gantry. The gantry is supported by porous carbon air bearings on a precision ground granite base. Four round air bearings support the weight of the gantry while four preloaded rectangular bearings provide alignment to the granite guideway. The worktable is supported by a 12” x 12” (305 mm x 305 mm) Vacuum Pre-Loaded (VPL) air bearing, which utilizes both positive and negative pressure to preload the table to the granite surface. The VPL increases the vertical and pitch stiffness and transfers the load of the table and workpiece into the granite rather than the gantry beam.

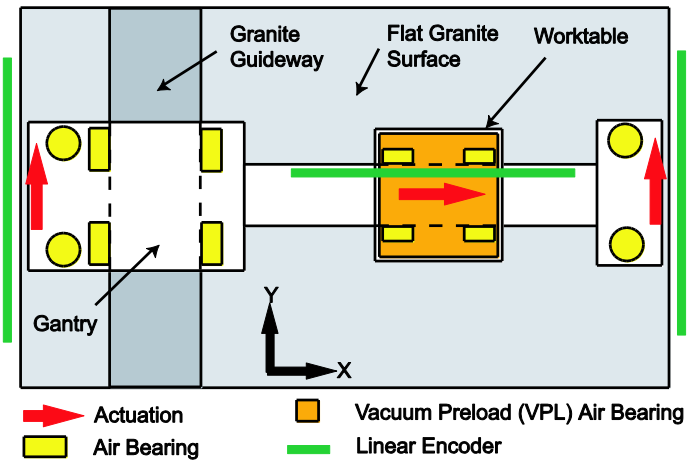

Figure 3-1. Conceptual design of stage (Top View).

Four additional rectangular bearings provide support and alignment of the worktable along the gantry beam. Actuation of the gantry is achieved by two direct drive linear motors. The primary motor is located on the side closest to the granite guideway, while the secondary motor is located on the opposite end to increase the stiffness of the beam and decrease undesired vibrations at the free end. Actuation of the worktable is realized by one direct drive linear motor located on the top of the gantry beam. High resolution position feedback (4 µm grating x4096 interpolation) is realized by glass scale linear encoders located next to their associated motors.

Design objectives of the machine include a target stiffness of 50 N/µm, positioning repeatability of < 1 µm and dynamic accuracy of 1-5 µm. This can be achieved by proper mechanical design of the stage structure, robust controller design, and compensation of known errors. Errors due to thermal deformation become more prevalent as the accuracy of a machine improves below one micron. This is due to thermal expansion of materials, which is on the order of 0 – 30 ppm/°C. The effect of thermal deformation of machine tools has been widely studied and has been noted as one of the most difficult sources of error to combat [1]. Some methods to minimize thermal error are temperature controlled environments, moving the machine slowly to prevent mechanical heat generated from friction, liquid cooling critical areas of the machine, and using materials with low coefficients of thermal expansion. Also, symmetrical designs and using materials with high thermal conductivity (like aluminum) help alleviate thermal problems to a certain extent.

A second source of error is friction which is non-linear and difficult to model or predict. CNC machine tools already incorporate friction compensation features, however they are typically simple in nature (only considering constant bidirectional Coulomb friction) and do not properly model the complexity of the actual friction. To model the friction profiles of guideways and drive systems, such as ball-screws or roller bearings, is difficult and not conducive to time constraints. Air bearings

provide an alternative solution to mechanical guideways. Air bearings produce a pressurized film of air between a flat reference surface and itself. The gap is called the fly height, which is suggested by the manufacturer to be approximately 5 µm. The bearings operate on the squeeze film damping effect, which results in higher dynamic stiffness as well as negligibly small friction coefficients (µ = 0.00001 [28]). The use of air bearings eliminates the need to model friction and compensate its error contribution.

A mechanical drive system can also constitute sources of error through backlash and lead error, such as in ball screw drives and gears. To compliment the frictionless bearings, direct drive linear motors were selected to provide actuation to the stage. They are non-contact and are capable of high acceleration and high speed.

The proposed stage design is presented in the Figure 3-2 which incorporates the above mentioned features.

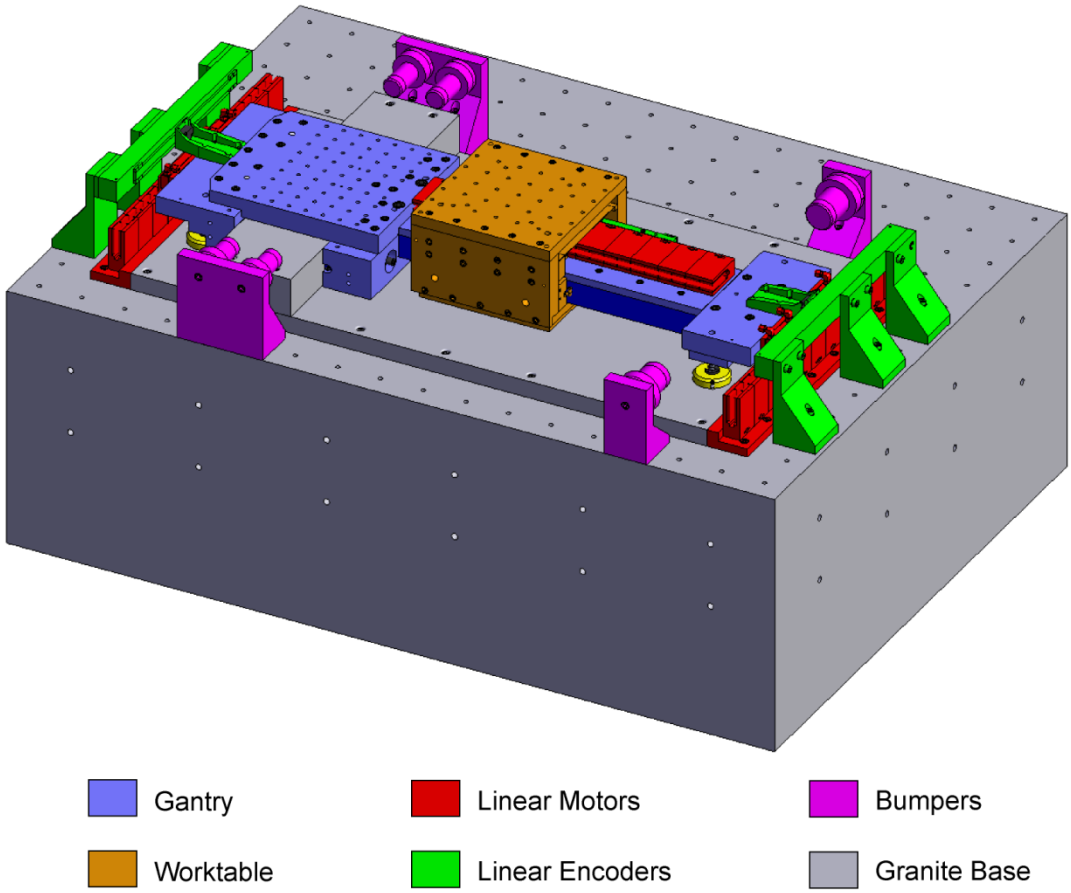

Figure 3-2. Conceptual design of precision stage.

3.3 Detailed Y-Axis (Gantry) and X-Axis (Table) Design

During the design of the gantry, special attention was focused on the four preloaded air bearings, since their location provides the majority of the yaw and x-axis stiffness for the stage. To maximize yaw stiffness, the bearings are positioned with the greatest distance apart while maintaining a travel range of 300 mm for the y-axis. The bearing size is 150 mm x 75 mm and was selected for its high stiffness (324 N/µm) and size. The structure supporting the bearings needs to be stiff in order to decrease gantry splay and deformation as the bearings are preloaded. Each bearing is preloaded with approximately 2500 N to achieve the recommended fly height of 5 µm. The structure around the bearings was designed with three components. The first reason was to minimize the number of bolted joints which reduce stiffness, and secondly to simplify the fabrication of the structure. Ideally the structure would be made of one piece, however, features such as the pockets which house the bearings would be very difficult to machine.

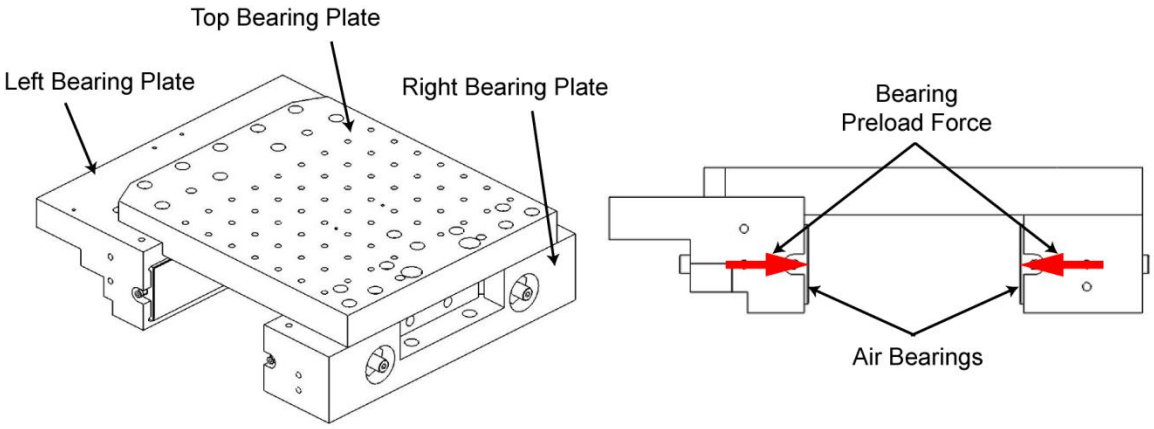

Figure 3-3. Three piece bearing support structure.

The bearings are mounted using ball mounting screws, which allow for self alignment of the bearings to their guideway. However, the stiffness of the bearing can decrease as the spherical joint is allowed to rotate. Therefore, micro-shrink cement [29] should be applied between the bearing and the surrounding structure which eliminates rotational movement and increases stiffness. The structure is designed with a 1 mm gap between the bearing and the structure, which is shown in the cross section view of Figure 3-4.

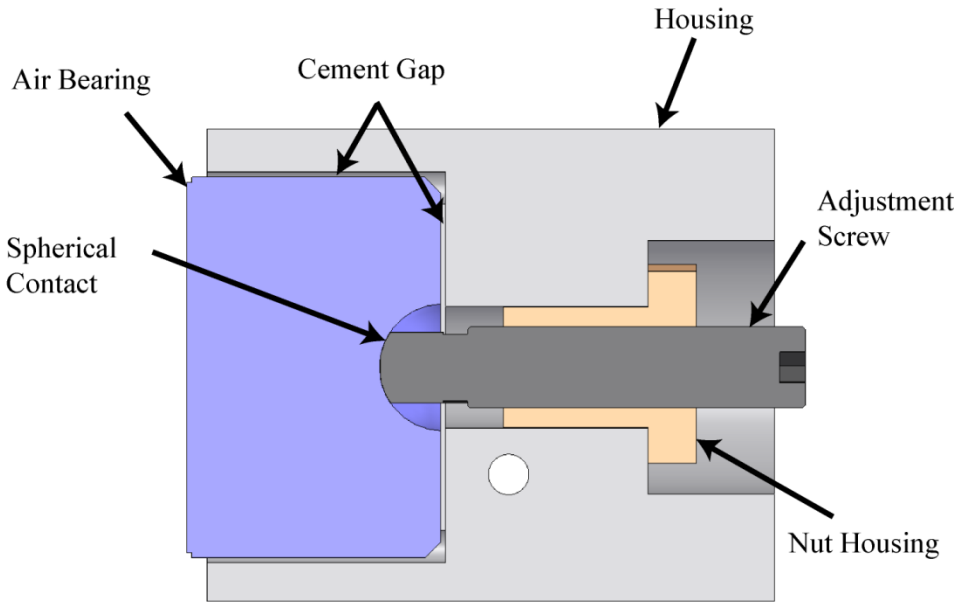

Figure 3-4. Air bearing support and adjustment design, as well as the bearing housing with 1mm gap for injection of cement after adjustment of fly heights.

The cement is installed by injection from the backside of the bearings. Cortesi from the Massachusetts Institute of Technology (MIT) also performed the same process with their Axtrusion single-axis drive [21]. They noted that two injection points spaced out along the back surface of the bearing provides better coverage than one located in the center. Therefore, two injection points were incorporated into the design of the housing. To simplify the injection process, channels were routed to the exterior of the gantry to provide ample room for syringes to inject the cement. Figure 3-6 illustrates the design of the channels in the structure and their location with reference to the bearings.

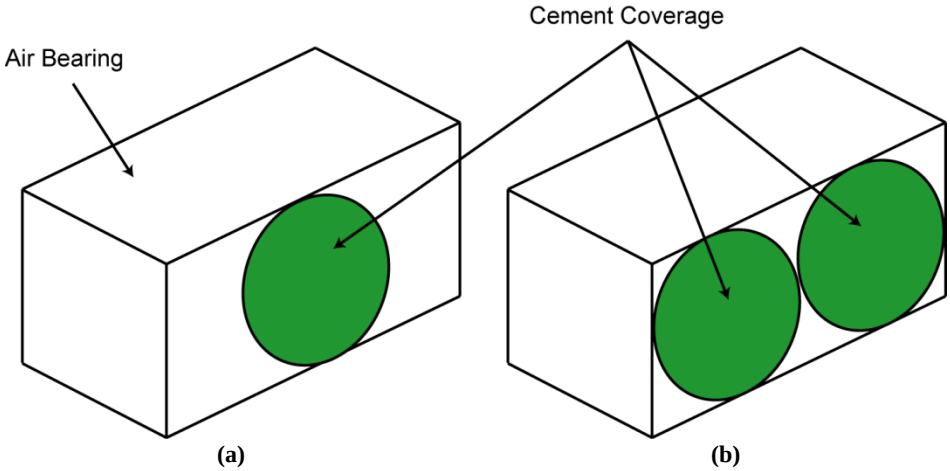

Figure 3-5. Cement coverage for (a) single injection point located at the center and (b) two injection points.

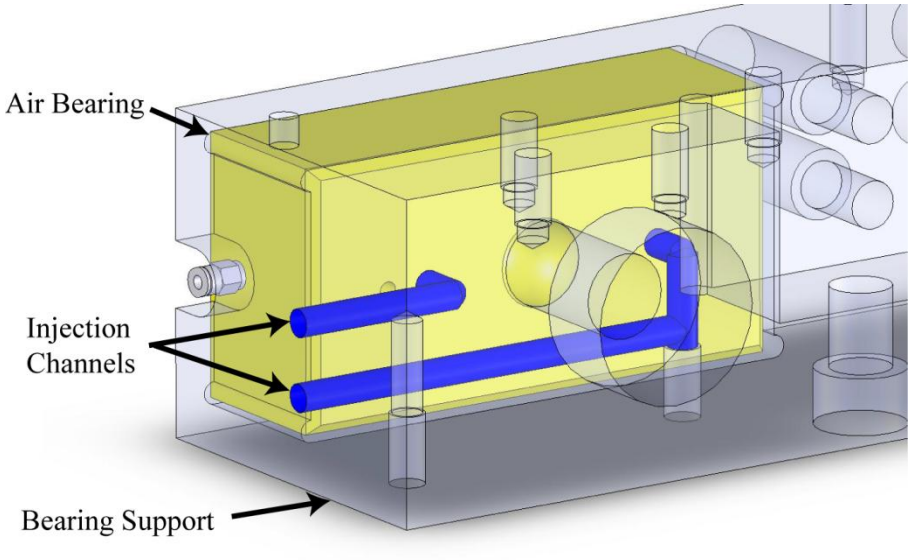

Figure 3-6. Injection channels for application of micro-shrink cement

The worktable was designed to use the gantry beam as a guideway. The beam is made with 304 stainless steel for its higher stiffness over aluminum, and non-magnetic properties. The sides of the beam are ground to 2 µm/300 mm flatness and parallelism. An aluminum plate is mounted on top of the beam, which fastens the magnetic way and the encoder scale for the x-axis. The plate allows for future additions or changes to the gantry while not modifying the steel beam itself. Since the sides are precision ground, damage to the surfaces from further machining operations will be likely and is not tolerable. The connection between the beam and the bearing structure is crucial, as it is a potential area of weakness. Since bolts create a less stiff design than single piece construction, the design incorporates a shrink fit between the bearing structure and the beam. A pocket is machined into the aluminum which is undersized by 0.001" (25.4 µm). The aluminum is placed in an oven at 125°C to expand the pocket and allow easy installation of the beam. While it is cooling, the aluminum contracts onto the beam for a highly stiff connection.

The linear motors are secured via internally cooled couplings. The couplings have internal channels as shown in Figure 3-7, which cycle temperature controlled glycol at 20°C and aid in removing the heat generated by the linear motors. The coupling design and installation can be seen in Figure 3-7.

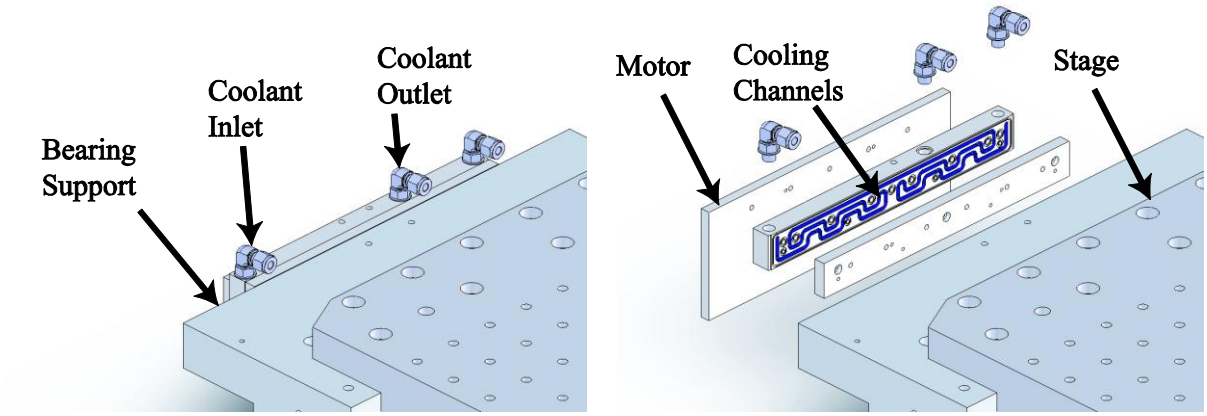

Figure 3-7. Y-axis cooling coupling shown in (a) collapsed view, (b) exploded view highlighting internal cooling channels.

The motors can reach a maximum temperature of 130°C with a maximum heat dissipation of 131 W [31]. If the energy from the motors were allowed to transfer into the gantry, the expansion and warping of the aluminum would result in severe positioning errors. By removing the heat as close to the source as possible, the gantry maintains a constant temperature and preserves its positional accuracy. It is also important to remove the heat in order to maintain the stiffness of the preloaded bearing arrangements. By analyzing the expansion of the Top Bearing Plate shown in Figure 3-3, a simple calculation illustrates the effects of temperature change on the stiffness of the machine. The desired fly height of the air bearings is 5um. Therefore, the overall air gap between two preloaded bearings is 10 µm. The coefficient of thermal expansion for aluminum is 24 ppm/°C and the granite guideway is 200 mm wide. Therefore, if the temperature of the top plate increases by 1°C, the fly height for each bearing will increase from 5 µm to 7.4 µm. And if the temperature increases by 2°C, then the gap nearly doubles to 9.8 µm. The bearing stiffness is non-linear as shown in Figure 3-8, therefore the increase of the fly height will reduce the stiffness of the bearings and the overall structure. Therefore, it is crucial to restrict any heat from reaching the stage. A further analysis of the couplings is presented in Section 3.6 to verify the efficiency of the couplings.

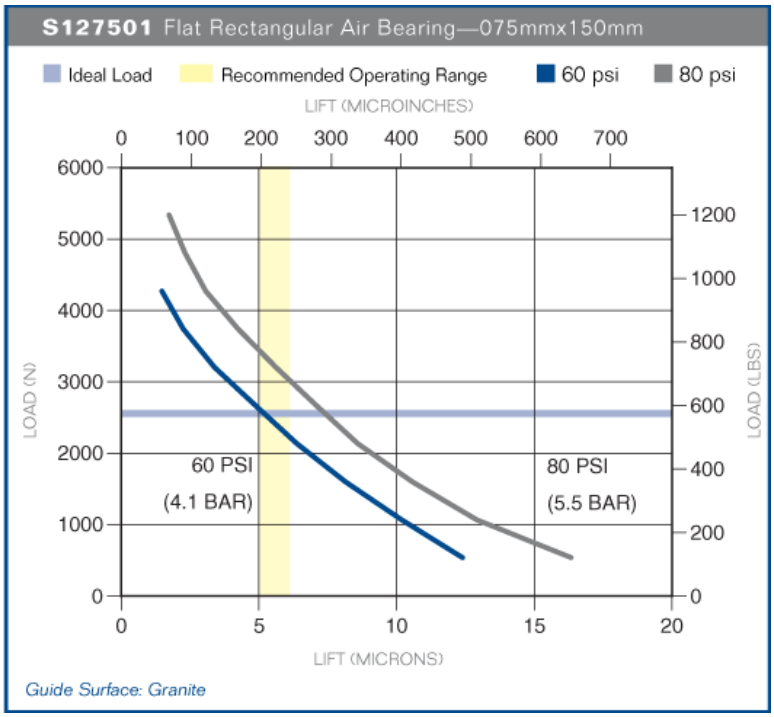

Figure 3-8. Air bearing lift-load curve showing non-linear stiffness [30]

The high resolution optical encoders are located as close to the motors as possible to reduce measurement error. The scales are made of glass with a 4 µm grating. The encoder signal is two sinusoidal waves with a 90° phase shift and amplitude of 1Vpp. The signals are interpolated 4096 times to produce a resolution of 0.97 nm. However, there will be signal-to-noise ratio issues which will produce a more realistic resolution of ~10 nm. An absolute reference signal is located every 10mm. The encoder heads are mounted to a bracket which positions the head 0.5 mm from the surface of the scale. A rigid stainless steel bracket was designed to maintain high stiffness and reduce vibration of the encoder head.

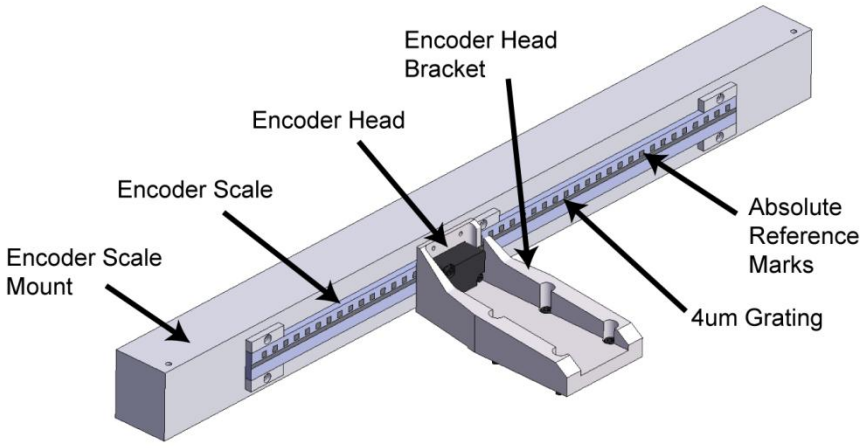

Figure 3-9. Encoder head and mounting bracket design for high stiffness

A similar preloaded bearing arrangement, as seen with the gantry, is implemented for the table. Four air bearings are preloaded against the gantry beam and with a separation distance of 215 mm. The table is actuated by one direct drive linear motor with one linear encoder providing high resolution feedback. It has a travel length of 300 mm and is capable of achieving 1 g acceleration and 1 m/s velocity. The location of the linear motor is situated such that the point of actuation is directly above the center of mass, which reduces moment loads on the table during actuation. Figure 3-10 shows many components of the worktable while illustrating the relative location and alignment of the motor and encoder.

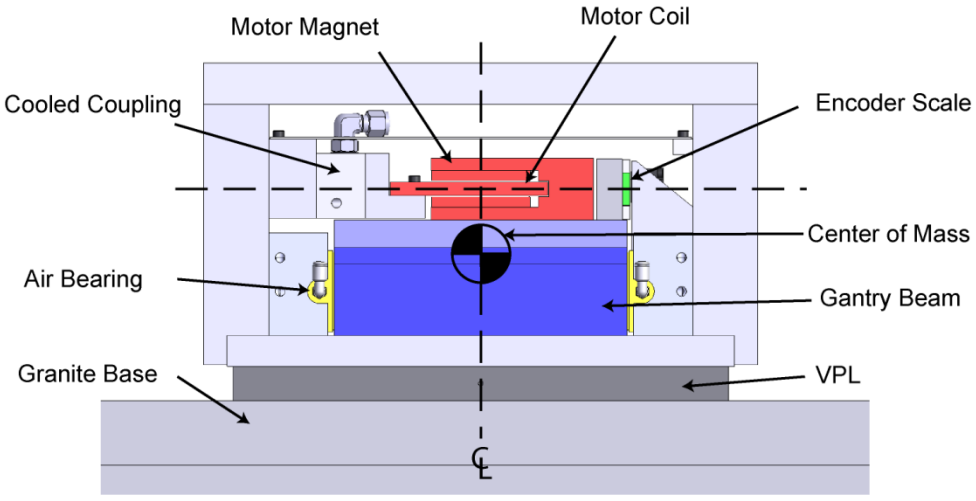

Figure 3-10. Table design arrangement for minimal moment loads and measurement errors.

The centerline of the motor was aligned with the center of the encoder scale to reduce measurement error during actuation.

What sets the worktable apart from other machine designs is the VPL air bearing located on the underside of the table. All vertical loads are transferred through the VPL and onto the granite base. The gantry beam is decoupled from these loads. This reduces bending loads of the beam and increases the vertical stiffness of the worktable. Pitch stiffness is also improved by the VPL, which aids in mitigating angular errors during the acceleration movement. The VPL works by applying both positive and negative pressure to different regions on its bottom surface as detailed in Figure 3-11. An ambient pressure groove is located between the vacuum and pressurized regions to avoid cross contamination.

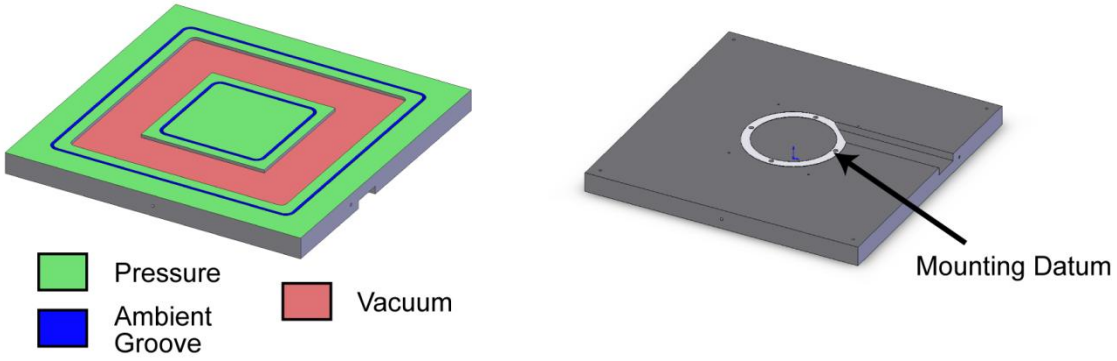

Figure 3-11. (a) Underside of VPL showing different pressure regions, (b) Top view of mounting datum ring.

Cement will be applied to the four x-axis air bearings as well as the VPL to improve the stiffness of the worktable. The process explained for the four air bearings of the gantry is replicated for the four air bearings of the worktable. However, a different approach was taken for the VPL.

To explain the application of the cement to the VPL, an explanation of the geometry is required. The VPL's datum surface is a 100 mm diameter ring located at its center. This datum is 0.010" (0.254 mm) above the remaining top surface. The required thickness of cement is 0.030" (0.762 mm) therefore a 0.020" (0.508 mm) deep pocket must be built into the plate which mounts to the VPL. To ensure the cement is properly applied through the entire surface of the VPL, a series of nine injection points span the surface. Starting with one injection point, the cement is injected until it can be seen at the next injection hole. The first hole is sealed by a screw and the syringe is moved to the next hole. This process is repeated until all holes are sealed. With this process, the cement fills the majority of the pocket, providing the maximum stiffness from the cement. To avoid leaks around the outer edge of the plate, an o-ring cord is used along the perimeter, which seals the gap between the plate and the VPL.

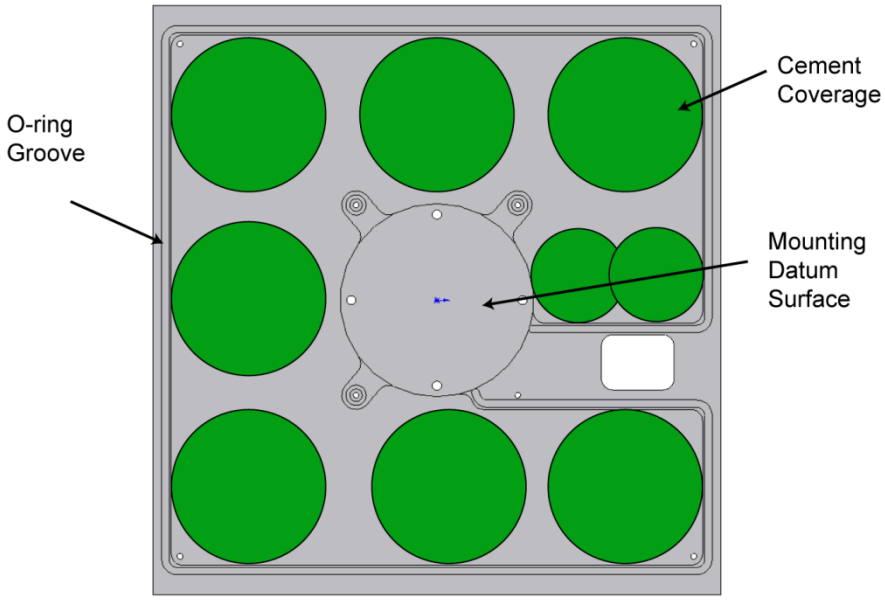

Figure 3-12. VPL mounting plate showing minimum cement coverage, datum surface and O-ring groove.

The top plate of the worktable is made of 7075 Aluminum, which is more resistant to damage than 6061 Aluminum. This is ideal as vices and other equipment will be installed and removed often and the integrity of the table must remain intact. An example of such equipment is a trunnion which is comprised of two rotary axes and will be mounted to the worktable for a future 5-axis design. The mounting pattern for the trunnion is incorporated into the top plate hole pattern.

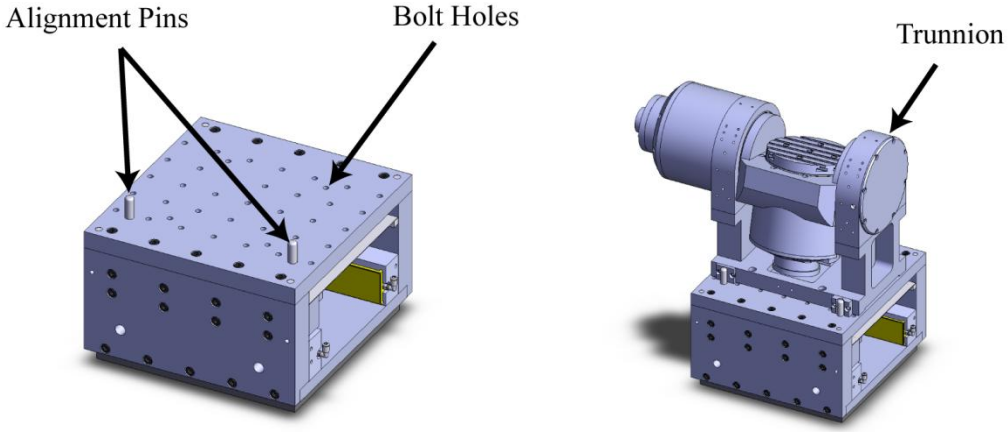

(a) **(b)**

Figure 3-13. Top plate of worktable with (a) bolt pattern and alignment pins, (b) with trunnion installed.

An internally cooled coupling was also designed for the x-axis motor. The design is similar to the y-axis couplings, but was altered for the different geometry of the worktable. The design will be

explained in Section 3.6. The fully assembled stage comprised of the granite base, gantry and worktable can be seen in Figure 3-14.

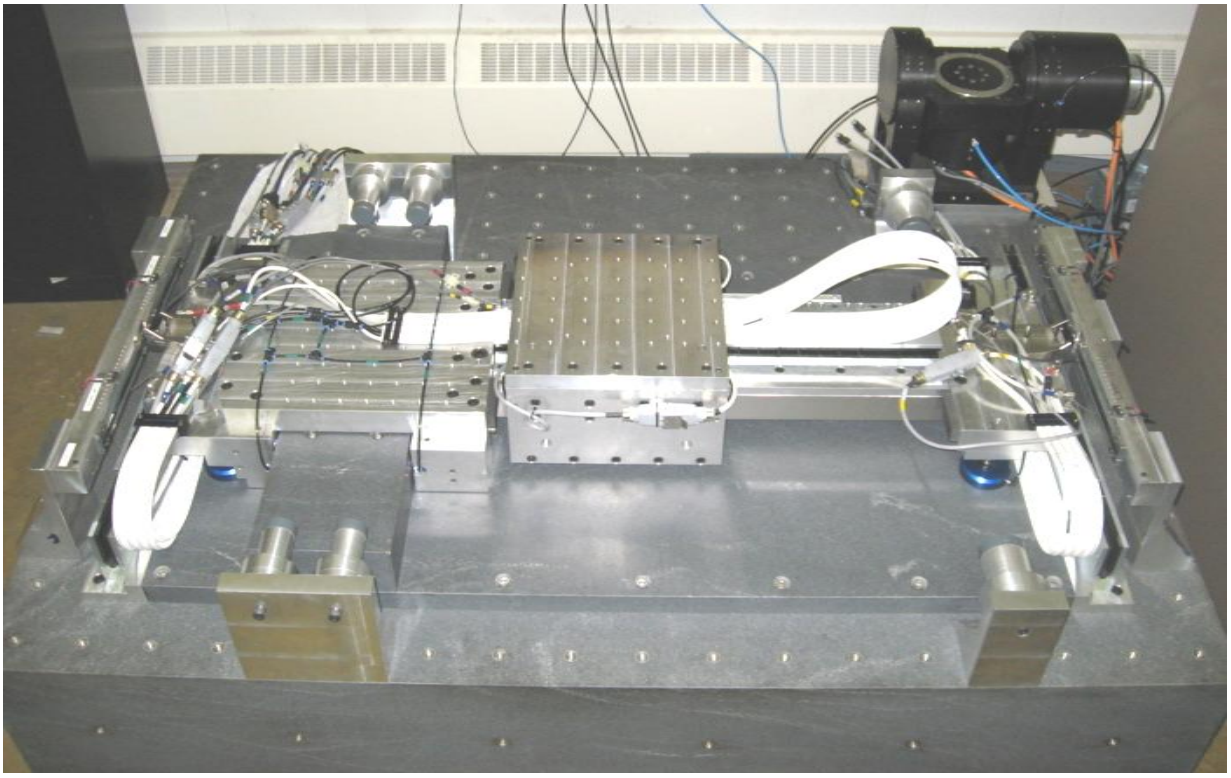

Figure 3-14. Assembled prototype of precision XY stage.

3.4 Dynamic Analysis

The linear motors were selected to accelerate the stage at 1g with a maximum velocity of 1m/s. The motor specifications from the manufacturer list the peak and continuous force to be 1247 N and 277 N respectively [13]. The total moving mass in the y direction is approximately 180 kg. Therefore the maximum acceleration from two motors is 14.3 m/s^2 or 1.45 g. To reach maximum velocity, there needs to be adequate travel to go from rest to maximum speed and back to rest. The trajectory generator provided with the controller software implements a piecewise constant jerk profile. Using this profile and applying our maximum acceleration, velocity and travel requirements, the following profile is produced.

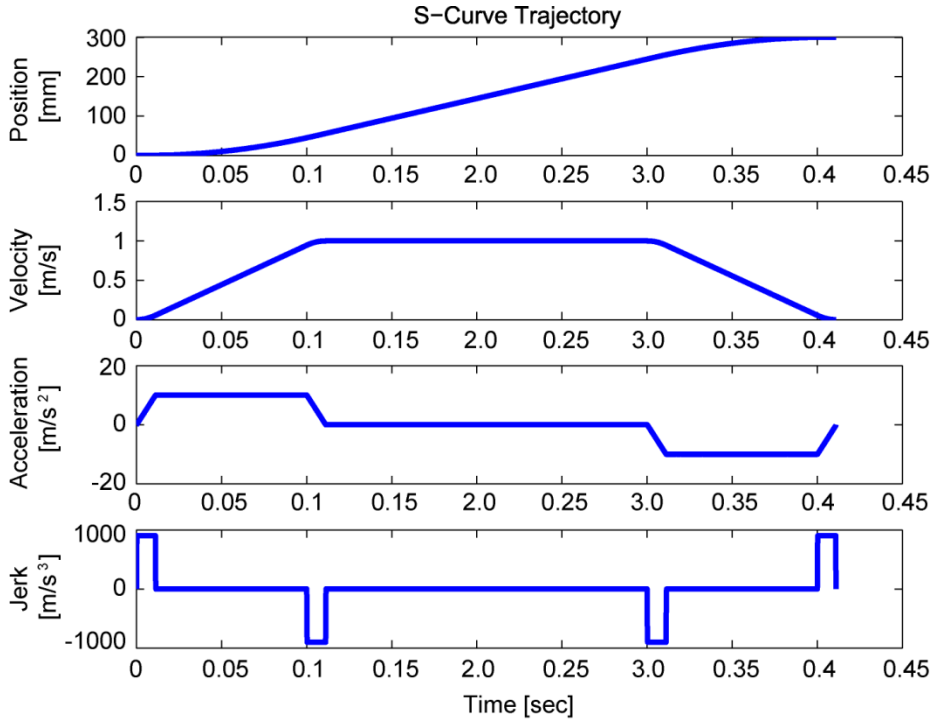

Figure 3-15. Example of trajectory profile

It can be seen from the figure that maximum velocity is reached for 200 mm of travel within the entire 300 mm range of travel. The following table lists some key values related to the machine and its dynamic performance.

Table 3-1. List of dynamic values of the machine.

	X	**Y**
Mass [kg]	33	180
Max Motor Force [N]	1247	2494
Maximum Acceleration [g]	3.85	1.45
Maximum Velocity [m/s]	1.0	1.0
Maximum Stroke [m]	0.3	0.3
Feedback Resolution [nm]	0.97	0.97

Machine vibration is an area which cannot be ignored and must be studied in parallel with rigid body dynamics. Vibrations can lead to loss of positional accuracy, weakening of the machine's structure as well as controller instability. An assessment of different sources of vibration was performed to attempt to identify the dynamics of the stage. Understanding the source of vibration can aid in determining solutions to diminish its effects on the accuracy of the machine.

The gantry beam was identified as a likely source of vibration with detrimental effects to accuracy as well as stability of the machine. Two areas were analyzed, which are the rigid body yaw vibration and the first bending mode of the beam. The frequency of the yaw vibration will be referred to as the yaw frequency. The natural yaw frequency is calculated with Equation (3.1).

$$\omega_n = \frac{1}{2\pi}\sqrt{\frac{k_\theta}{I}} \tag{3.1}$$

Where,

k_θ is the yaw stiffness $\left(\frac{N\cdot m}{rad}\right)$
I is the Moment of Inertia $(kg \cdot m^2)$

The yaw stiffness of the gantry can be calculated by relating the stiffness of the bearings to an equivalent angular stiffness. Equation (3.2) is the definition of linear stiffness while Equation (3.3) is angular stiffness.

$$k = \frac{F}{\delta} \tag{3.2}$$

$$k_\theta = \frac{M}{\theta} \tag{3.3}$$

Assuming small angles, the following diagram is used to relate Equations (3.2) and (3.3). The forces applied by the linear springs can be converted to an equivalent moment and the linear deflection can be related to an angular deflection as noted in Equation (3.4). The air bearings apply unidirectional stiffness which only acts during compression of the air gap. Therefore, during angular vibration of the gantry, it is assumed that only two bearings provide stiffness during yaw.

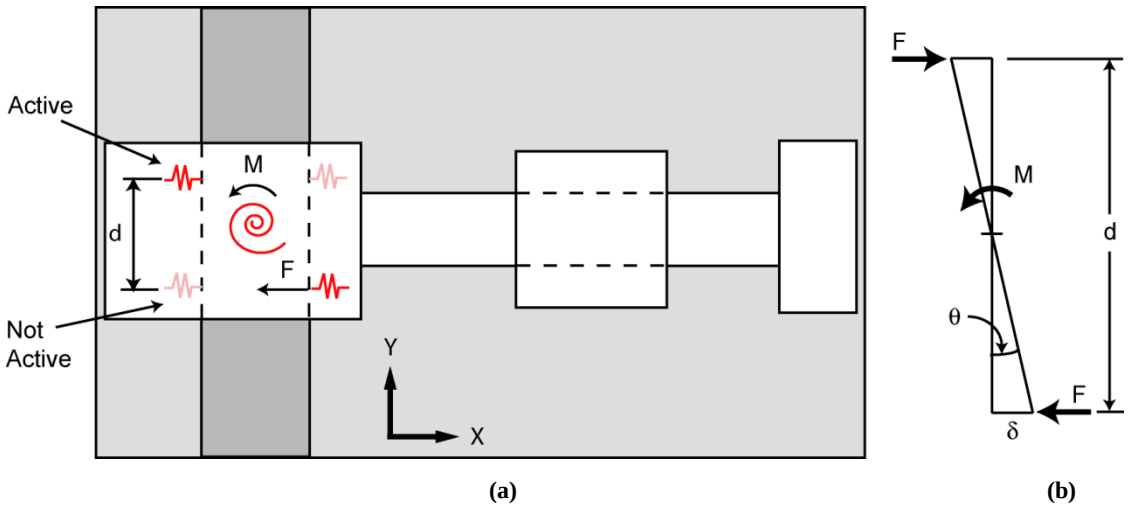

Figure 3-16. Relationship between the 4 preloaded air bearings and a torsional spring. (a) overall machine diagram and (b) geometrical relationship

$$k_\theta = \frac{M}{\theta} = \frac{2F\left(\frac{d}{2}\right)}{\frac{\delta}{\left(\frac{d}{2}\right)}} \tag{3.4}$$

Simplifying Equation (3.4) to include the stiffness of the linear bearings yields,

$$k_\theta = 2k_b\left(\frac{d}{2}\right)^2 \tag{3.5}$$

The moment of inertia in Equation (3.1) is calculated about the torsional spring in Figure 3-16. Due to the complexity of the stage, the inertia is approximated using CAD software. The moment of inertia of the worktable is determined using CAD and the parallel axis theorem to translate the inertia to the same location as the gantry. The following table lists the required values to solve Equation (3.6).

Table 3-2. List of required values to calculate the natural frequency of the yaw vibration of the gantry.

Description	Symbol	Value	Units
Bearing Stiffness [30]	k_b	324	N/um
Distance between bearings	d	0.25	m
Moment of Inertia of Gantry about bearings	I_g	46.63	kgm^2
Moment of Inertia of Table about its center	I_t	0.6058	kgm^2
Distance from table to gantry moment of inertia	d_t	0.4 – 0.7	m
Mass of worktable	m_t	33	kg

$$\omega_n = \frac{1}{2\pi}\sqrt{\frac{2k_b\left(\frac{d}{2}\right)^2}{I_g + (I_t + m_t d_t^2)}} \tag{3.6}$$
$$\boldsymbol{\omega_n = 67\ Hz}, for\ d_t = 0.55$$

A natural frequency of 67 Hz has been calculated for the yaw vibration. It should be noted that this frequency was also spotted in the Frequency Response measurement acquired in Chapter 4.

The first bending mode is modeled by considering the beam as a simple fixed-free cantilever. Equation (3.7) calculates the first bending mode frequency [32].

$$\omega_n = \frac{3.52}{2\pi}\sqrt{\frac{EI}{wL^4}} \tag{3.7}$$

Where,

$E =$ Modulus of elasticity (Pa)
$I =$ Area moment of inertia (m^4)
$w =$ Mass per length $\left(\frac{kg}{m}\right)$
$L =$ Length of beam (m)

Table 3-3 lists the terms required for the calculation of the first bending mode of the beam.

Table 3-3. List of terms required for calculating the first bending mode of the gantry beam.

Description	Symbol	Value	Units
Modulus of elasticity	E	193	GPa
Area moment of inertia	$I = \frac{bh^3}{12}$	2.624x10^{-5}	m^4
Beam width	b	0.054	m
Beam height	h	0.18	m
Beam length	L	0.87	m
Mass per length	w	77.76	kg/m

$$\omega_n = \frac{3.52}{2\pi}\sqrt{\frac{E\left(\frac{bh^3}{12}\right)}{wL^4}} \tag{3.8}$$
$$\omega_n = 190Hz$$

This analysis is an approximation and will be further analyzed during the frequency response identification experiments in Chapter 4.

3.5 Static Stiffness Analysis

The static stiffness of the machine is derived from the stiffness of the air bearings, linear motors, and the bending stiffness of the gantry beam. An additional analysis is performed on the pitch of the gantry during constant acceleration. The air bearing stiffness, as reported by the manufacturer, for each bearing at the 5 µm nominal fly height is listed in the table below.

Table 3-4. Stiffness values of air bearings used on the machine.

Bearing Size	Symbol	Stiffness [N/µm] [30]
∅80 mm (Round)	k_1	114
75 mm x 150 mm (Rectangular)	k_2	324
50 mm x 100 mm (Rectangular)	k_3	110

The stiffness is calculated in the x and y axes using Figure 3-17.

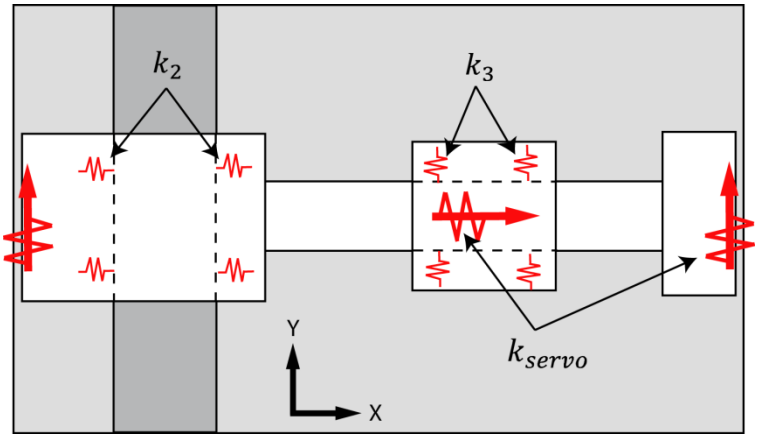

Figure 3-17. Stiffness diagram of the machine to analytically determine the overall stiffness in the x and y directions.

The total stiffness in the x-axis is calculated assuming the springs act in series. A similar calculation is made for the y-axis, however, the pitch stiffness acts in parallel.

$$k_x^{-1} = 2k_2^{-1} + k_{servo}^{-1} \tag{3.9}$$

$$k_y^{-1} = 2k_3^{-1} + 2k_{servo}^{-1} + k_{bending}^{-1} \tag{3.10}$$

The additional $k_{bending}$ term for the y-axis stiffness is related to the bending of the beam under static load. The beam can be represented by a torsion-pinned configuration as shown in Figure 3-18.

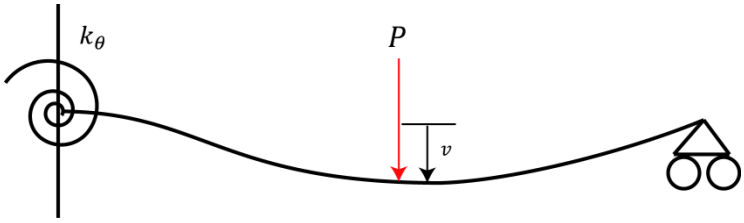

Figure 3-18. Static bending diagram of the gantry beam.

The torsion spring represents the yaw stiffness of the four preloaded air bearings, as mentioned in Section 3.4, and the pinned joined on the right assumes the secondary motor is powered, providing infinite static stiffness due to the implementation of integral action in the control law. The elastic curve formula is used to derive the equation of the deflection for the beam. Since the formula is 4th order, four boundary conditions are required to calculate the integration constants.

$$EI\frac{d^4v}{dx^4} = w(x) \tag{3.11}$$

$$\begin{aligned} v(0) &= 0 \\ v(L) &= 0 \\ v''(L) &= 0 \\ v''(0) &= \frac{k_\theta}{EI}v'(0) \end{aligned} \tag{3.12}$$

Where,

$v =$ Deflection (m)

$w =$ Force (N)

$E =$ Modulus of Elasticity (Pa)

$I =$ Moment of Inertia (m^4)

$k_\theta =$ Torsion Stiffness Constant $\left(\frac{N \cdot m}{rad}\right)$

Solving for $v(x)$ gives

$$v(x) = \frac{P}{288(EI)^2 + 96EIk_\theta L}\big(x\big(k_\theta L(9L - 11x)x + 6EI(3L^2 - 4x^2)\big) - 2(3EI + k_\theta L)(L - 2x)^3 H[-L + 2x]\big) \tag{3.13}$$

To determine the minimum stiffness, the point which has the most deflection must be determined. To find the point, the equation for slope of the beam $(v'(x))$ is set equal to zero and solved for x. It was found that the maximum deflection occurs at $0.513L$. To simplify the mathematics involved to determine the bending stiffness, it is assumed that the maximum deflection occurs at $L/2$. Therefore, the equation for the bending stiffness of the beam is:

$$k_{bending} = \frac{P}{v\left(\frac{L}{2}\right)} = \frac{768EI(3EI + k_\theta L)}{L^3(48EI + 7k_\theta L)} \tag{3.14}$$

The torsion stiffness k_θ was calculated using Equations (3.2) - (3.5).

The servo stiffness is derived from the bandwidth of the controller which can be calculated as follows:

$$k_{servo} = m\omega_{bw}^2 \tag{3.15}$$

The stiffness from each axis was analyzed under three cases with varying servo stiffness. Case 1 assumes a 30 Hz servo bandwidth, which is common on most machine tool drives. Case 2 assumes 100 Hz servo bandwidth, which is common in high performance servo-drives. Case 3 assumes infinite dc stiffness due to integral action from the controller. This assumption is realized by analyzing a simple first order system with a PID controller.

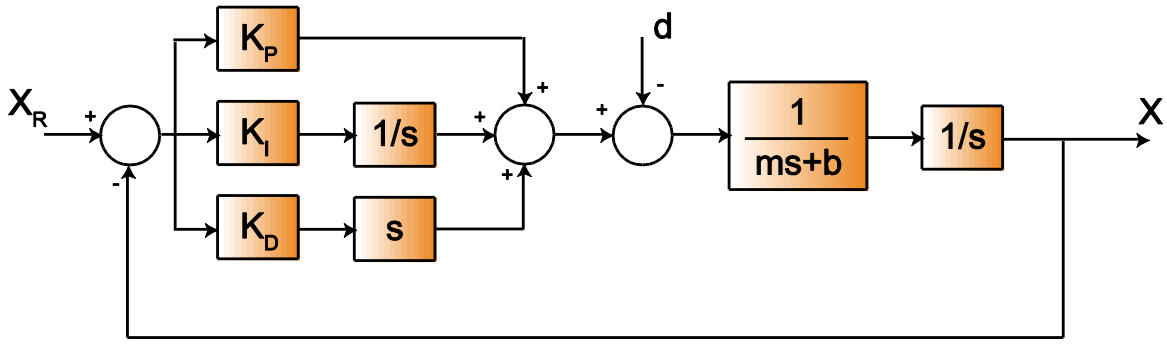

Figure 3-19. Block diagram of a first order system with a PID controller

Simplifying the block diagram and solving for the output in terms of the inputs produces,

$$X(s) = \frac{K_d s^2 + K_p s + K_i}{s^3 + \frac{(b + K_d)}{m} s^2 + \frac{Kp}{m} s + \frac{K_i}{m}} X_r(s) + \frac{\frac{1}{m} s}{s^3 + \frac{(b + K_d)}{m} s^2 + \frac{Kp}{m} s + \frac{K_i}{m}} d(s) \tag{3.16}$$

During a situation where the stage is under control and at rest, the reference input (X_r) is zero. Therefore the disturbance (d) input is the remaining factor which determines the stiffness of the controller. Plotting the disturbance transfer function in the frequency domain produces the profile in Figure 3-20. For a static load disturbance, the frequency can be assumed to be ~0 Hz and according to the figure, the magnitude at 0 Hz approaches zero. Therefore, static stiffness for a controller with integral action can be assumed to be infinite.

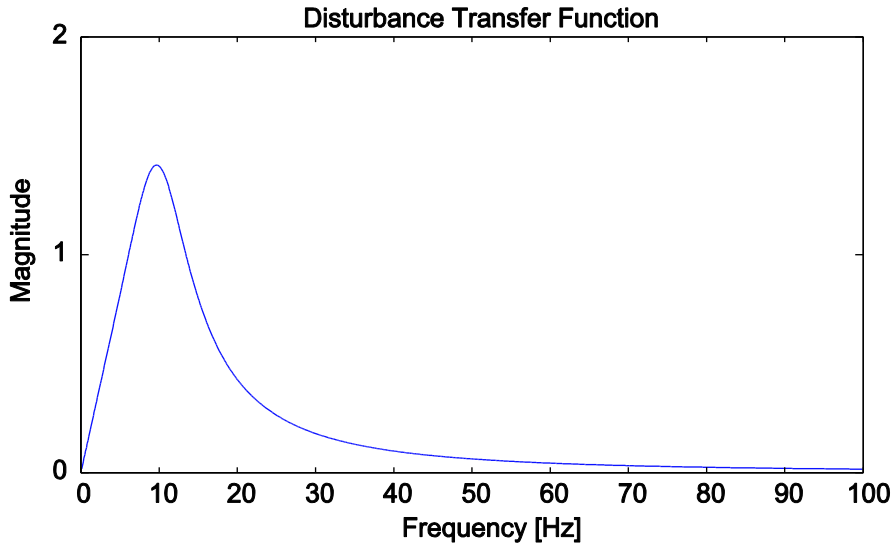

Figure 3-20. Disturbance transfer function of a PID controller for a 1st order model system.

During constant acceleration of the gantry, a moment load is applied due to the motors not acting along the center of mass, which causes the gantry to pitch. This rotation causes a linear deflection at the encoder heads, which is recorded as displacement error. The value of this displacement can be determined by analyzing a free body diagram of the gantry in Figure 3-21.

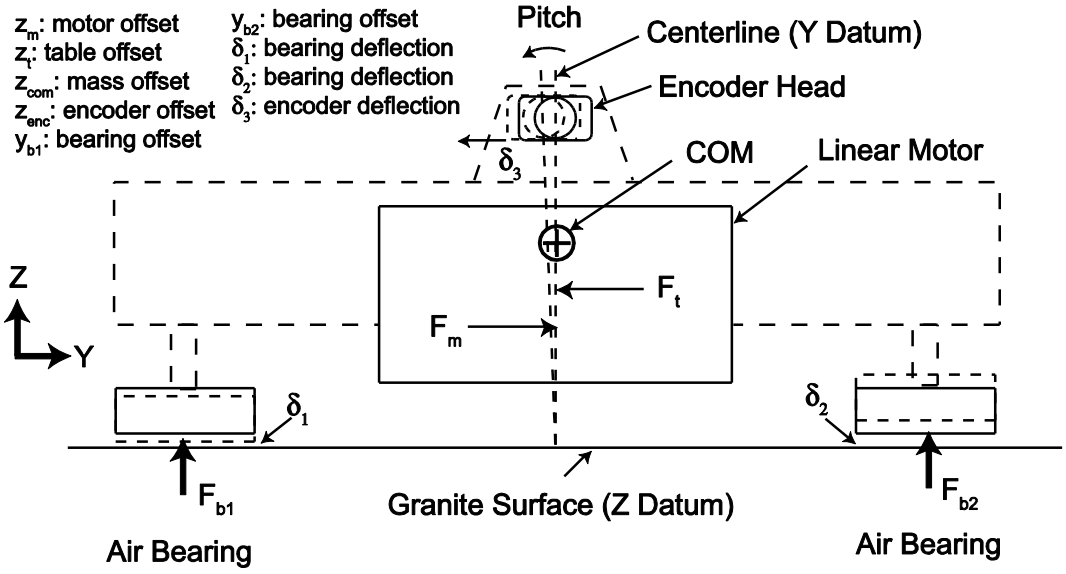

Figure 3-21. Free body diagram of gantry pitch motion during constant acceleration

The force equations were calculated using the center of mass as the reference point.

$$\sum F_z = 0 = F_{b1} + F_{b2} - m_G g \tag{3.17}$$

$$\sum F_y = m_G a = F_m - F_t \tag{3.18}$$

$$\sum T_x \cong 0 = F_m(z_{com} - z_m) - F_t(z_{com} - z_t) - F_{b1}y_{b1} + F_{b2}y_{b2} \tag{3.19}$$

Solving the system of equations for F_{b1} and F_{b2}, results in the following equation.

$$F_{b1,b2} = \frac{m_G g}{2} \pm \frac{a}{2y_{b1,b2}}[(m_G + m_t)(z_{com} - z_m) - m_t(z_{com} - z_t)] \tag{3.20}$$

Table 3-5 lists the values required to calculate the load of the bearings during 1 g acceleration.

Table 3-5. Gantry pitch parameter values

Parameter	Value	Units
g	9.81	m/s^2
a	9.81	m/s^2
m_G	142	kg
m_t	33	kg
$y_{b1,b2}$	166	mm
z_{com}	85.0	mm
z_m	50.0	mm
z_t	67.5	mm

The load of the each bearing was found to be $F_{b1} = 430$ N, and $F_{b2} = 266$ N. These values can be used to determine the fly height of the bearings by analyzing the lift-load curve, provided by the manufacturer, in Figure 3-22.

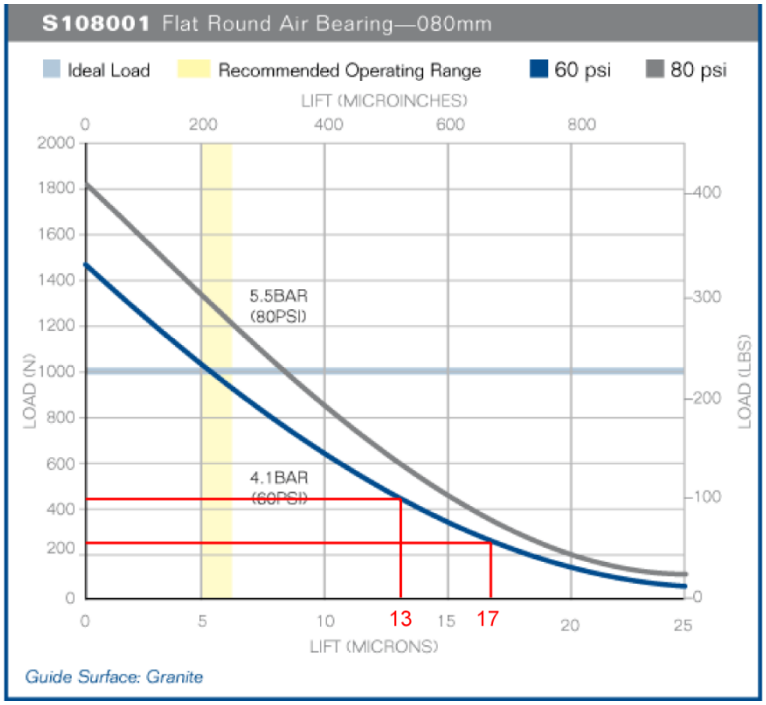

Figure 3-22. Lift-load curve for 80mm diameter air bearings [30]

It can be seen from the figure that $\delta_1 = 13$ μm and $\delta_2 = 17$ μm. The deflection of the encoder head is calculated using Equation (3.21) with $z_{enc} = 140$ mm.

$$\frac{(\delta_2 - \delta_1)}{y_{b1} + y_{b2}} = \frac{\delta_3}{z_{enc}} \qquad (3.21)$$
$$\delta_3 = 1.7\ um$$

Therefore, during 1 g acceleration, a 1.7 μm measurement error is created by the deflection of the encoder head. In later sections, an acceleration of 0.2 g is used for analysis and the encoder head will experience a measurement error of 0.34 μm. Table 3-6 presents the stiffness in each axis for all 3 cases.

Table 3-6. Overall stiffness of the x and y axes for 3 different servo bandwidths.

		Case 1		Case 2		Case 3	
		X	Y	X	Y	X	Y
SERVO STIFFNESS							
	f_{servo} [Hz]	30	30	100	100	∞	∞
	ω_{servo} [rad/sec]	188	188	628	628	∞	∞
	m_{servo} [kg]	33.0	175	33.0	175	33.0	175
	k_{servo} [N/μm]	**1.17**	**6.22**	**13.0**	**69.1**	**∞**	**∞**
BEARING STIFFNESS							
	$k_{bearing}$ [N/μm]	**648**	**220**	**648**	**220**	**648**	**220**
BENDING STIFFNESS							
	E [GPa]		193		193		193
	I [m^4]		2.62x10^{-5}		2.62x10^{-5}		2.62x10^{-5}
	k_θ [Nm/rad]		1.01x10^7		1.01x10^7		1.01x10^7
	L [m]		0.870		0.870		0.870
	$k_{bending}$ [N/μm]		**422**		**422**		**422**
TOTAL STIFFNESS							
	k [N/μm]	***1.17***	***5.97***	***12.8***	***46.8***	***648***	***145***

The total stiffness of the axes is highly influenced by the servo stiffness of the motors. Therefore, dynamic identification and controller design are crucial in order to verify the design specification of 50 N/μm. The controller design is discussed in detail in Chapter 4.

3.6 Thermal Analysis

Thermal analyses of machine tools and their environment are significant to facilitate their accuracy specifications. Traditional machine tools require a warm up period which has the machine powered and moving in order to reach thermal equilibrium. The time required can be several hours in order to reach this state [1]. As the machine warms up, the motors, guideways, bearings, etc. heat up and expand which causes positioning errors. This issue is typically avoided since the machines are

run on long shifts which can last for days at a time therefore the machine is at or near thermal equilibrium. The design of the machine can also help reduce the effect of thermal errors. A symmetric machine structure will typically expand in a symmetric and uniform fashion. If the encoder heads are positioned along the axis of symmetry, they become insensitive to thermal effects. However, an asymmetric structure expands in a more complicated manner, which can make it difficult to measure and compensate for any positional errors. For machines composed of different materials, thermal variation causes warping between the components. For example, if an aluminum and steel plate are bolted together and their temperatures are raised, stress will be created between the two components since the aluminum expands more than steel. A warping effect will be seen due to this thermally induced stress. The machine in this thesis uses aluminum, stainless steel, glass and granite. These all have different coefficients of expansion. Therefore, it is imperative to mitigate all sources of thermal error at their source, which in this case are the environment and the linear motors.

The expansion of the stage due to a change in temperature was estimated to determine the magnitude of positional errors which may be observed. The following table outlines which areas of the stage are sensitive and which do not require analysis.

Table 3-7. Areas of the stage which are sensitive to thermal changes.

	X	**Y**
Gantry Structure	***sensitive***	insensitive
Worktable Structure	insensitive	insensitive
Gantry encoder scales	insensitive	***sensitive***
Worktable encoder scale	***sensitive***	insensitive

The gantry is asymmetric about the y-axis, since the guideway is located on the left with the beam extending to the right. Temperature changes will expand the beam, which will shift the x-axis encoder scale. Therefore the gantry is sensitive to thermal changes along the x-axis. Since the gantry is symmetric about the x-axis and the encoder heads are located along the axis of symmetry, the gantry is insensitive along the y-axis. The worktable structure is symmetric about both axes and is therefore, insensitive to thermal changes.

The encoder scales are sensitive along their direction of measurement. This is due to the glass scale expanding as the temperature increases. The coefficient of thermal expansion for the glass scale is 8 ppm/°C. The scales are held in a floating mounts, hence in this analysis they are assumed to be fixed in the middle with both ends expanding outwards. With a range of travel of 150 mm to each side, the error will be 1.35 μm/°C at the furthest position from center. The gantry beam has a coefficient of thermal expansion of 17.3 ppm/°C and it is assumed to be fixed at the left side. The

distance from the left side of the beam to the center of the x-axis encoder scale is the 360 mm. Therefore, the scale will move 6.23 ppm/°C.

Table 3-8 summarizes the magnitude of error for areas listed in Table 3-7.

Table 3-8. Magnitude of error due to thermal changes.

	X [ppm/°C]	Y [ppm/°C]
Gantry	***6.23***	-
Worktable	-	-
Gantry encoder scales	-	***1.35***
Worktable encoder scale	***1.35***	-

To help reduce thermal error due to environmental changes, the laboratory which contains the precision stage was recently converted to be temperature controlled with proportional (p-type) control. The temperature of the room was recorded for 6.5 weeks and the data is displayed in the Figure 3-23. The spikes correspond to night/day and the presence of people in the laboratory.

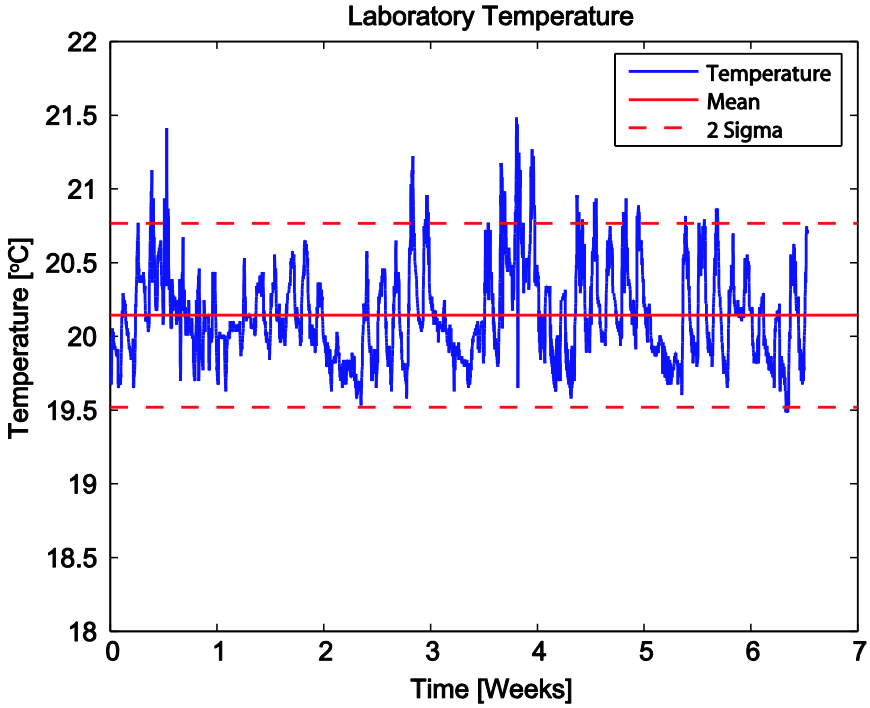

Figure 3-23. Laboratory temperature with mean and standard deviation bounds

The data was analyzed and the results are presented in the following table

Table 3-9. Temperature data of laboratory.

	[°C]
Maximum	21.48
Minimum	19.48
Range	2.00
Mean	20.14
Standard Deviation	0.312

The goal is to have the room maintain a constant temperature of 20°C ± 0.2°C which the controller is currently not achieving. It is believed that a digital proportional-integral controller will improve the accuracy of the temperature control, particularly in coping with internal and external disturbances due to room occupancy and outside temperature changes.

As mentioned in Section 3.3, internally cooled couplings are designed to remove any heat generated by the linear motors. The y-axis couplings were designed by Carlton Banks as a 4th year design project [33]. The purpose was to design the coupling such that the heat dissipated by the motor would be removed by the glycol, which is cycled through the internal channels of the coupling. The criteria for the design for the x and y-axis couplings are:

1. Align, position and secure the linear motor to the coupling
2. Align, position and secure the coupling to the stage
3. Include inlet and outlet ports for glycol
4. Configure internal cooling channels to dissipate the maximum heat generated by motor
5. Design must be leak proof under 100 psi internal pressure
6. Coupling must be handled as single unit (ie. The seal cannot be broken during disassembly of stage)

The y-axis design is presented in Figure 3-24.

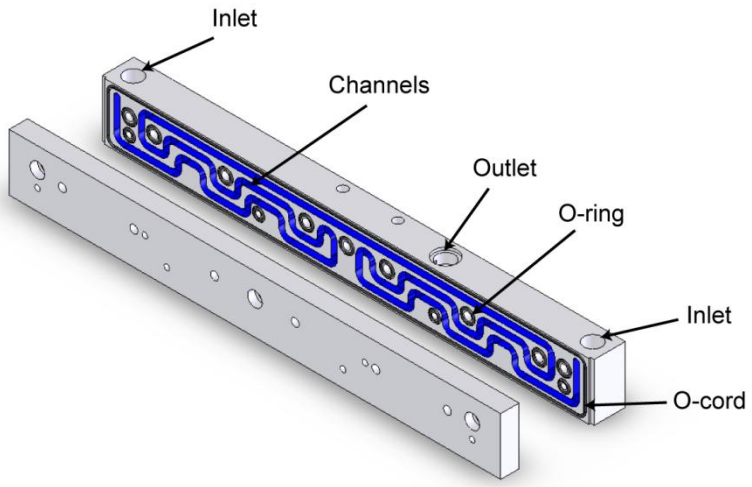

Figure 3-24. Y-axis coupling design

The x-axis coupling is presented in Figure 3-25.

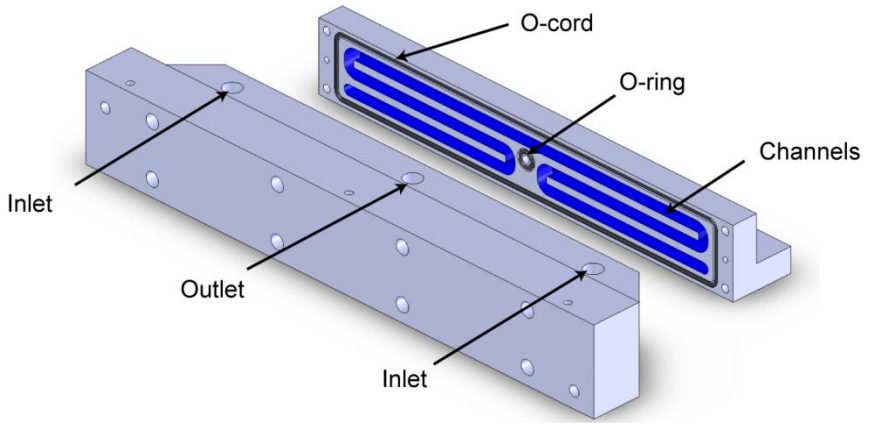

Figure 3-25. X-axis coupling design

The couplings were analyzed before production to verify their effectiveness to remove heat under maximum thermal loading. The following assumptions were used in the analysis:

- Uniform volumetric heating of the motor.
- All exposed surfaces of the motor and coupling are insulated (worst case).
- Constant and uniform heat transfer between the coupling and glycol.
- Glycol is always at 20°C.

The motors coils have a maximum heat dissipation of 131 W and volume of 214 cm^3. Therefore, they have a volumetric heating coefficient of 0.612 W/cm^3. Figure 3-26 displays the results of the analysis for the y-axis coupling. It is important to note the temperature of the surface which is in contact with the stage.

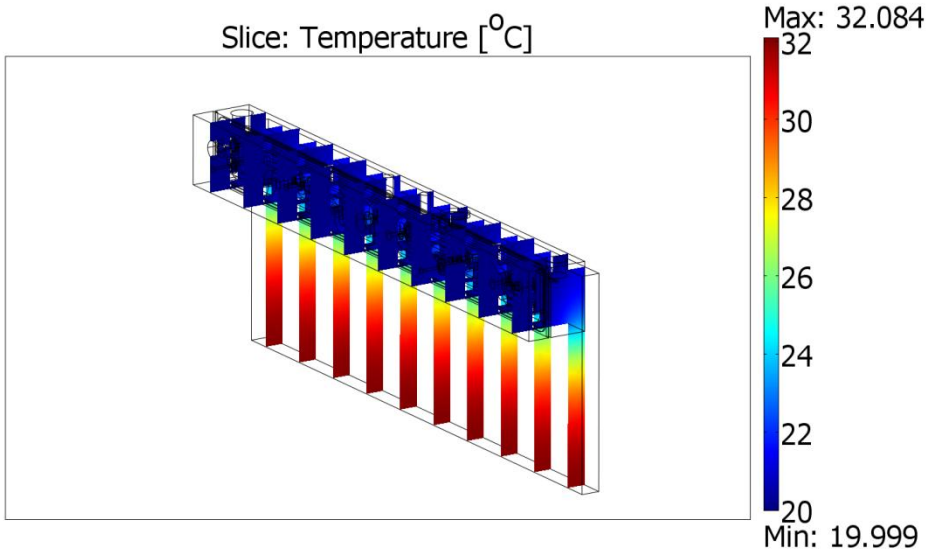

Figure 3-26. Thermal analysis of y-axis coupling

The same analysis was performed on the x-axis coupling, which is shown in Figure 3-27.

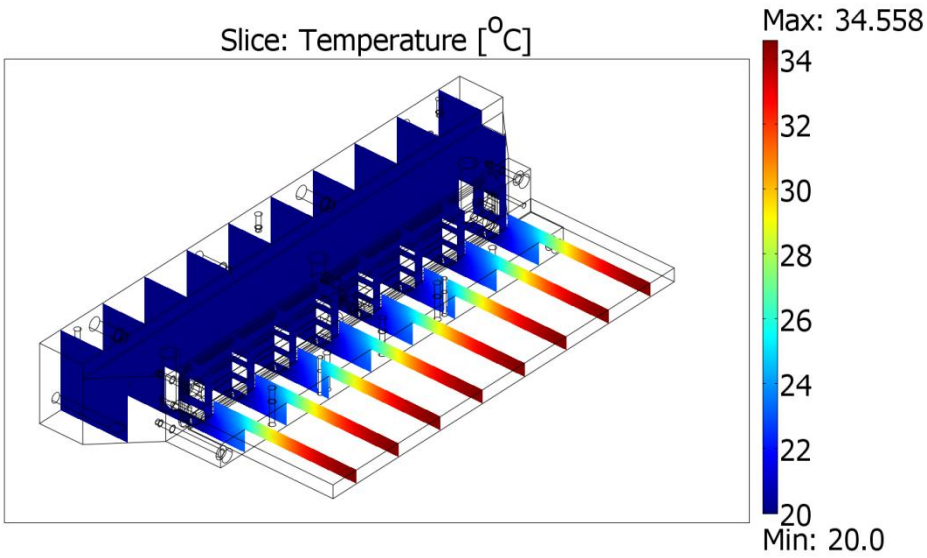

Figure 3-27. Thermal analysis of x-axis coupling

It can be seen from the figures that the surface in contact with the stage maintains a temperature of 20°C. Therefore, the effect of thermal errors from the motors can be considered negligible.

3.7 Error Budget

This section presents an error budget for the precision stage and outlines major sources of error for the machine [34]. The amount of error contributed by each source is quantified and critical areas are determined. Efforts can then be made to develop solutions to minimize individual errors. Each of the following sub-sections focuses on a particular source of error and attempts to quantify its impact on the overall accuracy. The reader is referred to Section 2.4 for definitions and a full explanation of linear, straightness and angular errors.

3.7.1 Linear Positional Error

The linear error for each axis consists of encoder scale error, the resolution of the encoders and the uncertainty of the encoder signal. The encoder scales have error from imperfections within the grating. Each encoder scale is tested for its positional error and a certificate with the error profile is provided to the customer. The scale error for the scales used with the stage is 0.79 µm. A resolution of 0.97nm is achieved by interpolating the 4 µm wavelength signal in 4096 sub-divisions. However, the uncertainty within one signal period is 0.044um, as provided by the manufacturer. The error within one signal period is critical for both the accuracy of positioning, as well as velocity control during a slow and constant velocity traverse of an axis. Metrology experiments can measure the encoder scale error and since these errors are mostly repeatable, compensation can be applied which

can reduce the error by 100 times. The uncertainty of the signal and encoder resolution cannot be compensated.

3.7.2 Straightness Error

Straightness error refers to the unwanted motion in one of the two directions orthogonal to the direction of a linear axis commanded to move along a (nominal) straight-line trajectory. Typically, these are referred to vertical and horizontal straightness errors. However, it depends on the setup of the system and its orientation within the machine. The straightness error is directly dependent on the geometry of the guideways. For the Y-axis, the gantry moves along the base granite surface and granite guideway. The X-axis is guided by the base granite surface and the stainless steel gantry beam. These surfaces were built with a specified tolerance of 2 μm/300 mm. Therefore the maximum expected straightness error is 2um since the range of travel is 300 mm. Straightness errors are repeatable and compensation of their error is possible. As with linear error, metrology measurements can determine the error profile which can be used to reduce the error.

3.7.3 Angular Error

Angular error refers to the three unwanted rotational movements of a moving component commanded to move along a (nominal) straight-line trajectory. Typically, these are referred to as yaw, pitch and roll errors. These errors are created from the contours of the guideways. The maximum angular error for each axis can be calculated from the maximum slope of the guideways which is 2 μm/300 mm or 6.7 nm/mm. To relate angular error to the other sources of error, it must be converted into linear units. This is accomplished by selecting a point of interest (usually the tool tip or reference point on a workpiece) and an axis of rotation for each angular degree of freedom. The distance between the two is the lever arm and then the angular errors can be converted into small linear displacements. The point of interest was chosen to be the center of the top plate of the worktable. The following assumptions are made when calculating the linear displacements.

- Pitch of the worktable contributes to displacement in y.
- Roll of the worktable contributes to displacements in x.
- Yaw of the worktable does not contribute to displacements.
- Pitch of the gantry does not contribute to displacements (since the gantry and table are vertically decoupled from each other).
- Roll of the gantry does not contribute to displacements (since the gantry and table are vertically decoupled from each other).
- Yaw of the gantry contributes to displacements in the y. Its x-axis error contribution is negligible due to it being a cosine error.

The point of rotation for pitch and roll of the worktable is assumed to be the center of the VPL surface which is in contact with the granite surface. And the yaw point of rotation will be about the torsional spring as mentioned in Section 3.4.

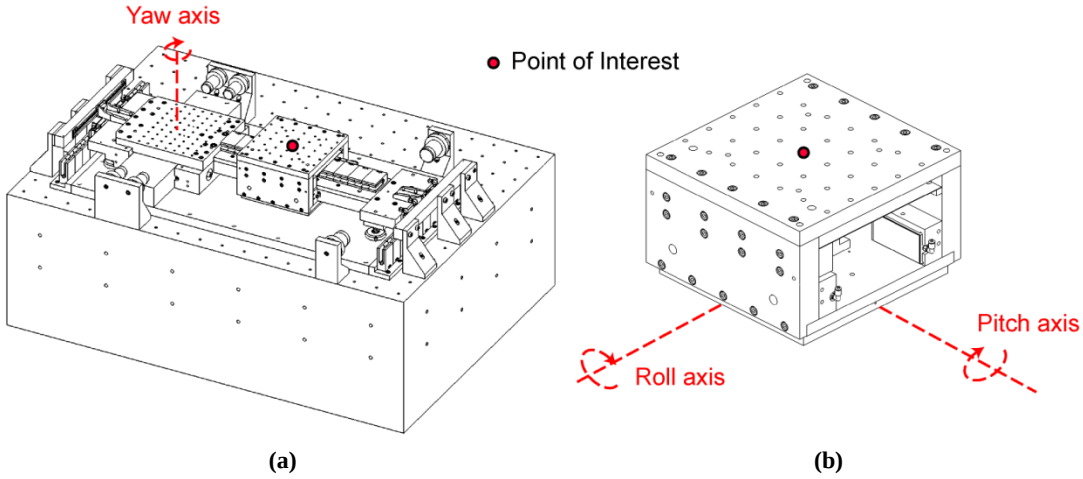

Figure 3-28. Point of interest for (a) yaw, (b) roll and pitch axes of rotation.

The rotation arm for pitch and roll is 200 mm and a maximum length of 650 mm for the yaw. The linear displacements due to angular error are 5.67 µm in the y direction and 1.34 µm in the x direction. Compensation of angular errors is possible with metrology tests if the machine has two additional rotary axes, which is the case for the designed machine with the trunnion (rotary-tilt) axes installed.

3.7.4 Dynamic Error

Dynamic errors occur from flexibility of machine components during acceleration and from external loading. Flexibility of the beam was analyzed in Section 3.5, which determined the static stiffness at the center of the beam in the y direction. Assuming an infinite servo static stiffness due to integral action, Table 3-6 gives an overall stiffness of 145 N/µm. During 0.2 g acceleration movement, the inertia of the worktable will provide an external load of 66 N to the beam. Therefore, the maximum deflection of the beam in the y direction will be:

$$v_y = \frac{66\ N}{145\ N/um}$$
$$v_y = 0.455\ um \tag{3.22}$$

A similar calculation is made for the x-axis. From Table 3-6 with an infinite servo static stiffness, an overall stiffness of 648 N/µm is given. The deflection in the x-axis during 0.2 g acceleration is:

$$v_x = \frac{66\ N}{648\ N/um}$$
$$v_x = 0.102\ um \tag{3.23}$$

Accelerating the worktable at 0.2 g along the y-axis is predicted to result in a displacement of 0.455 µm while a similar acceleration in x will result in a displacement of 0.102 µm. This deformation, however, is expected to be repeatable and will be modeled with the intention of applying real-time compensation. Additionally, the pitch of the gantry during 0.2 g acceleration will result in approximately 0.34 µm deflection of the encoder head in the y-axis.

3.7.5 Servo Error

Servo errors are a type of dynamic error which occurs during accelerations of the machine. It is also known as following error or tracking error. A simulation was performed to approximate the servo error expected for the x and y axes. A first order model with inertia and viscous friction coefficients was used to represent the mechanics of the system. The controller used is a Proportional-Integral-Derivative (PID) controller with feedforward acceleration and velocity. A reasonable controller bandwidth was chosen to be 30 Hz which is typical for most ball-screw drives. Higher bandwidth controllers (100 Hz) are possible with direct drive linear motors. However, the lower bandwidth was selected to represent a worst case and more realistic scenario. The feedforward estimates assume that the mass and friction values are identified with minimal uncertainty. A trajectory selected for the simulation is 200 mm travel, 0.2 m/s velocity, and 0.2 g acceleration with a 50 m/s^3 jerk-continuous profile. This trajectory will be used during actual tracking tests in Chapter 4. The results of the simulation are in Figure 3-29 and the peak servo error was found to be 0.1 µm for both axes.

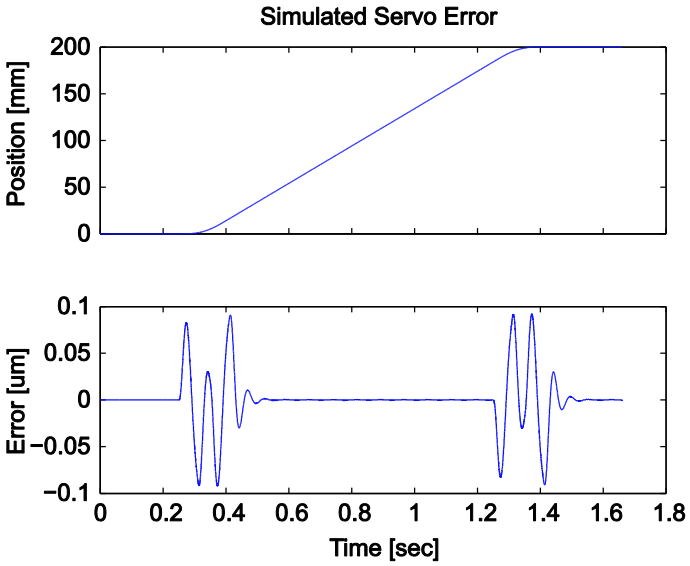

Figure 3-29. Simulated servo error

3.7.6 Thermal Error

A thermal analysis of the stage was performed in Section 3.6 which quantified how the stage expands with changes in temperature. It also verified the effectiveness of the cooling couplings which will remove the heat generated by the motors. The temperature of the environmentally controlled laboratory was recorded and plotted in Figure 3-23. The maximum range of temperature change was noted to be ± 1°C. Using this data in conjunction with Table 3-8, a maximum thermal error can be calculated. The error in the x direction consists of the expansion of the gantry beam and the worktable encoder scale. Therefore, a maximum error in the x direction is 7.58 µm and 1.35 µm in the y direction. However, further temperature control improvements are currently planned which will lower the temperature range to ± 0.2°C. Therefore, the error due to thermal change will be 1.52 µm in the x-axis and 0.27 µm in the y-axis.

3.7.7 Overall Error Budget

The error budget has been presented and a range of topics have been analyzed for their maximum contribution to error of the machine. Linear, straightness and angular errors were determined through geometric characteristics of the guideways while dynamic and thermal errors were calculated analytically. The results are presented in the following table which summarizes all of the errors for the x, y and z axes. [34]

Table 3-10. Predicted Error Budget.

	Error Magnitude (nm)					
	Without Geometry Compensation			With Geometry Compensation		
	X	Y	Z	X	Y	Z
Linear						
Encoder resolution	0.97	0.97		0.97	0.97	
Scale	790	790		79	79	
Encoder signal	44	44		44	44	
Straightness						
Y Guide	2000			200	200	
X Guide		2000	2000	200	200	200
Angular						
Y Guide	0	4330		0	433	
X Guide	1340	1340		134	134	
Dynamic (0.2 g acceleration)						
Servo	100	100		100	100	
Air Bearings	102	300		15	45	
Beam		155			23	
Gantry Pitch		340			51	
Thermal						
Friction	0	0	0	0	0	0
Drive System	0	0	0	0	0	0
Environment (20 ± 0.2°C)	1520	270	0	1520	270	0
Static Error						
Arithmetic Sum (E_A)	5695	8775	2000	2178	1361	200
RMS[1] Sum (E_R)	1206	1899	2000	635	229	200
Mean ((E_A + E_R)/2)	3451	5337	2000	1406	795	200
Maximum Resultant Error	**E_T = 5.87 µm**			**E_T = 1.63 µm**		
Static + Dynamic Error						
Arithmetic Sum (E_A)	5897	9670	2000	2293	1580	200
RMS Sum (E_R)	1046	1522	2000	551	186	200
Mean ((E_A + E_R)/2)	3471	5596	2000	1422	883	200
Maximum Resultant Error	**E_T = 6.11 µm**			**E_T = 1.69 µm**		

It can be seen that the largest contributor to the overall error of the machine environment thermal error. Further study into temperature control of the laboratory should be initiated in order to improve the accuracy of the machine.

[1] Assumes normal probability for each error about its mean value

[1] Compensation indicates the correction of repeatable geometric & dynamic errors by shifting the position

3.8 Conclusion

An ultra-precision planar stage concept and prototype has been designed and presented in this chapter. The T-type gantry and worktable configuration achieves an overall work area of 300 mm x 300 mm with a maximum velocity of 1 m/s and maximum acceleration of 1 g. The stage is supported by porous carbon air bearings on a precision ground granite base and actuation is achieved through direct drive linear motors with high resolution feedback of 1 nm. A VPL is utilized underneath the worktable to provide high vertical and pitch stiffness as well as decouple the gantry beam from vertical loads. A dynamic analysis of the gantry yielded a natural yaw frequency of 67 Hz and the first bending mode of the beam was calculated to be 190 Hz. These modes will be compared to experimental data in Chapter 4. The static stiffness of the machine was determined for the x and y axes by determining the servo, bearing and beam stiffness. Assuming the stiffness's act in series and the controller has integral action, a theoretical overall stiffness of 648 N/µm and 145 N/µm were calculated for the x and y axes respectively.

An additional thermal analysis was performed to quantify the effects of thermal influences on the machine structure and accuracy. The x-axis was identified to be most sensitive to thermal effects due to the elongation of the gantry beam and encoder scale. The maximum relative expansion coefficient was determined to be 7.58 µm/°C in the x direction and 1.35um/°C in the y. Internally cooled couplings were designed to mitigate thermal effects due to the linear motors. Their effectiveness was verified through finite element analysis which proved the couplings were successful at keeping the stage side of the coupling at 20°C.

An overall error budget was presented which combined geometric, dynamic and thermal errors to determine an overall error of the machine. With geometric compensation, the error was predicted to be 1.69 µm with the main contributor being thermal errors from the environment.

Chapter 4

Statics, Dynamics and Controls

4.1 Introduction

In this chapter, the dynamics are experimentally identified and high performance controllers are developed for the x- and y-axis drive systems. Section 4.2 focuses on the static stiffness of the axes and compares the findings to the theoretical stiffness values calculated in Chapter 3. Section 4.3 performs frequency domain identification experiments to characterize the dynamics of the stage. Parameter identification for models and controller design is performed in Section 4.4. A Multi-input-multi-output (MIMO) model is established for the y-axis due to the strong coupling between the primary and secondary motors. A loop-shaping controller for the x-axis is designed and a multivariable state-feedback controller is designed for the y-axis. The designs are verified through stability analyses and tracking tests. The conclusions are presented in Section 4.5.

4.2 Static Stiffness

In Section 3.5, a static stiffness analysis was performed, which attempted to analytically determine the stiffness of the stage in the x- and y-axes. Theoretical stiffness values were found to be 648 and 145 N/μm in the x- and y-axes respectively. The experimental stiffness values will be lower due to unaccounted flexibilities in the system. The actual static stiffness was measured using dead weights, which pull laterally on the stage via a cable and pulley system. The stiffness was measured along a grid pattern inside the workspace, simulating a load from a spindle located at the center of the workspace for the x-axis. The stiffness in the x-direction at each location was measured and is presented in Figure 4-1.

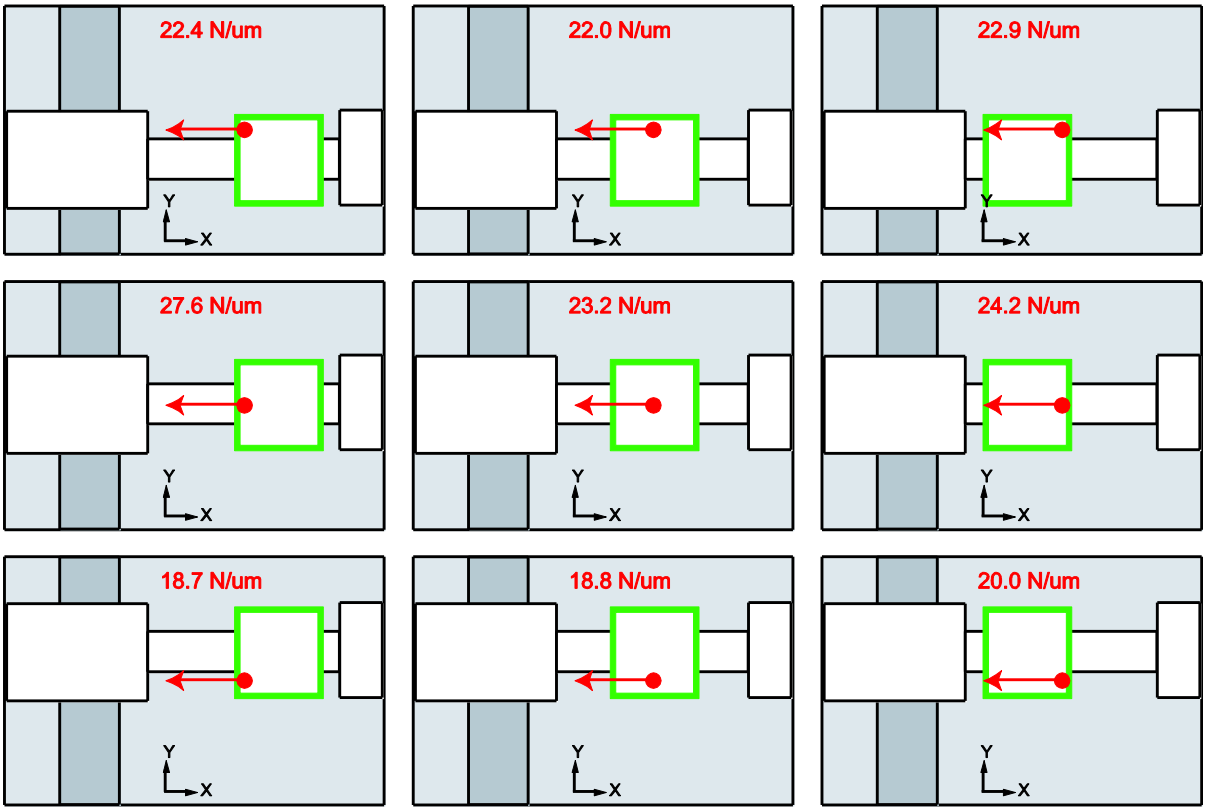

Figure 4-1. X-axis stiffness grid pattern and results

The stiffness in the y-direction at each location was measured and is presented in Figure 4-2.

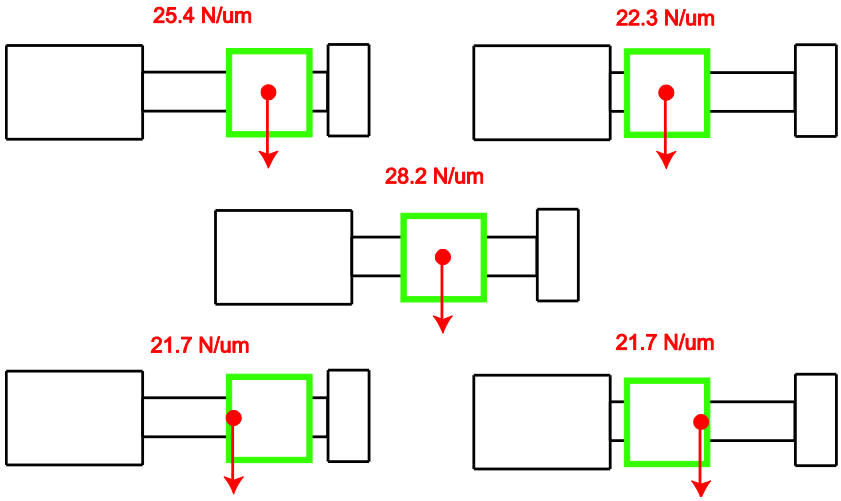

Figure 4-2. Y-axis stiffness grid pattern and results

The actual stiffness was measured to be much less than the theoretical stiffness. This is due to the pitch stiffness of the worktable and ultimately, the VPL and its bolted interface. The dead weight load is applied on the top surface of the worktable creating, a pitch load. Although this creates a moment on the table, it is a more realistic stiffness measurement since this is the location where cutting forces

would be applied. Stiffness tests were also performed with the vacuum for the VPL turned off. It was found that the VPL contributed 14.5 N/µm of stiffness which correlates to a pitch stiffness of $3.78x10^6$ Nm/rad. The theoretical stiffness analysis does not account for pitch stiffness of the worktable of VPL due to the complexity the analysis. Another contributor to lower stiffness is the x- and y- bearings not being cemented. There is likely relative movement between the spherical bolt head and the gap clearances allowing for more movement and less stiffness.

4.3 Frequency Response Measurement and Identification

Advanced controller design requires a well defined model of the system in order to understand the inertial characteristics, as well as any resonance frequencies which may cause instability of the servo loop. A Frequency Response Function (FRF) is an effective test which collects all of the required information to determine the parameters of the drive model. The test is performed by passing a wide range of frequencies (2 Hz – 3000 Hz) to the drives under open-loop. The position response is collected from the linear encoders and differentiated to produce the velocity and acceleration responses. The high quality signals allow for calculations up 3 kHz. The data is presented in a Bode plot showing the magnitude and phase relative to the input signal. The low frequency section (2 Hz – 100 Hz) of the magnitude plot is used to estimate the equivalent mass of the drive since rigid-body motion dominates the dynamics in this frequency range. Spikes in magnitude at certain frequencies are called resonances, which can cause undesired vibrations and even instability. Methods to reduce the resonance effects are discussed and implemented in Section 4.4.

The axes are controlled by a dSpace® controller with a sampling frequency of 20 kHz. The commercial controllers for the drives are used as straight amplifiers, which convert a ± 10 V analogue signal from the dSpace® into current for the motors. A programmable amplifier gain was selected to maximize the motor power capabilities with a slight safety margin. The motors have a peak current (I_p) of 27.7 A. However, a maximum of 25.45 A was selected to calculate the gain, which is 2.54 A/V. The input sine wave signal was selected to be strong enough to excite the dynamics of the machine while not too strong to damage any of the components. A peak-to-peak signal of ± 2 V was sent to the amplifiers to produce a 5.09 A peak-to-peak current signal. This resulted in ± 347 N in the x- and ± 694 N in the y-axis.

4.3.1 X-axis

The FRF measurement was performed on the x-axis and the acceleration FRF is presented in Figure 4-3.

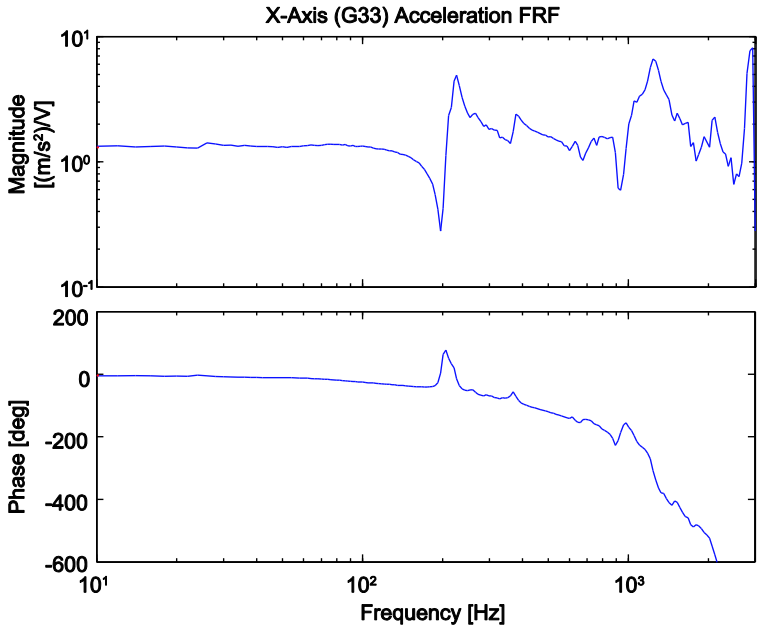

Figure 4-3. X-axis FRF

It can be seen in the magnitude plot that the FRF is flat up to ~200 Hz, where a zero and pole are present to create an anti-resonance and resonance. This mode is believed to be the result of the pitch motion of the worktable. This will be verified through dynamic impact testing using an instrumented hammer and an accelerometer. By testing the impact response at different locations on the worktable, the physical motion of the table will emerge by analyzing the magnitude and phase of the response. Combining the results from all locations will characterize the motion of the table. A second mode, albeit small, is present at 377 Hz, while a third mode is present at 1240 Hz. The sources of these other modes is currently unknown to the author, however, impact testing could provide insight into the type of vibration at those frequencies as well.

4.3.2 Y-Axis

The y-axis is more complex than the x-axis due to the multi-input-multi-output (MIMO) system configuration of the two linear motors and encoders. As well, the asymmetric design of the gantry creates many dynamic modes not seen with the x-axis FRF. Two FRF experiments were performed which capture the direct transfer functions (i.e. Left motor, left encoder; right motor, right encoder) and cross transfer functions (i.e. Left motor, right encoder; right motor, left encoder) for both motors. Therefore, four transfer functions are collected in total to create a 2×2 MIMO transfer function. Equation (4.1) illustrates the open loop model used for identification.

$$\begin{bmatrix} x_1 \\ x_2 \end{bmatrix} = \begin{bmatrix} G_{11} & G_{12} \\ G_{21} & G_{22} \end{bmatrix} \begin{bmatrix} u_1 \\ u_2 \end{bmatrix} \tag{4.1}$$

Actuation of the left motor (u_1) while capturing the position feedback of both encoders will allow the calculation of G_{11} and G_{21}. Actuating the right motor (u_2) will provide the remaining two transfer functions. It was found during experimentation that the dynamic response of the gantry is dependent on the position of the worktable. Figure 4-4 presents the four transfer functions for the gantry with the worktable at its center position (x = 150 mm).

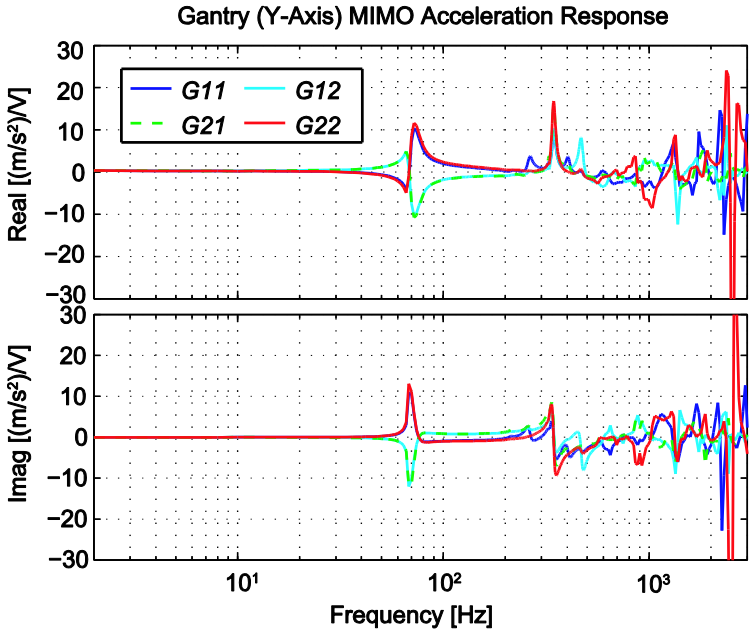

Figure 4-4. Y-axis direct and cross FRF's

A resonance is clearly seen at 68 Hz for all transfer functions, which corresponds to the rigid body oscillations about the four pre-loaded air bearings as discussed in Section 3.4. The analytical model calculated a natural frequency of 67 Hz for the worktable at its center position. The next significant resonance occurs at 344 Hz, which is dependent on the position of the x-axis. An analytical model has not been successfully created to characterize this mode. However, a speculation is that it is one of the bending modes of the gantry assembly. The mode is best seen in G_{21}, which was measured with the worktable at three positions over the full range of travel. Figure 4-5 shows the dependence of this resonance frequency on the position of the worktable. The 68 Hz mode, on the other hand, was not strongly affected by the table x-axis position. This is due to the table's mass having a smaller influence on the moment of inertia of the gantry about the center of the four pre-loaded air bearings acting on the granite guideway.

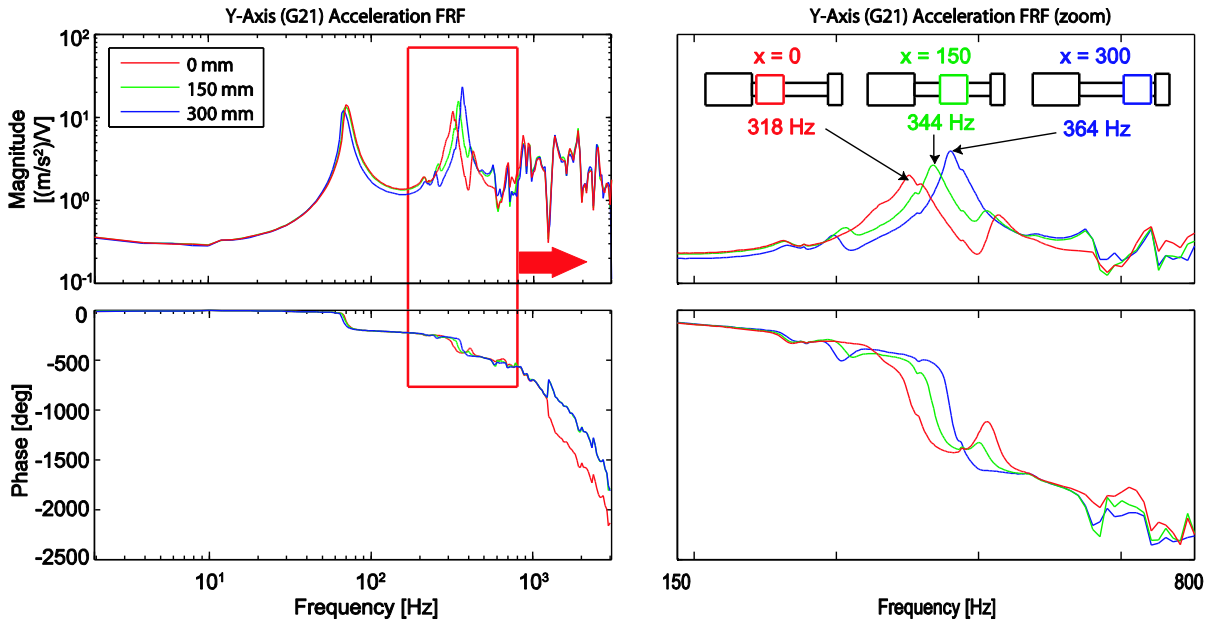

(a) **(b)**

Figure 4-5. Y-axis FRF dependence on worktable position. (a) 2 – 3000 Hz, (b) 150 – 800 Hz

The frequency shifts from 318 Hz at x = 0 mm to 364 Hz at x = 300 mm. A third resonance occurs at 472 Hz.

4.4 Controller Design

This section discusses the controller design for the x- and y-axes of the stage. The FRF's measured in Section 4.3, were used to fit models using least squares parameter estimation.

4.4.1 Parameter Identification

The y-axis parameter identification and control design were performed together with Daniel Gordon who is enrolled in the Master's program and the University of Waterloo. Identification was also completed with the aid of Dr. K. Erkorkmaz. The material presented in this section is a summary of the experimental measurements that were obtained. A model of the x-axis is described in Equation (4.2).

$$M\ddot{x} + c\dot{x} + kx = F \tag{4.2}$$

Where,

- x is the position (m)
- M is the mass (kg)
- c is the viscous coefficient (kg/s)
- k is the stiffness coefficient (kg/s^2)
- F is the applied force (N)

Since the construction of the x-axis uses air bearings and direct drive linear motors, the contributions of c and k are assumed negligible. The model in the Laplace domain becomes,

$$ms^2x(s) = u(s)$$
$$\frac{x(s)}{u(s)} = \frac{1}{ms^2} \tag{4.3}$$

Where,

- x is the position (m)
- m is the equivalent inertia $(V/(mm/s^2))$
- u is the control signal (V)

The equivalent inertia was found by fitting Equation (4.3) to the FRF in Figure 4-3, which was determined to be 7.513x10^{-4} $(V/(mm/s^2))$. The model is overlaid on top of the FRF to compare its fit, which can be seen in Figure 4-6. The model fits well up to 100 Hz after which, it does not incorporate the dynamic modes present in the experimental FRF.

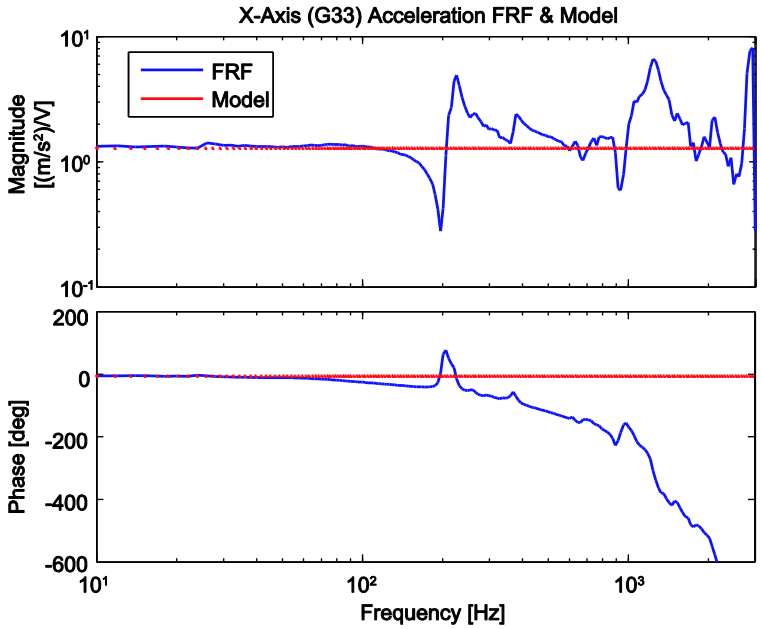

Figure 4-6. X-axis FRF with identified model

A MIMO model is used to identify the characteristics of the y-axis. Equation (4.4) is the model presented in the Laplace domain. The cross terms of the matrices are assumed to be identical, making the matrices symmetric. [35]

$$\begin{bmatrix} m_{11} & m_{12} \\ m_{21} & m_{22} \end{bmatrix} s^2 \begin{bmatrix} x_r(s) \\ x_r(s) \end{bmatrix} + \begin{bmatrix} c_{11} & c_{12} \\ c_{12} & c_{22} \end{bmatrix} s \begin{bmatrix} x_r(s) \\ x_r(s) \end{bmatrix} + \begin{bmatrix} k_{11} & k_{12} \\ k_{12} & k_{22} \end{bmatrix} \begin{bmatrix} x_r(s) \\ x_r(s) \end{bmatrix} = \begin{bmatrix} u_1(s) \\ u_2(s) \end{bmatrix} \tag{4.4}$$

The model is fit using a least squares methodology using the data between 2 Hz and 100 Hz, which includes the low frequency and first mode characteristics. The identified parameters are the following:

$$\begin{aligned} M_{est} &= \begin{bmatrix} 9.40 & 4.64 \\ 4.64 & 8.74 \end{bmatrix} \times 10^{-4} \\ C_{est} &= \begin{bmatrix} 4.49 & -4.49 \\ -4.49 & 4.49 \end{bmatrix} \times 10^{-3} \\ K_{est} &= \begin{bmatrix} 4.25 & -4.25 \\ -4.25 & 4.25 \end{bmatrix} \times 10^{1} \end{aligned} \tag{4.5}$$

The identified parameters are then used to plot an estimated FRF and are overlaid on top of the experimental FRF to examine their fit. Figure 4-7 shows the fit for each transfer function.

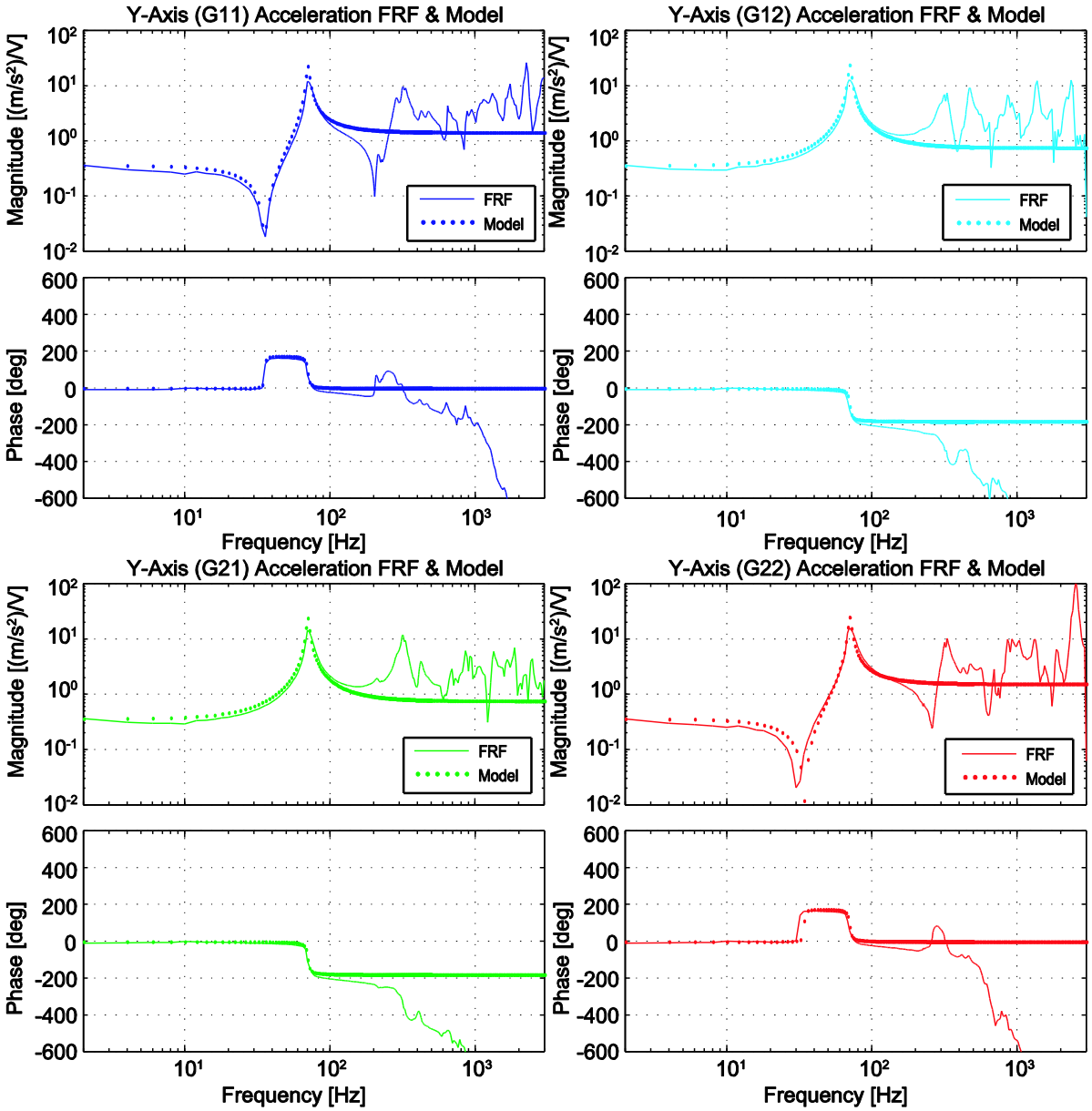

Figure 4-7. Y-axis direct and cross FRF's and models

The identified parameters fit well up to 100 Hz, capturing the first mode with an overall RMS fit error of 0.779 $((mm/s^2)/V)$. The model is useful for tracking test simulations and stability analysis in the low frequency range. However, full stability analysis is conducted by considering the experimentally measured FRF's.

4.4.2 X-Axis

The controller design for the x-axis was completed using the internal hardware structure of the ETEL® digital controllers. The structure consists of a proportional-integral-derivative (PID)

controller with feedforward acceleration and velocity terms. A Loop shaping design methodology was implemented to manipulate the Loop transfer function of the x-axis [36].

Filters were applied to attenuate the other resonances and high frequency dynamics. A notch filter was applied at 220 Hz to reduce the magnitude of the resonance at that frequency. A 2nd order low pass filter was located at 1200 Hz, to mitigate high frequency dynamics. Once the filters are applied, the loop transfer function can be manipulated to achieve a desired closed-loop response. The bandwidth of the controller is the highest frequency at which a system can maintain an acceptable level of control. It occurs approximately when the magnitude of the loop transfer function has a value of 1 at 0 dB. Denoted as the cross over frequency, a controller can be designed to achieve a desired bandwidth within the dynamic capabilities of the system. The x-axis was designed to have a crossover frequency of 100 Hz, which is relatively high for machine tool drives.

The Nyquist plot of the loop function is presented in Figure 4-8(a). It can be seen the loop does not approach the instability point $(-1 + 0j)$, and has a positive phase margin of 25°, showing that the system is stable. The closed loop sensitivity function is shown in Figure 4-8(b) with a maximum sensitivity of 2.6 at approximately 100 Hz. This is slightly aggressive, which is due to a phase margin less than 30°, however, it favours better tracking accuracy and is still within acceptable limits for high precision machines.

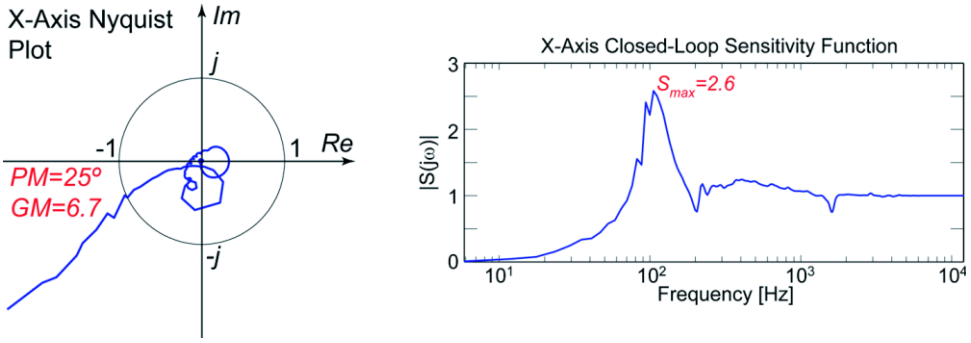

(a) **(b)**

Figure 4-8. X-axis (a) Nyquist and (b) Sensitivity plots

High speed and low speed tracking experiments were performed to analyze the dynamic capability of the drive. The low speed test is performed at 20 mm/s feed, 0.25 m/s^2 acceleration and 5 m/s^3 jerk similar to Figure 3-15. The results are shown in Figure 4-9(a) with a maximum error profile mimicking the commanded jerk profile. The peak error was recorded to be 1.62 µm. The error during constant feed motion is less than 410 nm. The high speed experiment was performed at 200 mm/s feed, 2 m/s^2 acceleration and 50 m/s^3 jerk. The results are shown in Figure 4-9(b).

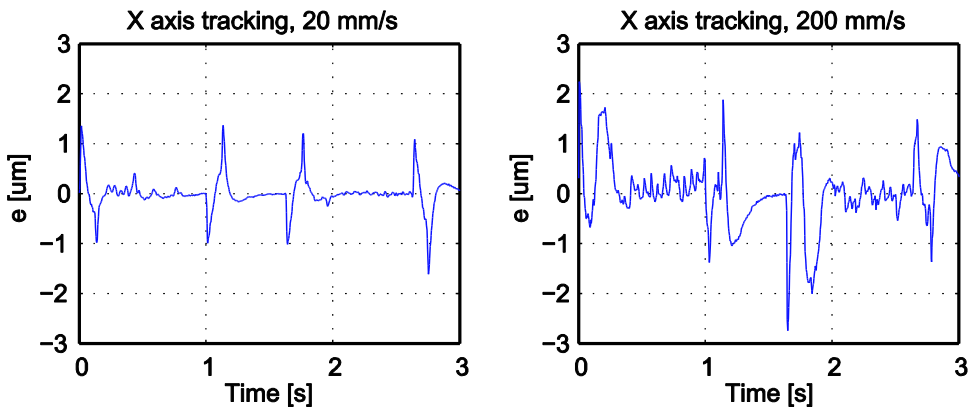

(a) **(b)**

Figure 4-9. X-axis (a) low speed and (b) high speed tracking results

The peak error was recorded to be 2.74 µm, which again seemed to be synchronized with the peaks of the commanded jerk profile. The constant feed error was measured to be less than 710 nm. The position holding accuracy was analyzed by recording the tracking error during no movement. Figure 4-10 displays the error, which has a maximum of 26 nm and an RMS value of 8 nm.

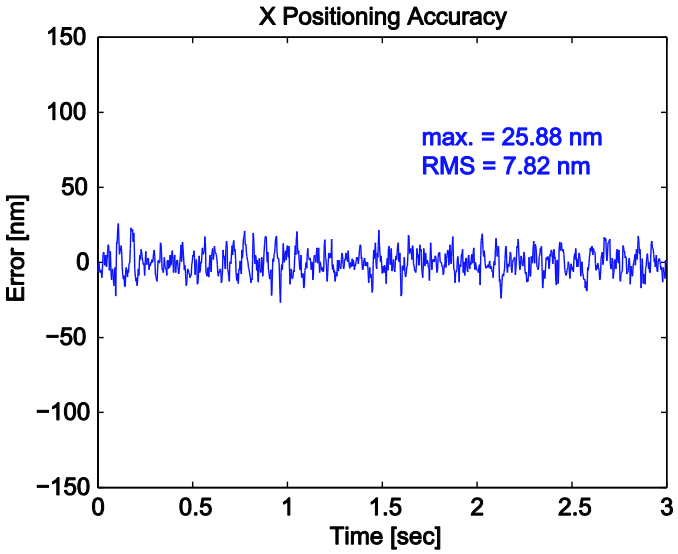

Figure 4-10. X-axis positioning accuracy

4.4.3 Y-Axis

The controller design of the y-axis was performed by Daniel Gordon in conjunction with his Master's study and the University of Waterloo. The material presented in this section is a summary of his work and the results he achieved on the designed machine stage.

The developed controller is shown in Figure 4-11. The variation of y-axis dynamic due to the x-axis position was considered in notch filter design, which will be gain scheduled depending on the x-axis location of the worktable.

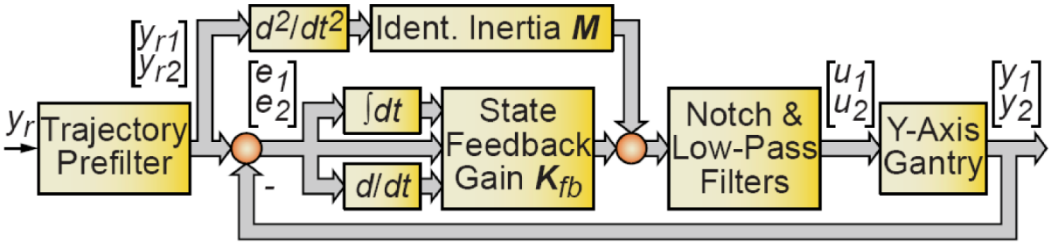

Figure 4-11. Y-axis controller state feedback design

Position measurements $[y_1, y_2]$ from the encoders are utilized in a state feedback scheme. The state vector comprises of the tracking error and their time integrals and derivatives: $x' = [\int e_1 dt, \int e_2 dt, e_1, e_2, \dot{e_1}, \dot{e_2}]$. The feedback gain has the following structure:

$$K_{fb} = \left[\underbrace{K_i}_{integral\ \ action} \;\middle|\; \underbrace{K_p}_{proportional\ \ gain} \;\middle|\; \underbrace{K_d}_{damping} \right]_{2x6} \tag{4.6}$$

To compute K_{fb}, first a PD controller is designed in the form $k_p + k_d s$, based on a desired natural frequency ω_n and damping ration ζ. Considering the gantry as a rigid body:

$$k_p = m\omega_n^2 \;\;,\;\; k_d = 2\zeta\omega_n m \tag{4.7}$$

On the setup, $\omega_n = 40$ Hz and $\zeta = 1.2$ were used. This controller uses the center of mass position estimated from the two encoders: $\bar{y} = \alpha_1 y_1 + \alpha_2 y_2$; $\alpha_1 = m_1/(m_1 + m_2)$, $\alpha_2 = m_2/(m_1 + m_2)$. Its output $(\bar{u})$ is distributed to the motors proportionally to the mass they actuate: $u_1 = \alpha_1 \bar{u}$, $u_2 = \alpha_2 \bar{u}$. Hence, K_p and K_d become:

$$K_p = k_p \begin{bmatrix} \alpha_1^2 & \alpha_1\alpha_2 \\ \alpha_1\alpha_2 & \alpha_2^2 \end{bmatrix}, \quad K_d = k_d \begin{bmatrix} \alpha_1^2 & \alpha_1\alpha_2 \\ \alpha_1\alpha_2 & \alpha_2^2 \end{bmatrix} \tag{4.8}$$

This scheme results in the yaw mode (68 Hz) to nearly vanish from the averaged transfer function being controlled ($\bar{G} = \alpha_1^2 G_{11} + \alpha_1\alpha_2(G_{12} + G_{21}) + \alpha_2^2 G_{22}$) as seen in Figure 4-12; without suffering from the phase lag associated with notch filtering a vibration mode. This allows the control performance to be significantly improved, by mitigating the negative effect of the yaw mode on closed loop stability, similar to the approach in [37].

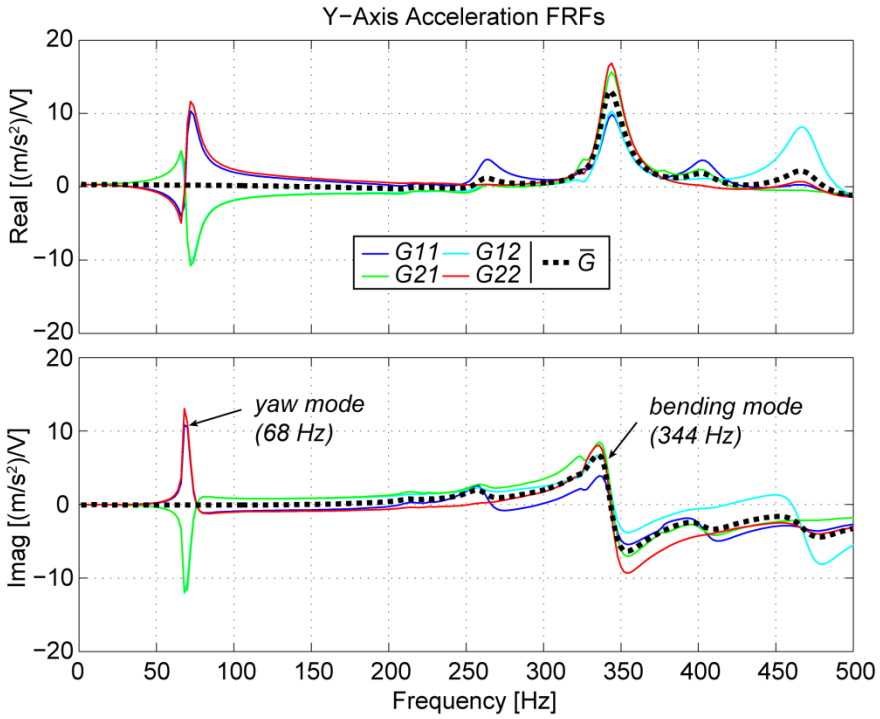

Figure 4-12. Y-axis open loop acceleration FRF's

K_i is designed to eliminate steady state errors at the servo level rather than the center of mass. This is because opposing servo errors may give the false impression that the center of mass positioning error is zero. Hence,

$$K_i = k_i \begin{bmatrix} \alpha_1 & 0 \\ 0 & \alpha_2 \end{bmatrix}, \qquad where: \;\; k_i < \frac{k_p k_d}{m} \; for\; stability \tag{4.9}$$

The above stability limit comes from applying the Routh-Hurwitz criterion, assuming rigid body dynamics. The practical limit, however, was found to be lower due to machine base vibrations occurring around 22 Hz.

Also, active damping is injected to attenuate the yaw vibrations, which may be excited by external disturbances. This was a crucial step in furthering the stability margins, which also enabled higher control bandwidth and dynamic stiffness to be achieved. Active damping is designed to emulate a torsional damper, which increases the yaw damping by 32 times. Its output is distributed to the drives by their mass rations. Hence, the final form of K_d becomes:

$$K_d = \underbrace{k_d \begin{bmatrix} \alpha_1^2 & \alpha_1\alpha_2 \\ \alpha_1\alpha_2 & \alpha_2^2 \end{bmatrix}}_{\substack{Derivative\;\; Action\;\; for \\ CoM\;\; control}} + \underbrace{c \begin{bmatrix} \alpha_1 & -\alpha_1 \\ -\alpha_2 & \alpha_2 \end{bmatrix}}_{\substack{Active\;\; damping\;\; to \\ attenuate\;\; yaw\;\; vibrations}} \tag{4.10}$$

Additional filters were also inserted to stabilize the closed loop and avoid poor robustness at certain frequencies. These filters were designed by applying multivariable stability and sensitivity analyses. Considering the experimentally recorded open loop position frequency response matrix $G(j\omega)$, and the feedback controller frequency response $K(j\omega)$ computed analytically, the multivariable loop transfer function matrix can be constructed as $L(j\omega) = G(j\omega)K(j\omega)$ as seen in Equation (4.11).

$$\begin{bmatrix} L_{11}(j\omega) & L_{12}(j\omega) \\ L_{21}(j\omega) & L_{22}(j\omega) \end{bmatrix} = \begin{bmatrix} G_{11}(j\omega) & G_{12}(j\omega) \\ G_{21}(j\omega) & G_{22}(j\omega) \end{bmatrix} \begin{bmatrix} K_{11}(j\omega) & K_{12}(j\omega) \\ K_{21}(j\omega) & K_{22}(j\omega) \end{bmatrix} \tag{4.11}$$

Stability is guaranteed when the locus of $\det\{I + L(j\omega)\}$ makes no counter-clockwise encirclements of the origin in the complex plane [38]. Also, the maximum singular value of the sensitivity function $\left(\bar{\sigma}\big(S(j\omega)\big) = \bar{\sigma}\left\{\big(I + L(j\omega)\big)^{-1}\right\}\right)$ was inspected as a margin of robust stability. This is useful for determining the critical frequencies that need to be low pass or notch filtered. When the feedback design was complete, the cross over frequency was 100 Hz and the peak sensitivity 2.64. To enhance the command tracking, inertial forces were also compensated as shown in the controller design in Figure 4-11. In addition, a trajectory pre-filter was designed to remove the correlations of velocity, acceleration, jerk and snap (4th derivative) commands from the tracking error. This filter was tuned by conducting a single tracking experiment and using least squares fitting to identify its coefficients.

The contribution of active damping can be observed in the sensitivity plot in Figure 4-13. When active damping is disabled, the gantry goes into yaw vibrations at the 68 Hz. This is also confirmed by the high sensitivity $\left(\bar{\sigma}\big(S(j\omega)\big)\right)$ prediction around this frequency. When active damping is turned on, the sensitivity peak reduces from 4.46 to 2.65 and shifts from 68 Hz to 104 Hz.

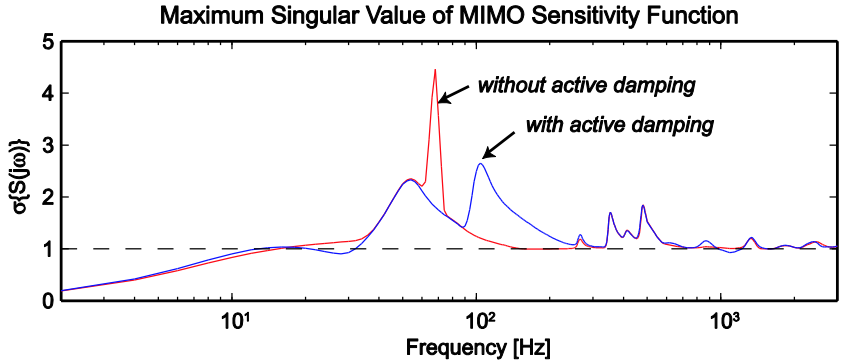

Figure 4-13. Y-axis sensitivity plot

The tracking tests in Figure 4-14 were conducted with the 200 mm/s trajectory. The trajectories are similar to Figure 3-15, however: Jerk is parabolic, Acceleration is cubic, Velocity is quartic, and

Position is quintic. To retain stability in the absence of active damping, the servo was detuned, which explains the higher tracking errors.

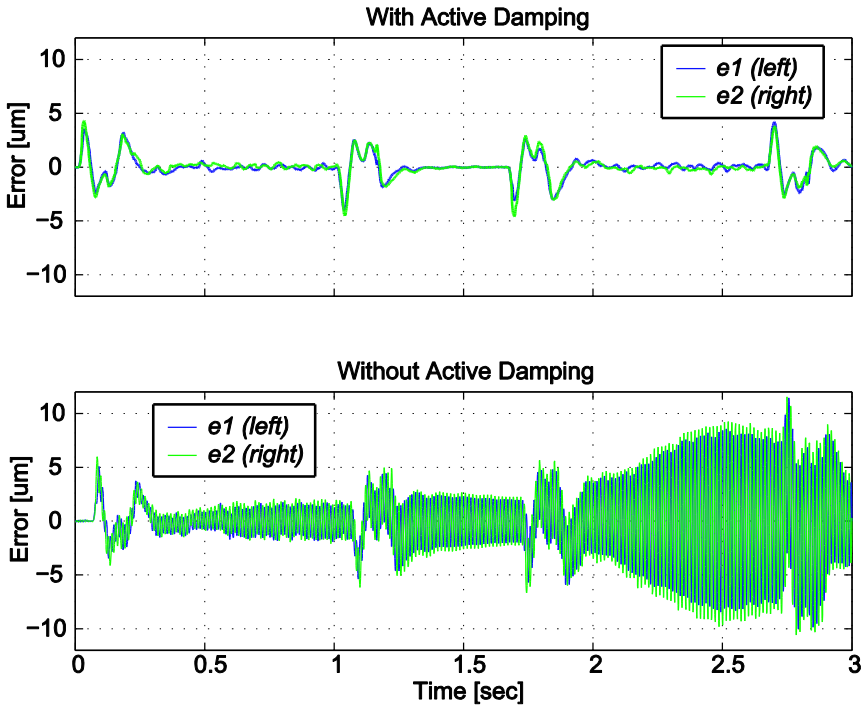

Figure 4-14. Contribution of active vibration damping on y-axis control

Servo performance experiments were performed on the y-axis. The low speed (20 mm/s) tracking error results are shown in Figure 4-15(a). A maximum error of 1.45 µm is observed, with a constant feedrate error less than 100 nm. The high speed (200 mm/s) results are shown in Figure 4-15(b) with a recorded peak error of 2.41 µm, which corresponds with the snap profile in the commanded trajectory. The constant feed error is measured to be less than 400 nm.

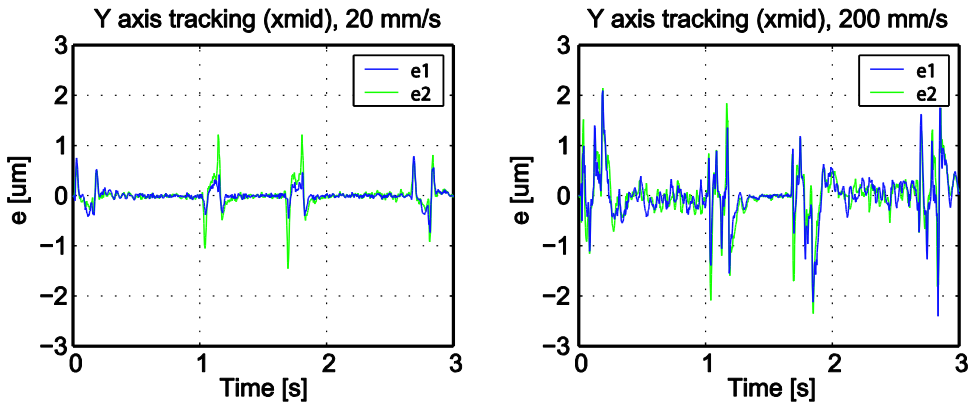

(a) **(b)**

Figure 4-15. Y-axis (a) low speed and (b) high speed tracking results

Position holding accuracy was analyzed as well and is presented in Figure 4-16. The peak error for the left motor is 65 nm with an RMS error of 23 nm. The right motor has a peak error of 104 nm with an RMS error of 30 nm.

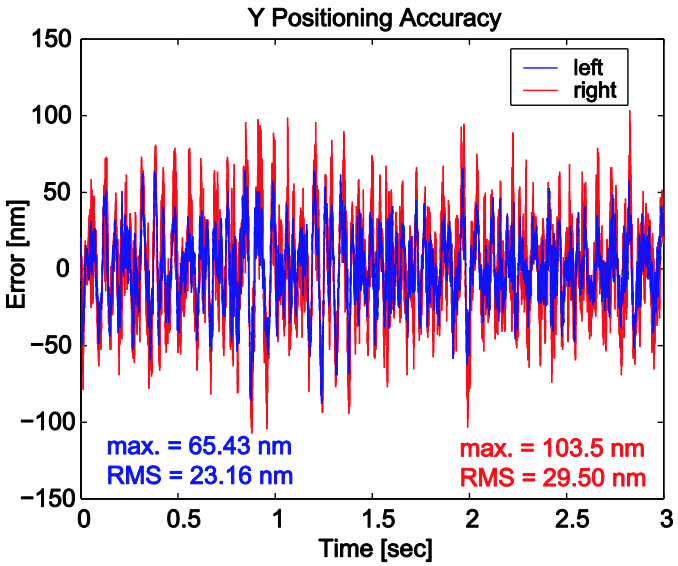

Figure 4-16. Y-axis positioning accuracy

If the y-axis were controlled with independent PID controllers, the achievable crossover frequency would be 16.4 Hz and the active disturbance rejection band 8.2 Hz, which is an order of magnitude less than that achieved with the developed multivariable design. Hence the design necessitates MIMO control with active damping.

4.5 Conclusions

This chapter presented the static stiffness of the x and y axes with a comparison to analytically calculated stiffness from Chapter 3. The experimental stiffness values as measured at the top of the worktable are 22.2 N/µm and 23.9 N/µm in the x- and y-axes respectively. Frequency response function (FRF) measurements were performed to characterize the dynamics of the machine. The results were used to identify model parameters through the least squares estimation method. Controllers for the two axes were developed, using a loop shaping method for the x-axis and a multivariable state feedback method for the y-axis. High and low speed tracking tests were conducted and the errors were recorded. The peak error for the low speed tests were 1.62 µm and 1.45 µm for the x- and y-axes respectively. The high speed tests resulted in 2.74 µm in the x-axis and 2.41 µm in the y-axis. The RMS holding accuracy of the x-axis is 7.82 nm, and 23.16 nm and 29.50 nm for the y-axis left and right motors respectively. These results indicate that reasonably uniform stiffness and servo performance has so far been obtained on the machine tool. It is believed that cementing the

bearings will increase stiffness as well as servo performance. MIMO control and active damping are crucial for achieving high accuracy with the developed gantry design.

Chapter 5

Metrology of Precision Stage

5.1 Introduction

In this chapter, metrology experiments are performed to measure geometric errors of the x and y axes. Measurements are performed using a laser interferometer in accordance with international metrology standards. The setup for each test is outlined in Section 5.2, with an explanation of Abbe error in Section 5.3 and how it contributes to measured errors. Section 5.4 focuses on the linear positional error while Section 5.5 examines straightness errors. Finally, Section 5.6 presents the angular errors for each axis. Each test is performed at three locations along each axis to produce an error map of the machine.

5.2 Experimental Setup

The error measurements were performed using laser interferometry with different optics for each type of error. This section goes through the five setups for geometric errors. Roll is not presented in this chapter due to the unavailability of equipment. Squareness is also absent due to electronic issues with the laser setup at the time of testing. However, they will be required to fully map the errors of the machine and apply proper error compensation.

5.2.1 Linear Positioning Error Setup

The equipment required for the linear error tests are a 90° laser head with an internal reference retro-reflector and a retro-reflector located on the moving worktable. Figure 5-1 shows the x-axis setup, which is similar for the y-axis.

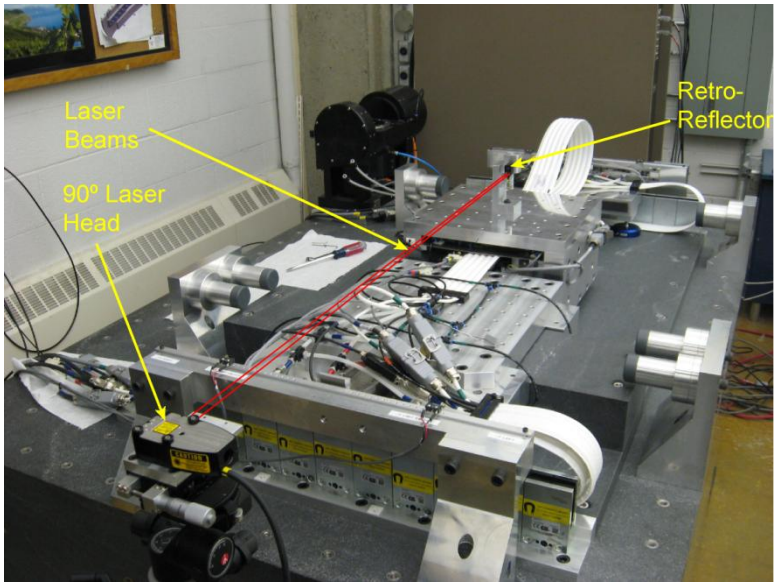

Figure 5-1. Linear positioning error setup

5.2.2 Straightness Error Setup

The equipment required for the straightness tests include a 0° laser head without internal optics, a Wollaston prism and a short range straightness retro-reflector. The prism is located on the moving stage while the reflector is stationary and is located on the far end of the machine. The setup is similar between vertical and horizontal measurements with all components rotated by 90°. Figure 5-2 shows the setup for the y-axis horizontal straightness measurement.

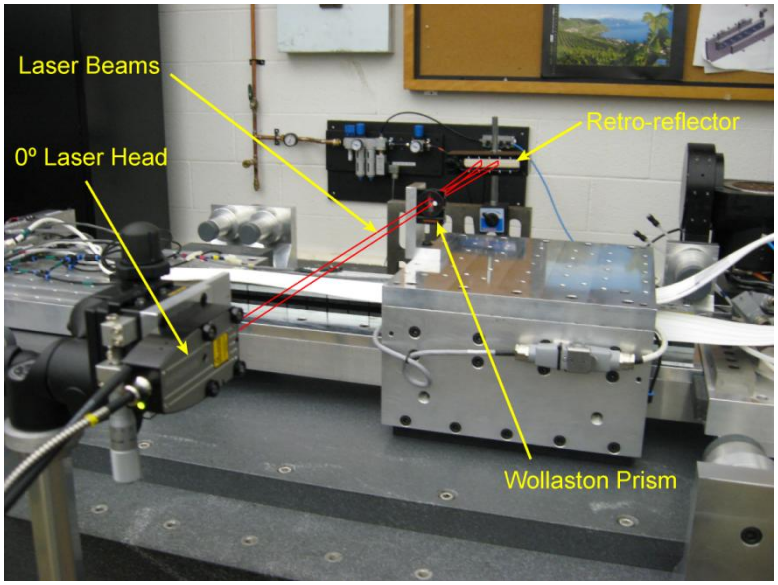

Figure 5-2. Straightness error setup

5.2.3 Angular Error Setup

The equipment required for the angular tests include a 0° laser head without internal optics, an angular interferometer, and an angular retro-reflector. The interferometer is stationary and is located between the laser head and reflector. The reflector is located on the moving stage. The setup is similar between yaw and pitch measurements with the optics rotated by 90°. Figure 5-3 shows the setup for the x-axis pitch measurement.

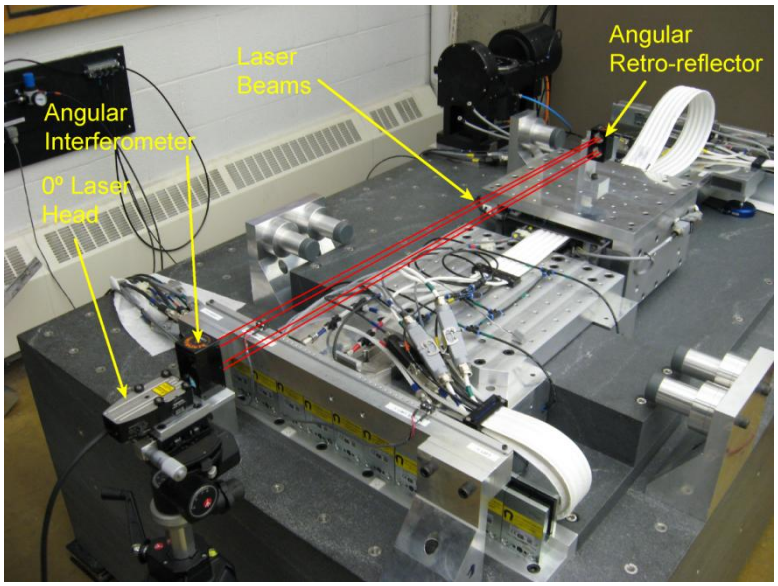

Figure 5-3. Angular error setup

5.3 Abbe Error

Abbe error is a measurement effect observed by the amplification of angular errors in a linear form. Abbe error is also called sine error as it is calculated by the sine of the angle multiplied by the length of a lever arm. To calculate actual positioning error, the contribution of Abbe error must be removed to reveal the true error. Angular errors can be accurately measured by a laser interferometer which leaves the difficult task of determining the lever arm lengths. There is no elementary method to determine the arm length, therefore educated approximations of the location of the axes of rotation are used. The assumptions for these lengths are explained in this section.

Linear positioning error is affected by pitch and yaw motions of the stage and is insensitive to roll. The pitch error for both axes is created by the curvature of the top granite surface and it is assumed that the axis of rotation is located on this surface. However, slight modifications of this assumption are used for each axis. For the x-axis, the worktable is under control during tests with its position feedback from its linear encoder. Pitch motions of the worktable will cause a linear

displacement registered at the encoder head, which will be corrected by the controller. Therefore, the location of the encoder head is considered to be the pivot point in correcting for Abbe errors concerning the pitching motion of the x-axis. The y-axis pitch motion rotates under a different assumption. It is assumed that small pitch motions of the gantry beam do not induce noticeable pitch motions of the table. Therefore, the pitch axis of rotation for the y-axis remains on the granite surface. The vertical straightness of the y-axis is seen in Figure 5-14 which shows a high point located at the center of granite surface. It is assumed that the high point is the location of the pitch axis of rotation. The lever arm is calculated as the length from the metrology optics to the high point of the granite. Yaw motion of the table acts differently for the x- and y-axes due to the asymmetric design of the gantry. For x-axis measurements, the yaw axis is assumed to be vertical about the center of the worktable. However, for the y-axis, it is assumed to be centered about the four preloaded air bearings around the granite guideway.

Straightness errors are affected by roll motion. However, roll errors were not measured and therefore not accounted in the data presented in this chapter.

5.4 Linear Positional Error

This section presents the linear positional error of the x and y axes as described in ISO-230-2 [27]. The data presented has been compensated for Abbe error.

5.4.1 X Linear Positioning Error (EXX)

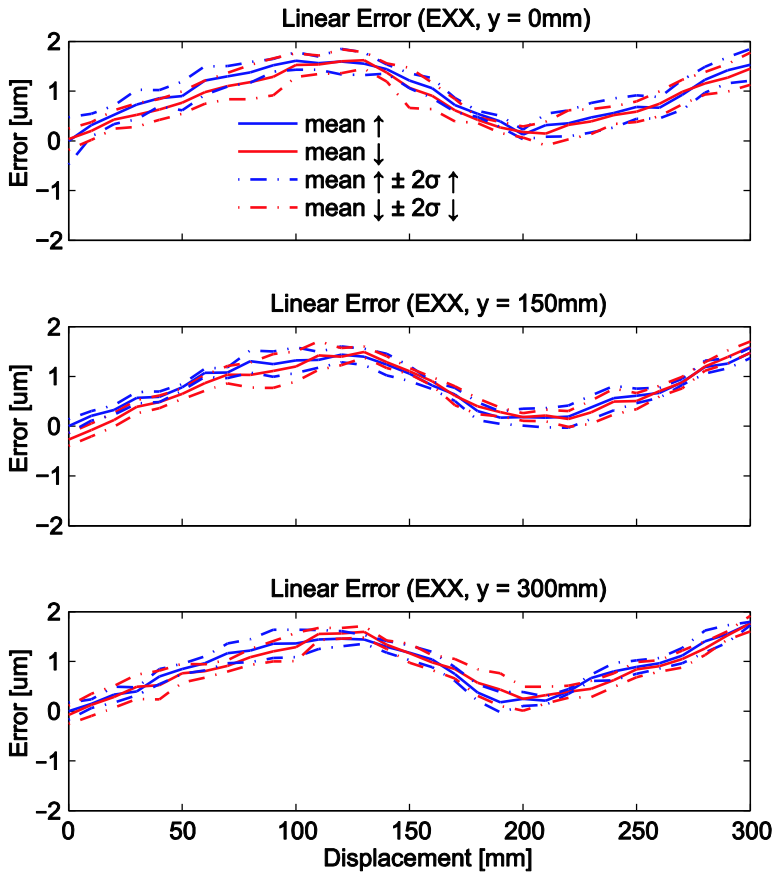

Figure 5-4. Linear positioning error of the X axis

Figure 5-4 clearly shows the similarity of the linear error profile between different measurement locations. The profile is created from errors within the encoder scale as well as other unforeseen effects. The accuracy of the encoder scales was measured by the manufacturer to be 0.79 µm. A best fit line would reveal a slight slope, which could be due to thermal expansion of the scale. This would cause the error to grow as x approaches 300 mm. The magnitude is quite repeatable with a maximum bidirectional uncertainty of 0.949 µm when y = 0 mm. Compensation of the linear error would remove the mean error profile and not the uncertainties. Unidirectional error compensation would decrease the linear accuracy to the uncertainty value at each measurement location, which has a maximum of ± 0.475 µm. A summary of the measurements is listed in Table 5-1.

Table 5-1. Metrology results for the X linear positioning error (w.r.t. table top)

Y = 0mm	Unidirectional ↑ [μm]	Unidirectional ↓ [μm]	Bidirectional [μm]
Reversal value (B)	N/A	N/A	0.234 (x = 60)
Mean reversal value ($\bar{B}$)	N/A	N/A	0.093
Range mean bidirectional positional deviation (M)	N/A	N/A	1.579
Systematic positional deviation (E)	1.608	1.585	1.620
Repeatability of positioning (R)	0.949 (x = 0)	0.812 (x = 150)	0.949
Accuracy (A)	2.327	2.018	2.327

Y = 150mm	Unidirectional ↑ [μm]	Unidirectional ↓ [μm]	Bidirectional [μm]
Reversal value (B)	N/A	N/A	0.284 (x = 10)
Mean reversal value ($\bar{B}$)	N/A	N/A	0.046
Range mean bidirectional positional deviation (M)	N/A	N/A	1.666
Systematic positional deviation (E)	1.472	1.859	1.859
Repeatability of positioning (R)	0.514 (x = 100)	0.682 (x = 90)	0.750
Accuracy (A)	1.737	2.105	2.105

Y = 300mm	Unidirectional ↑ [μm]	Unidirectional ↓ [μm]	Bidirectional [μm]
Reversal value (B)	N/A	N/A	0.253 (x = 70)
Mean reversal value ($\bar{B}$)	N/A	N/A	0.026
Range mean bidirectional positional deviation (M)	N/A	N/A	1.800
Systematic positional deviation (E)	1.763	1.837	1.837
Repeatability of positioning (R)	0.564 (x = 90)	0.658 (x = 190)	0.785
Accuracy (A)	1.970	2.178	2.178

Figure 5-5 illustrates the error profiles in a 3-dimensional view with the error located at its respected location within the machine's work area.

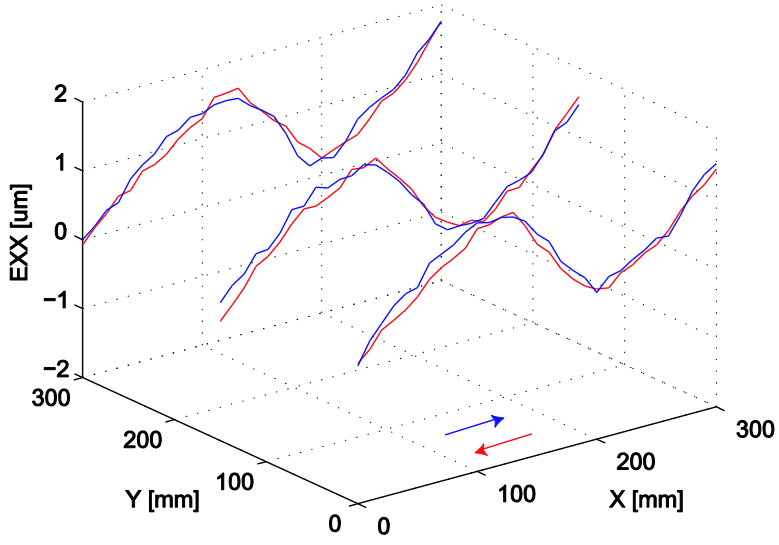

Figure 5-5. Grid view of X axis linear positioning error

5.4.2 Y Linear Positioning Error (EYY)

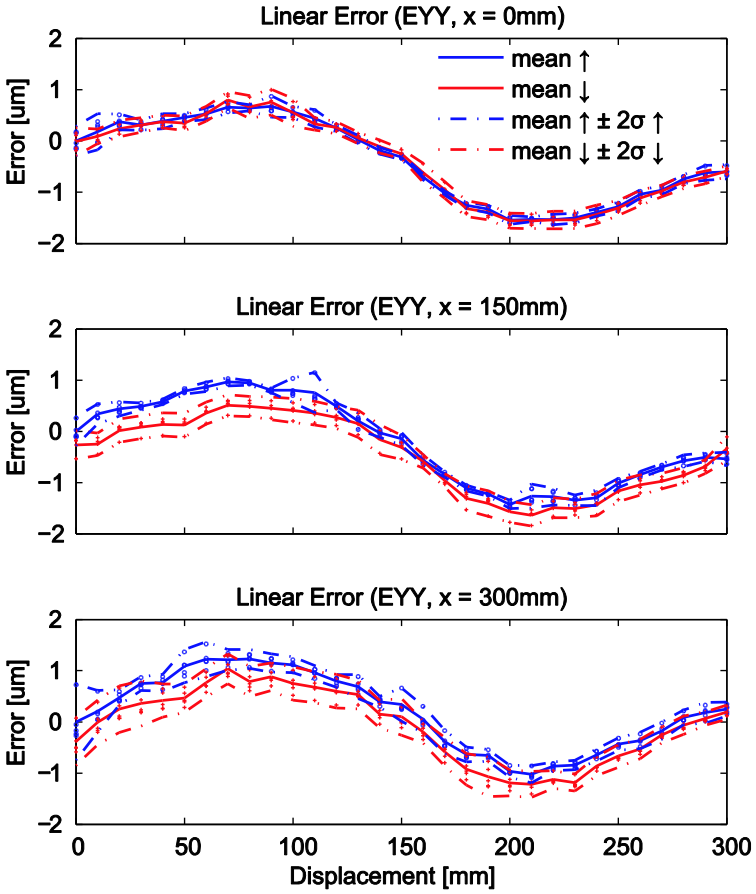

Figure 5-6. Linear positioning error of the Y axis

The profiles for each measurement in Figure 5-6 are similar. The profile shape is most likely due to the error within the encoder scale itself. The maximum unidirectional accuracy is 3.04 μm, which is mainly due to systematic deviation of the measurement. The maximum systematic positional deviation is 2.61 μm, which can be removed through error compensation. However, with a maximum uncertainty of 1.59 μm, error compensation methods will only provide a 2 times improvement. Table 5-2 summarizes the error data for each measurement location. It is expected that unidirectional error compensation will reduce the linear positioning error to ±0.743 μm.

Table 5-2. Metrology results for the Y linear positioning error (w.r.t. granite surface)

X = 0mm	Unidirectional ↑ [µm]	Unidirectional ↓ [µm]	Bidirectional [µm]
Reversal value (B)	N/A	N/A	0.147 (y = 70)
Mean reversal value ($\bar{B}$)	N/A	N/A	0.012
Range mean bidirectional positional deviation (M)	N/A	N/A	2.280
Systematic positional deviation (E)	2.217	2.366	2.366
Repeatability of positioning (R)	0.703 (y = 10)	0.545 (y = 100)	0.703
Accuracy (A)	2.516	2.726	2.726

X = 150mm	Unidirectional ↑ [µm]	Unidirectional ↓ [µm]	Bidirectional [µm]
Reversal value (B)	N/A	N/A	0.662 (y = 70)
Mean reversal value ($\bar{B}$)	N/A	N/A	0.271
Range mean bidirectional positional deviation (M)	N/A	N/A	2.235
Systematic positional deviation (E)	2.393	2.148	2.608
Repeatability of positioning (R)	0.782 (y = 110)	0.581 (y = 140)	1.025
Accuracy (A)	2.655	2.563	2.995

X = 300mm	Unidirectional ↑ [µm]	Unidirectional ↓ [µm]	Bidirectional [µm]
Reversal value (B)	N/A	N/A	0.624 (y = 50)
Mean reversal value ($\bar{B}$)	N/A	N/A	0.265
Range mean bidirectional positional deviation (M)	N/A	N/A	2.246
Systematic positional deviation (E)	2.251	2.258	2.448
Repeatability of positioning (R)	1.486 (y = 0)	0.940 (y = 0)	1.593
Accuracy (A)	2.756	2.805	3.040

Figure 5-7 illustrates the error profiles in a 3-dimensional view with the error located at its respected location within the machine's work area.

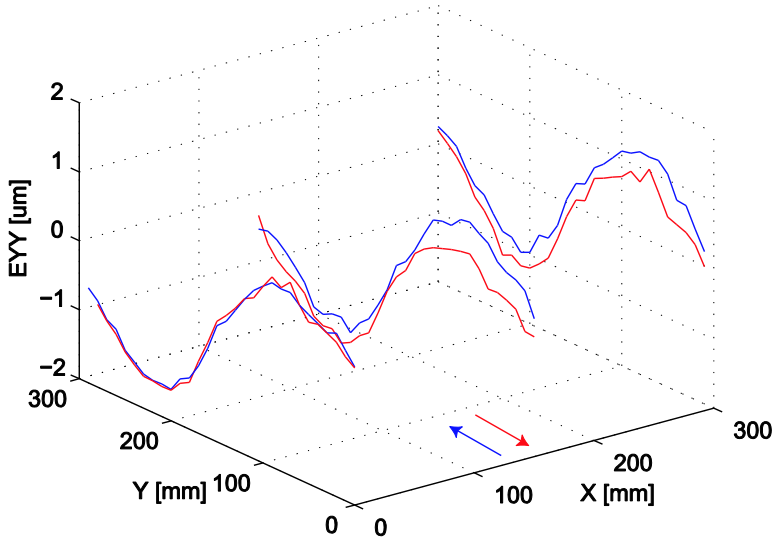

Figure 5-7. Grid view of Y axis linear positioning error

5.5 Straightness Error (EYX, EZX, EXY, EZY)

This section presents the vertical and horizontal straightness error of the x and y axes. The data is presented in accordance with ASME B5.54-2005 [25]. A least squares method is used to fit the data to the reference straight line. The data is presented by determining the mean bidirectional maximum and minimum and their corresponding uncertainties. It is displayed in this manner because the profile is not usually of concern and rather the overall accuracy is the desired value. However, the profile is required for compensation.

5.5.1 X Horizontal Straightness Error (EYX)

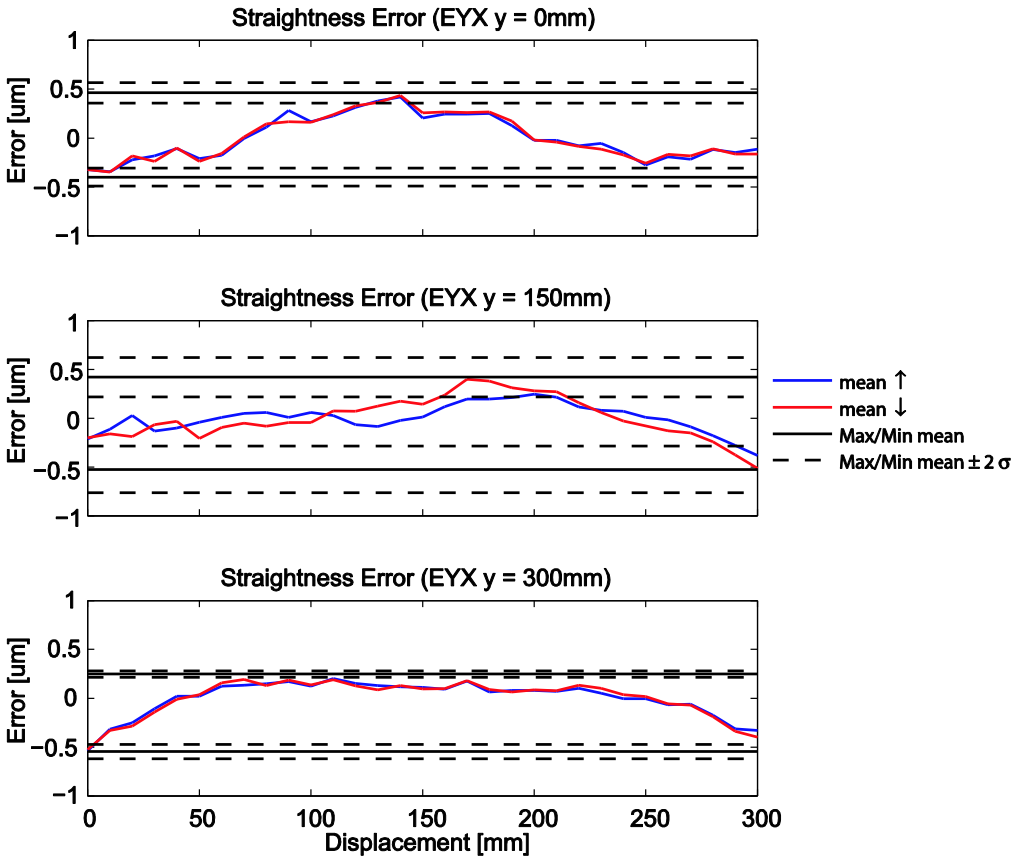

Figure 5-8. Horizontal straightness error of the X axis

The horizontal straightness is a direct correspondence to the gantry beam straightness. The profiles are somewhat similar as the high points are located in the center of travel, but their overall shapes do not correlate too closely. There are a couple factors which may contribute to the profile differences, such as roll of the table (rotation about the x-axis) along its travel. This would be categorized as Abbe error which cannot be adjusted, since roll was not measured. As well, it may be due to the large y-axis pitch error. Different lateral loads may be applied on the table as it is located

along the y-axis. The maximum systematic deviation is 0.94 µm with uncertainties of approximately 0.48 µm. The mean profiles for each measurement are used for error compensation, which should improve the straightness error from 1.39 µm, to ±0.24 µm. Table 5-3 summarizes the error data for each measurement location.

Table 5-3. Metrology results for the X horizontal straightness error

Y = 0mm		Bidirectional [µm]
	Systematic positional deviation (E)	0.864
	Repeatability of maximum (R_{max})	0.208
	Repeatability of minimum (R_{min})	0.184
	Accuracy (A)	1.060

Y = 150mm		Bidirectional [µm]
	Systematic positional deviation (E)	0.943
	Repeatability of maximum (R_{max})	0.403
	Repeatability of minimum (R_{min})	0.481
	Accuracy (A)	1.385

Y = 300mm		Bidirectional [µm]
	Systematic positional deviation (E)	0.794
	Repeatability of maximum (R_{max})	0.065
	Repeatability of minimum (R_{min})	0.148
	Accuracy (A)	0.900

Figure 5-9 illustrates the error profiles in a 3-dimensional view with the error located at its respected location within the machine's work area.

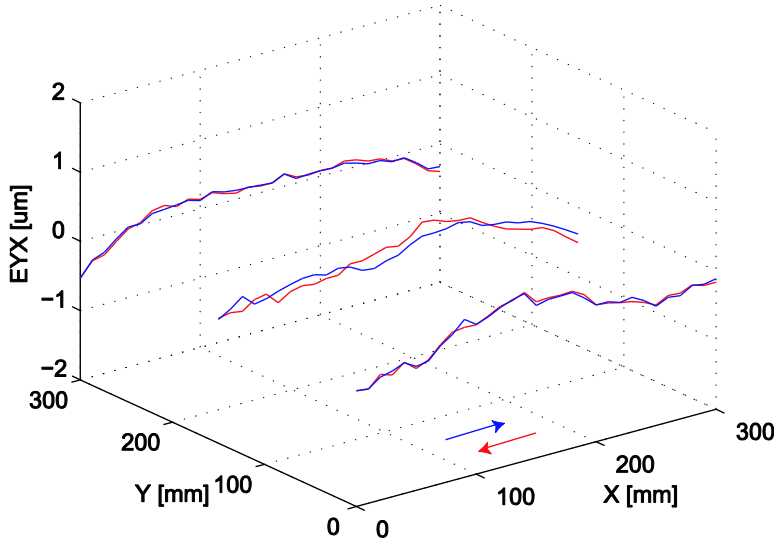

Figure 5-9. Grid view of X axis horizontal straightness error

5.5.2 X Vertical Straightness Error (EZX)

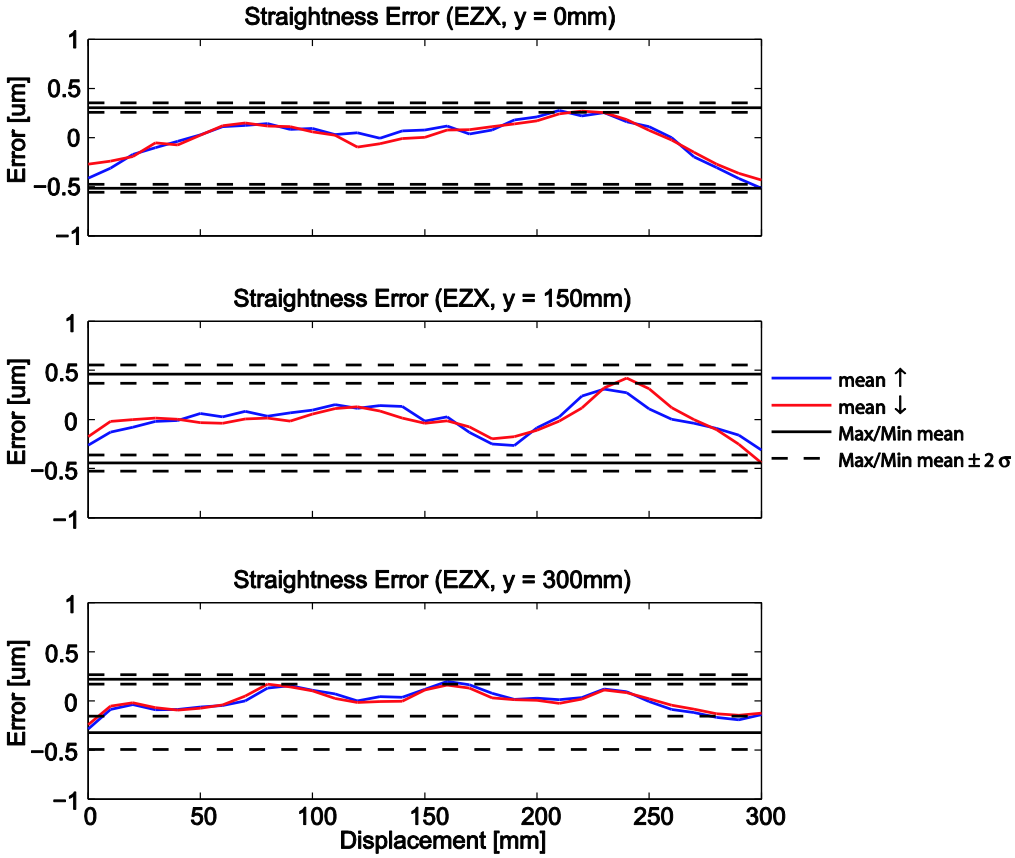

Figure 5-10. Vertical straightness error of the X axis

The vertical straightness of the x-axis is strongly influenced by the flatness profile of the granite surface. The reason for different profiles in Figure 5-10 is that the table is travelling along different sections of the granite, which have different flatness profiles. The maximum systematic deviation is 0.905 µm along the center of the granite surface. The maximum uncertainty is seen when y = 300 mm and corresponds to the uncertainty of the minimum mean. Overall, error compensation should be able to reduce the maximum accuracy from 1.08 µm, to ±0.17 µm. However, this will not be possible until a vertical axis is installed over top of the stage. Table 5-4 summarizes the error data for each measurement location.

Table 5-4. Metrology results of the X vertical straightness error

Y = 0mm		Bidirectional [μm]
	Systematic positional deviation (E)	0.822
	Repeatability of maximum (R_{max})	0.096
	Repeatability of minimum (R_{min})	0.081
	Accuracy (A)	0.911

Y = 150mm		Bidirectional [μm]
	Systematic positional deviation (E)	0.905
	Repeatability of maximum (R_{max})	0.185
	Repeatability of minimum (R_{min})	0.162
	Accuracy (A)	1.079

Y = 300mm		Bidirectional [μm]
	Systematic positional deviation (E)	0.544
	Repeatability of maximum (R_{max})	0.097
	Repeatability of minimum (R_{min})	0.342
	Accuracy (A)	0.763

Figure 5-11 illustrates the error profiles in a 3-dimensional view with the error located at its respected location within the machine's work area.

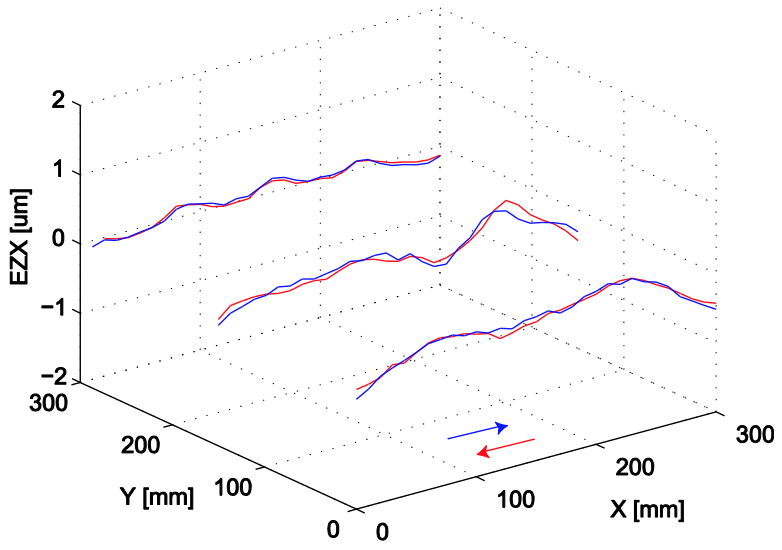

Figure 5-11. Grid view of X axis vertical straightness error

5.5.3 Y Horizontal Straightness Error (EXY)

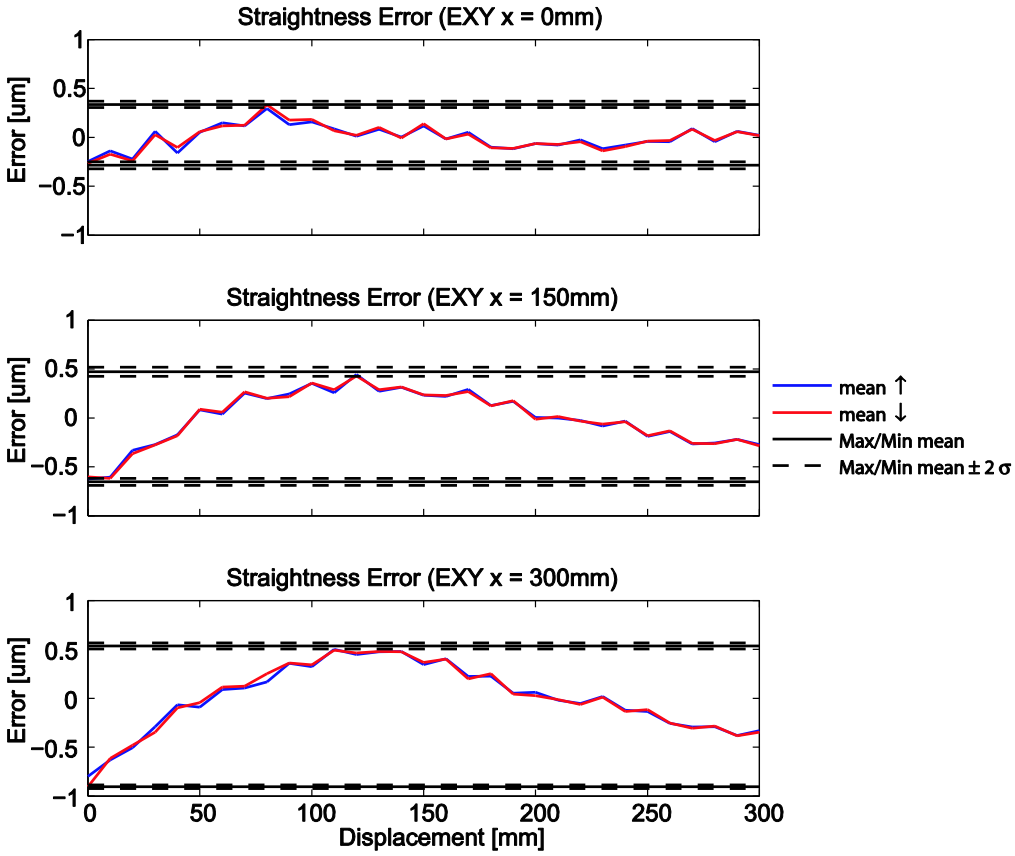

Figure 5-12. Horizontal straightness error of the Y axis

The horizontal straightness error corresponds to the straightness of the granite guideway. The profiles of y = 150 mm and y = 300 mm are similar, but both differ from the first. This may be due to roll of the table (rotation about the y-axis) as the table travels. As explained earlier, this is Abbe error which is not removed from the data, since roll was not measured. The maximum uncertainty of the data is 0.091 µm, with a maximum systematic deviation of 1.44 µm. Since the uncertainty is low, error compensation is more effective as it will reduce the error substantially, to ±0.045 µm. Table 5-5 summarizes the error at each measurement location.

Table 5-5. Metrology results for Y axis horizontal straightness

X = 0mm		Bidirectional [μm]
	Systematic positional deviation (E)	0.622
	Repeatability of maximum (R_{max})	0.065
	Repeatability of minimum (R_{min})	0.069
	Accuracy (A)	0.689

X = 150mm		Bidirectional [μm]
	Systematic positional deviation (E)	1.125
	Repeatability of maximum (R_{max})	0.091
	Repeatability of minimum (R_{min})	0.070
	Accuracy (A)	1.205

X = 300mm		Bidirectional [μm]
	Systematic positional deviation (E)	1.438
	Repeatability of maximum (R_{max})	0.061
	Repeatability of minimum (R_{min})	0.037
	Accuracy (A)	1.487

Figure 5-13 illustrates the error profiles in a 3-dimensional view with the error located at its respected location within the machine's work area.

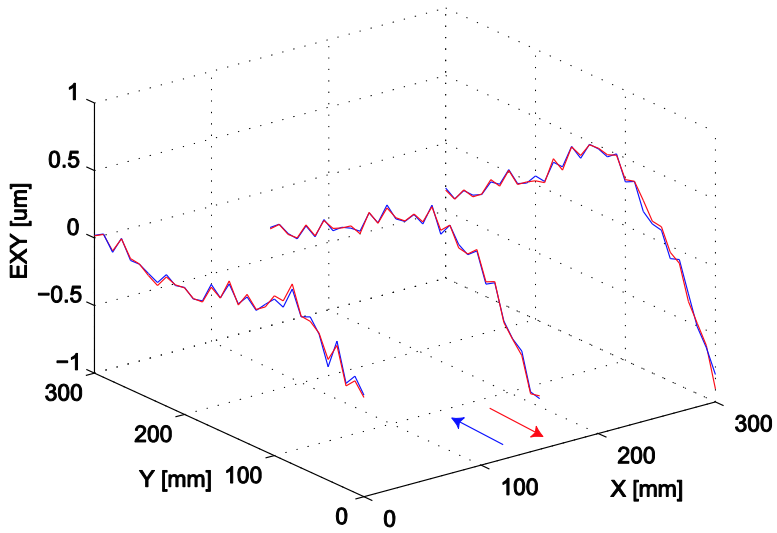

Figure 5-13. Grid view of Y axis horizontal straightness error

5.5.4 Y Vertical Straightness Error (EZY)

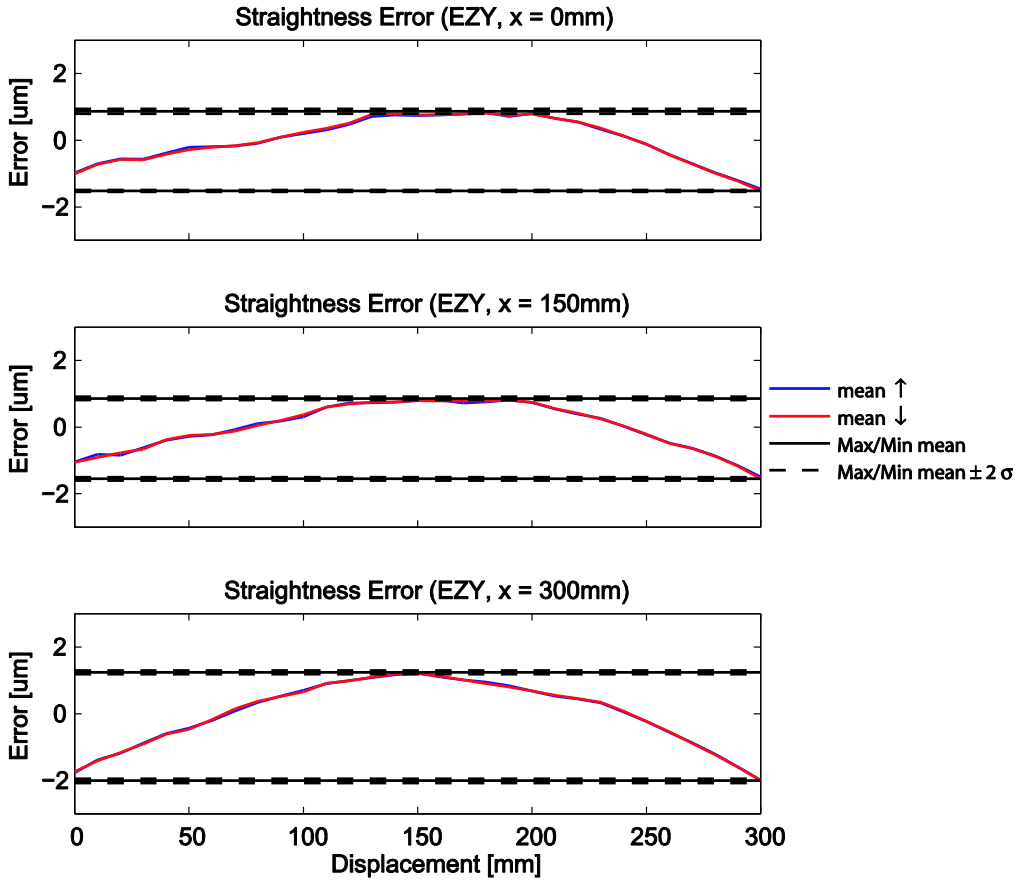

Figure 5-14. Vertical straightness error of the Y axis

The largest amount of linear error of the machine is the vertical straightness of the y-axis, displayed in Figure 5-14. The error is related to the flatness of the granite surface. Even though the errors may be large, the uncertainties are low, which allows for large improvements by error compensation. The maximum uncertainty is 0.149 µm, which occurs at the maximum mean when x = 0 mm. The maximum systematic deviation is 3.253 µm when x = 300 mm. Error compensation is expected to improve the accuracy from 3.37 µm, to ±0.075 µm.

Some Abbe error is present is the data shown in Figure 5-14 for the measurements located at x = 0, 300. Since the optics were located at the edge of the worktable, roll will contribute to a vertical displacement. Roll measurements must be completed prior to implementing the compensation algorithms.

Table 5-6. Metrology results for Y axis vertical straightness

X = 0mm		Bidirectional [μm]
	Systematic positional deviation (E)	2.387
	Repeatability of maximum (R_{max})	0.149
	Repeatability of minimum (R_{min})	0.053
	Accuracy (A)	2.488

X = 150mm		Bidirectional [μm]
	Systematic positional deviation (E)	2.409
	Repeatability of maximum (R_{max})	0.107
	Repeatability of minimum (R_{min})	0.095
	Accuracy (A)	2.510

X = 300mm		Bidirectional [μm]
	Systematic positional deviation (E)	3.253
	Repeatability of maximum (R_{max})	0.109
	Repeatability of minimum (R_{min})	0.128
	Accuracy (A)	3.371

Figure 5-15 illustrates the error profiles in a 3-dimensional view with the error located at its respected location within the machine's work area.

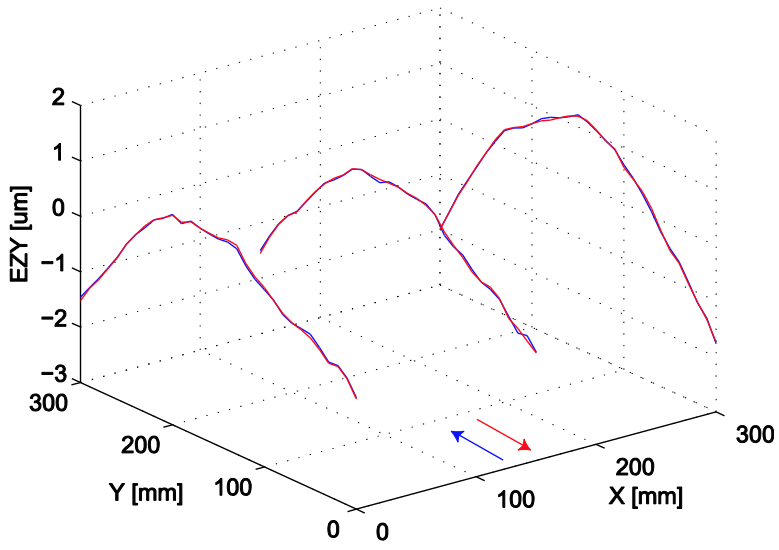

Figure 5-15. Grid view of Y axis vertical straightness error

5.6 Angular Error (EBX, ECX, EAY, ECY)

This section presents the angular errors of the x and y axes. The data is presented in the same manner as ISO-230-2 [39]. Abbe error is not present in angular measurements, as the rotation of an object is identical at any measurement location.

5.6.1 X Pitch Error (EBX)

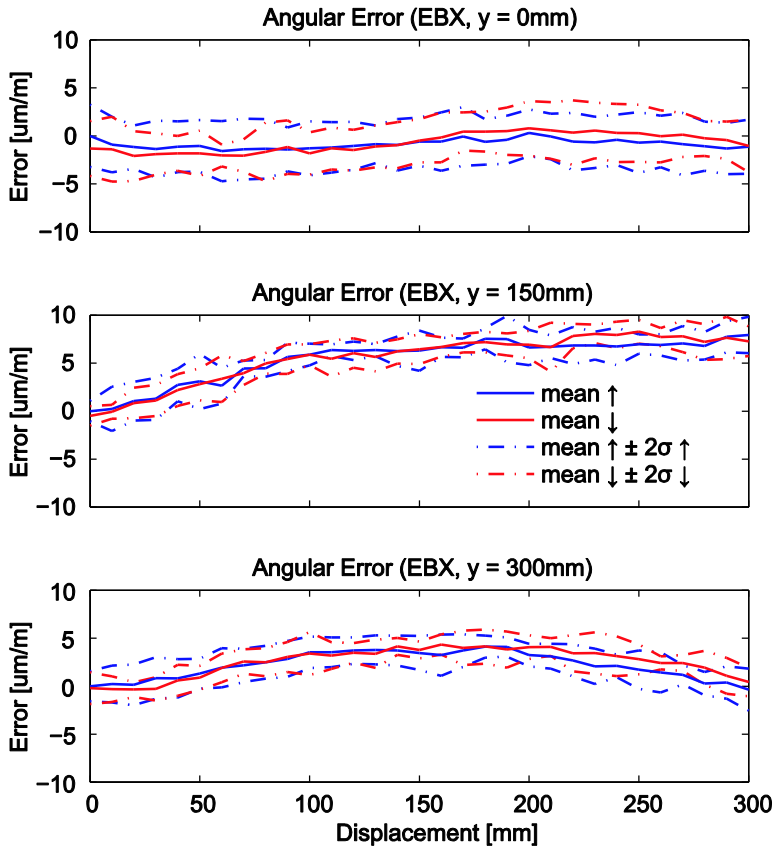

Figure 5-16. Pitch error of the X axis

Figure 5-16 displays the pitch error of the x-axis at each measurement location. Pitch error is the resultant of the curvature of the guideways, which in this case is the curvature of the top granite surface. The data presented is the relative angular, error since the initial absolute angular error is unknown. The maximum bidirectional systematic deviation occurs when y = 150 mm, which is 8.77 µm/m with an uncertainty of 5 µm/m for a total accuracy of 12.0 µm/m. Compensation of angular errors requires two orthogonal rotation axes, which in this case will be present when the trunnion is installed. It is expected to reduce the angular error from 12.0 µm/m to ±3.71 µm/m.

Table 5-7. Metrology results for the X pitch error

Y = 0mm	Unidirectional ↑ [μm/m]	Unidirectional ↓ [μm/m]	Bidirectional [μm/m]
Reversal value (B)	N/A	N/A	1.32 (x = 0)
Mean reversal value ($\bar{B}$)	N/A	N/A	-0.126
Range mean bidirectional positional deviation (M)	N/A	N/A	2.37
Systematic positional deviation (E)	1.91	2.88	2.88
Repeatability of positioning (R)	6.50 (x = 270)	6.76 (x = 10)	7.42
Accuracy (A)	7.80	8.46	8.46

Y = 150mm	Unidirectional ↑ [μm/m]	Unidirectional ↓ [μm/m]	Bidirectional [μm/m]
Reversal value (B)	N/A	N/A	1.28 (x = 250)
Mean reversal value ($\bar{B}$)	N/A	N/A	-0.081
Range mean bidirectional positional deviation (M)	N/A	N/A	7.93
Systematic positional deviation (E)	7.93	8.77	8.77
Repeatability of positioning (R)	5.74 (x = 50)	5.11 (x = 210)	5.00
Accuracy (A)	12.0	11.3	12.0

Y = 300mm	Unidirectional ↑ [μm/m]	Unidirectional ↓ [μm/m]	Bidirectional [μm/m]
Reversal value (B)	N/A	N/A	1.66 (x = 280)
Mean reversal value ($\bar{B}$)	N/A	N/A	-0.314
Range mean bidirectional positional deviation (M)	N/A	N/A	4.23
Systematic positional deviation (E)	4.47	4.70	4.70
Repeatability of positioning (R)	4.40 (x = 300)	4.49 (x = 100)	5.39
Accuracy (A)	7.95	7.78	8.47

Figure 5-17 illustrates the error profiles in a 3-dimensional view with the error located at its respected location within the machine's work area.

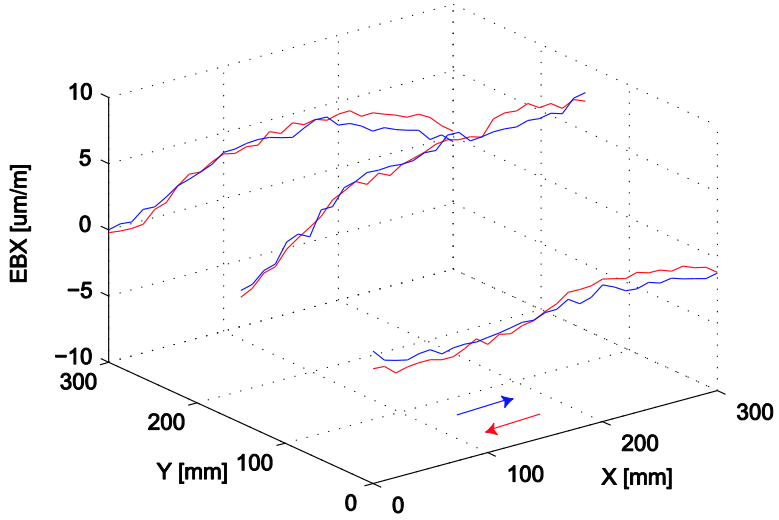

Figure 5-17. Grid view of X axis pitch error

5.6.2 X Yaw Error (ECX)

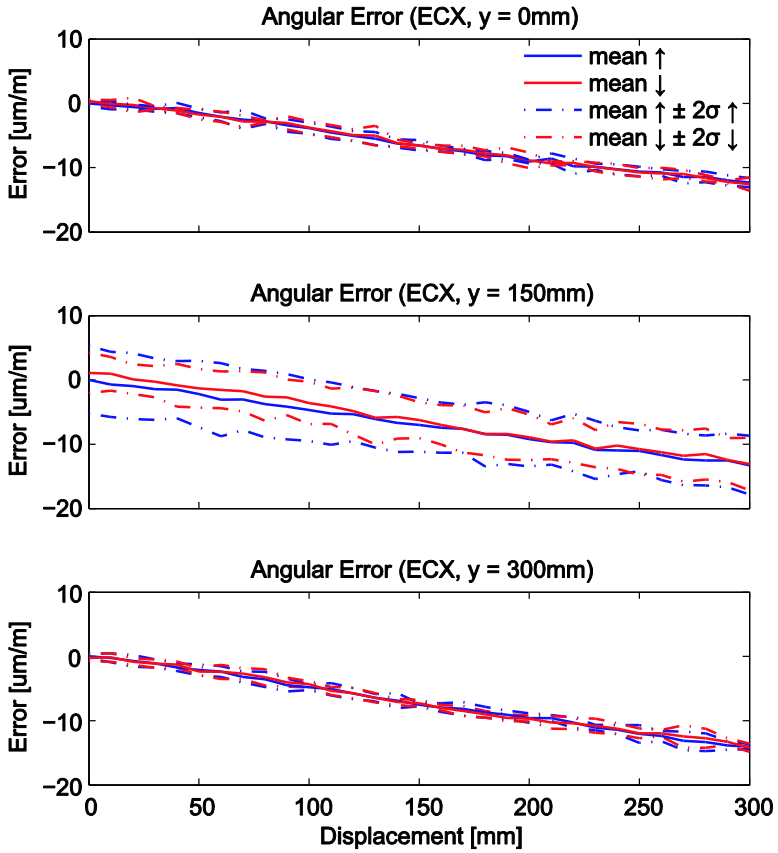

Figure 5-18. Yaw error of the X axis

Figure 5-18 displays the yaw error of the x-axis. This error is mainly created by the curvature of the gantry beam. The data collected at y = 150 has significantly larger uncertainty, however the mean value is similar to the other locations. Occasionally, laser misalignment will result in additional pulses within the electronics of the metrology equipment. This can lead to the data drifting during measurements, leading to larger uncertainties. This is assumed to have occurred while measuring the x-axis yaw error at y = 150 mm. The uncertainty levels for this test will not be considered for the predicted improvement with geometric compensation. The maximum bidirectional systematic deviation is 14.4 µm/m, while the maximum bidirectional uncertainty is 3.83 µm/m. Therefore, it can be assumed that error compensation will remove the systematic deviation and reduce the accuracy from 15.3 µm/m to ±1.92 µm/m.

Table 5-8. Metrology results for the X yaw error

Y = 0mm	Unidirectional ↑ [μm/m]	Unidirectional ↓ [μm/m]	Bidirectional [μm/m]
Reversal value (B)	N/A	N/A	0.784 (x = 210)
Mean reversal value ($\bar{B}$)	N/A	N/A	-0.046
Range mean bidirectional positional deviation (M)	N/A	N/A	12.6
Systematic positional deviation (E)	12.3	12.9	12.9
Repeatability of positioning (R)	2.85 (x = 70)	3.04 (x = 130)	2.99
Accuracy (A)	13.5	14.4	14.4

Y = 150mm	Unidirectional ↑ [μm/m]	Unidirectional ↓ [μm/m]	Bidirectional [μm/m]
Reversal value (B)	N/A	N/A	1.65 (x = 10)
Mean reversal value ($\bar{B}$)	N/A	N/A	-0.689
Range mean bidirectional positional deviation (M)	N/A	N/A	13.7
Systematic positional deviation (E)	13.3	14.2	14.4
Repeatability of positioning (R)	11.3 (x = 60)	8.36 (x = 130)	10.1
Accuracy (A)	23.1	21.4	23.1

Y = 300mm	Unidirectional ↑ [μm/m]	Unidirectional ↓ [μm/m]	Bidirectional [μm/m]
Reversal value (B)	N/A	N/A	0.675 (x = 210)
Mean reversal value ($\bar{B}$)	N/A	N/A	-0.066
Range mean bidirectional positional deviation (M)	N/A	N/A	14.0
Systematic positional deviation (E)	14.0	14.0	14.2
Repeatability of positioning (R)	2.89 (x = 270)	3.45 (x = 270)	3.83
Accuracy (A)	15.2	15.3	15.3

Figure 5-19 illustrates the error profiles in a 3-dimensional view with the error located at its respected location within the machine's work area.

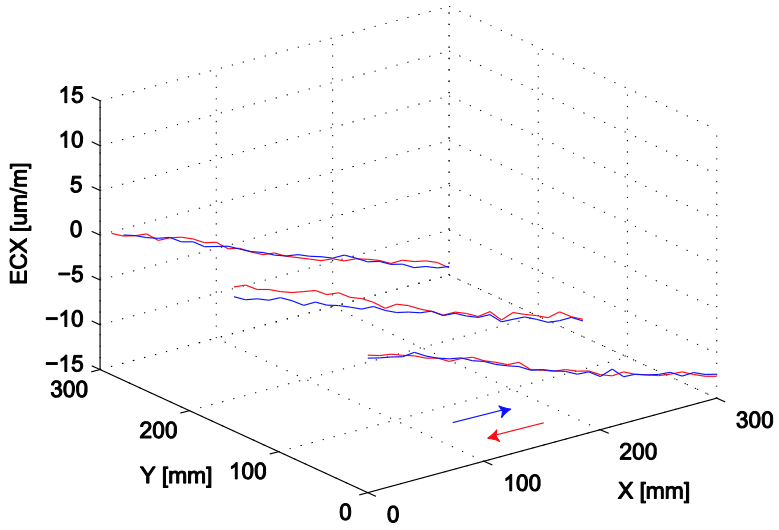

Figure 5-19. Grid view of X yaw error

5.6.3 Y Pitch Error (EAY)

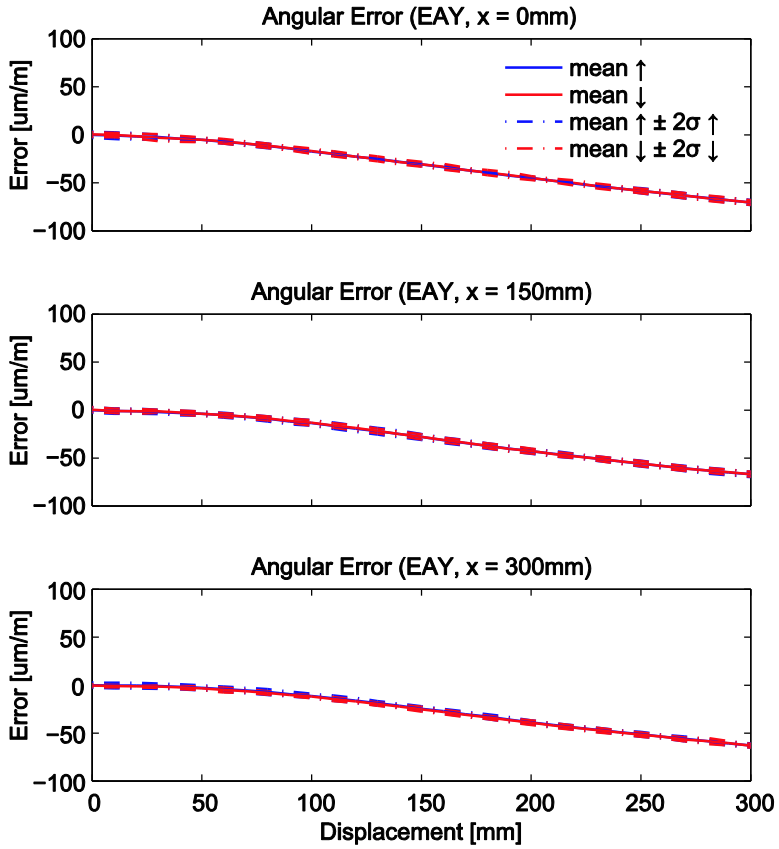

Figure 5-20. Pitch error of the Y axis

The y-axis pitch error is the largest angular error of the machine. With a maximum bidirectional systematic deviation of 70.9 µm/m, it is significantly higher than the other angular errors. The uncertainty, however, is of the same order as the other angular errors with a maximum bidirectional uncertainty of 6.83 µm/m. This error is due to the curvature of the granite surface, which can be seen in Figure 5-14. The accuracy of the pitch error is expected to improve from 76.5 µm/m to ±3.92 µm/m, after compensation.

Table 5-9. Metrology results for the Y pitch error

X = 0mm	Unidirectional ↑ [μm/m]	Unidirectional ↓ [μm/m]	Bidirectional [μm/m]
Reversal value (B)	N/A	N/A	0.524 (y = 10)
Mean reversal value ($\bar{B}$)	N/A	N/A	-0.113
Range mean bidirectional positional deviation (M)	N/A	N/A	70.7
Systematic positional deviation (E)	70.5	70.8	70.9
Repeatability of positioning (R)	6.96 (y = 10)	7.30 (y = 30)	6.83
Accuracy (A)	76.5	75.7	76.5

X = 150mm	Unidirectional ↑ [μm/m]	Unidirectional ↓ [μm/m]	Bidirectional [μm/m]
Reversal value (B)	N/A	N/A	0.662 (y = 30)
Mean reversal value ($\bar{B}$)	N/A	N/A	-0.185
Range mean bidirectional positional deviation (M)	N/A	N/A	67.1
Systematic positional deviation (E)	67.0	67.3	67.5
Repeatability of positioning (R)	7.30 (y = 140)	5.91 (y = 190)	6.57
Accuracy (A)	72.9	72.4	72.9

X = 300mm	Unidirectional ↑ [μm/m]	Unidirectional ↓ [μm/m]	Bidirectional [μm/m]
Reversal value (B)	N/A	N/A	0.971 (y = 60)
Mean reversal value ($\bar{B}$)	N/A	N/A	0.551
Range mean bidirectional positional deviation (M)	N/A	N/A	62.8
Systematic positional deviation (E)	63.0	62.6	63.1
Repeatability of positioning (R)	6.08 (y = 80)	5.93 (y = 280)	6.25
Accuracy (A)	68.0	65.9	68.0

Figure 5-21 illustrates the error profiles in a 3-dimensional view with the error located at its respected location within the machine's work area.

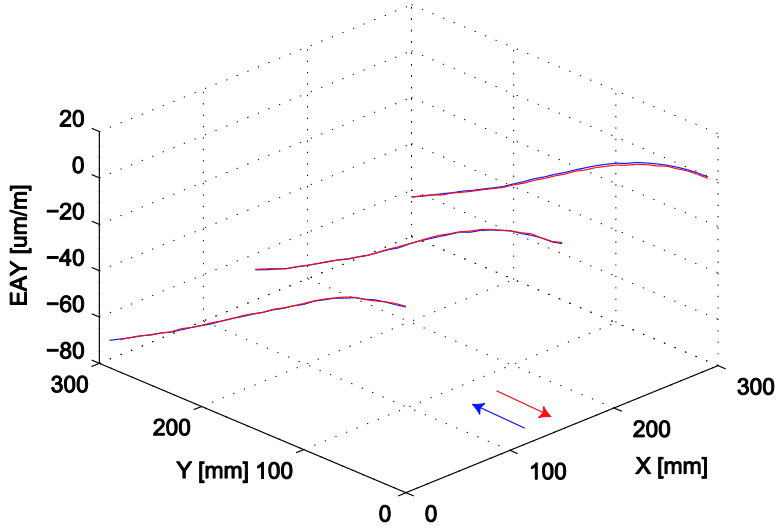

Figure 5-21. Grid view of Y pitch error

5.6.4 Y Yaw Error (ECY)

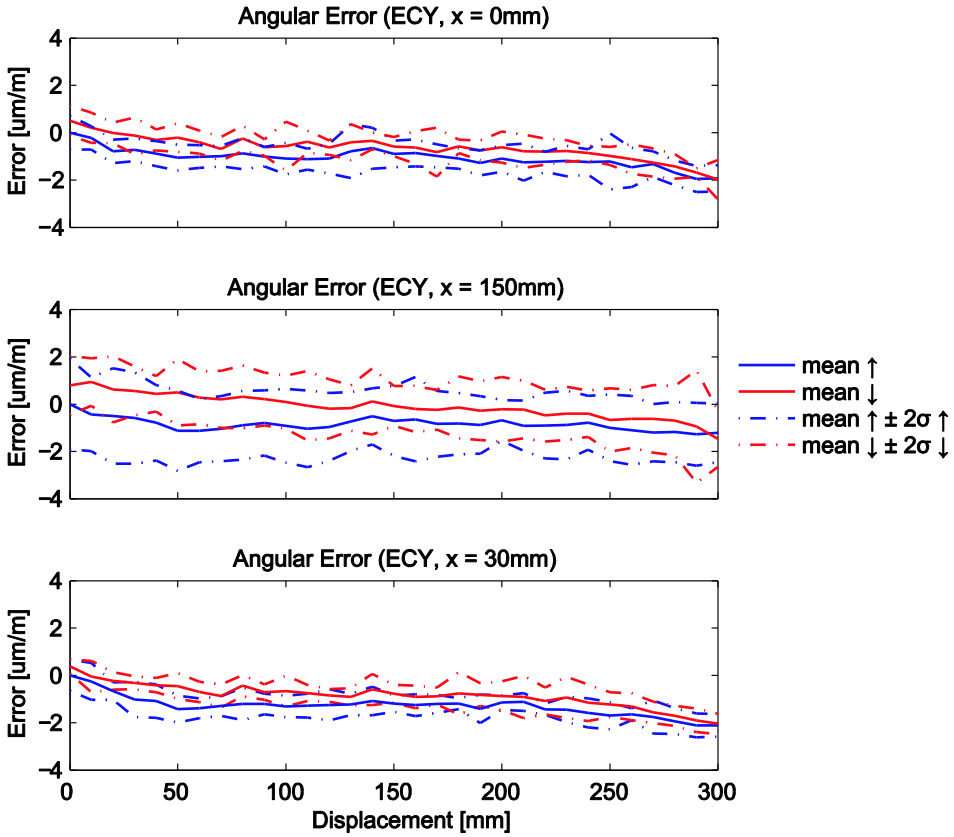

Figure 5-22. Yaw error of the Y axis

The yaw error of the y axis is the smallest angular error of the machine. This error is from the curvature of the granite guideway. This error is smaller than the other angular errors, due to the four preloaded air bearings of the gantry spanning a large distance. Since their separation is large, the angular error is small. The maximum bidirectional systematic deviation is 2.49 μm/m with a maximum uncertainty of 4.73 μm/m. The y-axis yaw error cannot be improved by a very significant amount since its uncertainty is larger than the mean deviation. The expected accuracy improvement after error compensation is from 5.35 μm/m to ±2.37 μm/m.

Table 5-10. Metrology results for the Y yaw error

X = 0mm	Unidirectional ↑ [μm/m]	Unidirectional ↓ [μm/m]	Bidirectional [μm/m]
Reversal value (B)	N/A	N/A	0.850 (y = 50)
Mean reversal value ($\bar{B}$)	N/A	N/A	-0.424
Range mean bidirectional positional deviation (M)	N/A	N/A	2.20
Systematic positional deviation (E)	1.95	2.48	2.48
Repeatability of positioning (R)	2.36 (y = 250)	2.06 (y = 100)	2.28
Accuracy (A)	3.21	3.94	3.94

X = 150mm	Unidirectional ↑ [μm/m]	Unidirectional ↓ [μm/m]	Bidirectional [μm/m]
Reversal value (B)	N/A	N/A	0.1.63 (y = 50)
Mean reversal value ($\bar{B}$)	N/A	N/A	-0.756
Range mean bidirectional positional deviation (M)	N/A	N/A	1.74
Systematic positional deviation (E)	1.27	2.41	2.41
Repeatability of positioning (R)	4.03 (y = 20)	4.75 (y = 290)	4.73
Accuracy (A)	4.74	5.35	5.35

X = 300mm	Unidirectional ↑ [μm/m]	Unidirectional ↓ [μm/m]	Bidirectional [μm/m]
Reversal value (B)	N/A	N/A	0.973 (y = 50)
Mean reversal value ($\bar{B}$)	N/A	N/A	-0.437
Range mean bidirectional positional deviation (M)	N/A	N/A	2.27
Systematic positional deviation (E)	2.12	2.43	2.49
Repeatability of positioning (R)	1.57 (y = 10)	1.79 (y = 180)	2.09
Accuracy (A)	3.28	3.14	3.29

Figure 5-23 illustrates the error profiles in a 3-dimensional view with the error located at its respected location within the machine's work area.

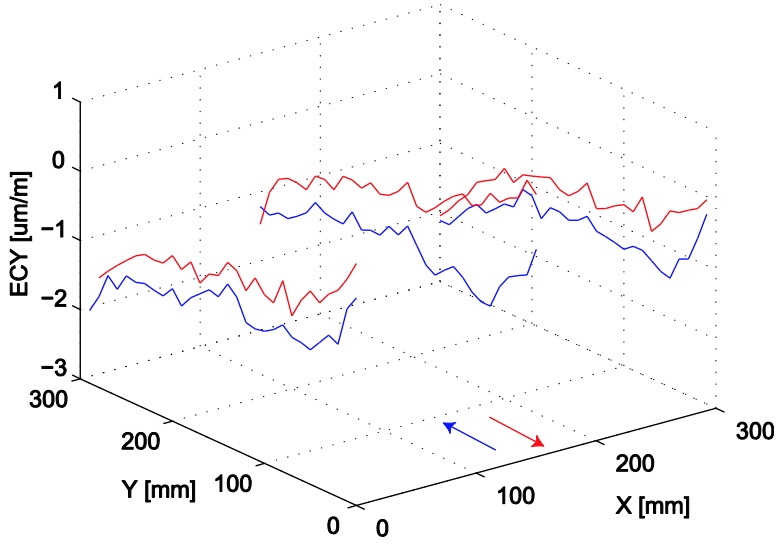

Figure 5-23. Grid view of Y yaw error

5.7 Conclusion

This chapter has presented the data and analysis of metrology measurements of the precision stage. Linear positioning error, vertical and horizontal straightness, as well as pitch and yaw errors were measured using a laser interferometer and presented in accordance with international metrology standards. Table 5-11 summarizes the maximum accuracies of all measurement locations for each test performed.

Table 5-11. Summary of accuracies from error measurements

		Error	Units
X-Axis			
	Linear Positioning	2.327	µm
	Horizontal Straightness	1.385	µm
	Vertical Straightness	1.079	µm
	Pitch	12.0	µm/m
	Yaw	23.1	µm/m
Y-Axis			
	Linear Positioning	3.040	µm
	Horizontal Straightness	1.487	µm
	Vertical Straightness	3.371	µm
	Pitch	76.5	µm/m
	Yaw	5.35	µm/m

Geometric error compensation will be used in future experiments to improve the accuracy of the machine. It is assumed that mean error values will be compensated, leaving the uncertainty as the remaining error. Table 5-12 lists the estimated errors with compensation applied.

Table 5-12. Summary of predicted accuracies assuming geometric error compensation

		Error	Units
X-Axis			
	Linear Positioning	0.475	µm
	Horizontal Straightness	0.241	µm
	Vertical Straightness	0.063	µm
	Pitch	2.87	µm/m
	Yaw	1.73	µm/m
Y-Axis			
	Linear Positioning	0.743	µm
	Horizontal Straightness	0.031	µm
	Vertical Straightness	0.064	µm
	Pitch	3.65	µm/m
	Yaw	2.38	µm/m

Chapter 6
Conclusions and Future Work

This thesis has presented the mechanical design, controller design and metrology of a novel ultra-precision planar stage intended as a base for a 5-axis machine tool. Its workspace of 300x300 mm^2 provides macro and micro operational capabilities for many applications.

The design of the machine incorporated a T-type gantry and worktable configuration with an asymmetric granite guideway to provide a majority of the machine's yaw and lateral stiffness. The gantry beam extends over the workspace to act as a guideway for the worktable. Rigid body yaw vibration of the gantry was observed at ~ 68 Hz due to its high moment of inertia around the y-axis guideway. A secondary motor for the gantry was installed at the end, to actively stiffen the structure and dampen the vibration mode. To further stiffen the structure, the gantry beam and worktable were decoupled from vertical loads, by installing a Vacuum Pre-Loaded (VPL) air bearing underneath the worktable to support its load on the granite surface. Hence, vertical deflections of the beam do not result in position deviations on the worktable surface. As well, the VPL provides higher vertical and pitch stiffness than aerostatic bearings, which was confirmed experimentally. Direct drive linear motors were implemented to actuate the stage up to 10 m/s^2 acceleration and 1 m/s velocity. Their non-contact and direct drive properties resulted in higher servo performance and positional accuracy than traditional mechanical systems, like ball-screw drives.

Liquid cooled motor couplings were designed to mitigate heat generated by the linear motors during high transient operations. Finite element analyses of the x- and y-axis coupling designs demonstrated their capabilities to maintain a constant 20°C temperature on the surface in contact with the stage. The control of the laboratory temperature revealed a ±1°C range, which was found to be too high. Further improvements to the thermostat controller are expected to lower the range to ±0.2°C.

Static stiffness testing of the stage revealed a discrepancy between theoretical and experimental stiffness values. It was determined that the pitch stiffness of the VPL, and its bolted interface, resulted in lower values when a lateral load was applied on the top surface of the worktable. Also, other bearings are still under point contact allowing for relative motion between the bearing and guideways. The resulting lateral stiffness values when loaded at the top of the worktable were 22.2 N/μm in the x-axis and 23.9 N/μm in the y-axis. These stiffness values are expected to improve after cementing the bearings.

Dynamic testing of the drive systems using Frequency Response Function (FRF) measurements revealed the vibration modes of the stage structure. The first mode present in the x-axis occurs at 220

Hz and is believed to be due to the pitching of the worktable. A prominent mode at ~68 Hz in the y-axis is due to the rigid body yaw vibration about the four preloaded air bearings for the gantry. A second mode in the y-axis occurs between 320 Hz and 364 Hz, and is considered to be due to the bending mode of the beam. This mode is dependent on the position of the x-axis. Model parameters were identified through least squares parameter estimation of the experimental FRF tests. A loop shaping controller was designed for the x-axis with a crossover frequency of 100 Hz and phase margin of 25°. The resulting maximum sensitivity of the loop function was 2.6 at approximately 100 Hz, which is slightly aggressive, but favors better tracking results. A multivariable control framework was implemented for the y-axis due to the strong coupling in the dual actuator design of the gantry. Signal averaging of the encoder measurements was used to determine the position of the center of mass of the stage. The averaging technique negated the 68 Hz mode, allowing for higher controller bandwidth designs and better tracking response. As well, active damping High (200 mm/s) and low (20 mm/s) speed tracking results were completed to test the controller designs. Peak errors of 1.61 µm and 1.45 µm for the x- and y-axes respectively, were measured for the low speed tracking. The high speed test measured peak errors of 2.74 µm and 2.41 µm for the x- and y-axes respectively.

Static errors of the machine were measured using laser interferometry for both axes. Linear positioning, straightness and angular errors were measured at 10 mm increments over the full range of motion. A final error budget, Table 6-1, includes updated values of geometric, dynamic, servo and thermal errors of the machine.

Suggestions for future work include improvement to the environmental temperature control of the laboratory. Application of cement around the bearings, especially the VPL, should further improve the stiffness of the structure and also the control bandwidth and accuracy. Some ideas learned through the course of research are as follows:

- Redesign machines base structure to avoid excitation of base vibrations, which reduce positioning accuracy.
- Lower the profile of the stage structure to improve pitch stiffness.
- Align actuators with center of mass to reduce moment loads during acceleration.
- Locate encoders closer to work area to minimize position feedback errors.
- Implement linear amplifiers to replace PWM amplifier.
- Investigate stiffness features of VPL to develop analytical model.
- Apply VPL technology to the gantry to increase its pitch stiffness

Table 6-1. Final Error Budget

	Error Magnitude (nm)					
	Without Compensation			With Compensation[1]		
	X	Y	Z	X	Y	Z
Linear	2327	3040	-	475	743	-
Straightness						
Horizontal	1487	1385	-	31	241	-
Vertical[2]	-	-	3371	-	-	64
Angular (included in Linear)	0	0	0	0	0	0
Dynamic (0.2 g acceleration)	2845	2960	0	427	444	0
Servo (@ 0.2 g acc., 50 m/s^3 jerk)	2740	2410	-	2740	2410	-
Thermal						
Friction	0	0	0	0	0	0
Drive System	0	0	0	0	0	0
Environment (20 ± 0.2°C)	1520	270	0	1520	270	0
Static Error						
Arithmetic Sum (E_A)	5334	4695	3371	2026	1254	64
RMS[3] Sum (E_R)	1820	1935	3371	920	477	64
Mean ((E_A + E_R)/2)	3577	3315	3371	1473	866	64
Maximum Resultant Error	**E_T = 5.93 µm**			**E_T = 1.71 µm**		
Static + Dynamic Error						
Arithmetic Sum (E_A)	10919	10065	3371	5193	4108	64
RMS[3] Sum (E_R)	2260	2272	3371	1430	1157	64
Mean ((E_A + E_R)/2)	6590	6168	3371	3312	2632	64
Maximum Resultant Error	**E_T = 9.64 µm**			**E_T = 4.23 µm**		

[1] Compensation indicates the correction of repeatable geometric & dynamic errors by shifting the position commands. 15% uncertainty in dynamic error compensation is assumed.
[2] Maximum of both axes.
[3] Assumes normal probability for each error about its mean value.

References

[1] Slocum, A. H., 1992, Precision Machine Design, Society of Manufacturing Engineers, Dearborn MI.

[2] Shinno, H., Yoshioka, H., Taniguchi, K., 2007, A Newly Developed Linear Motor-Driven Aerostatic X-Y Planar Motion Table System for Nano-Machining, Annals of the CIRP, 56/1:369-372

[3] Shinno, H., Hashizume, H., 1999, Nanometer Positioning of a Linear Motor-Driven Ultraprecision Aerostatic Table System with Electrorheological Fluid Dampers, Annals of the CIRP, 48/1:289-292

[4] Cheng, X., Nakamoto, K., Sugai, M., Matsumoto, S., Wang, Z.G., Yamazaki, K., 2008, Development of ultra-precision machining system with unique wire EDM tool fabrication system for micro/nano-machining, Annals of the CIRP, 57/1:415-420

[5] Holmes, M., Trumpet, D., Hocken, R., 1995, Atomic-Scale Precision Motion Control Stage (The Angstrom Stage), Annals of the CIRP, 44/1:455-460

[6] Aerotech Inc., 2010, ABL9000 Air Bearing Stage, Retrieved January 11, 2010, from the Aerotech web site, http://www.aerotech.com/products/airbearing/abl9000.html

[7] Precitech, Inc. 2010, Nanoform 700 Ultra, Retrieved January 11, 2010, from Precitech web site, http://www.precitech.com/Precitech_nano700_features.html

[8] Moore Tool Company, 2010, Drum Lathes – Machines for development and production of microstructured surfaces, Retrieved January 11, 2010, from Moore Tool website, http://www.mooretool.com/PDF%20Brochures/Drum%20Lathes.pdf

[9] ASML, 2010, Twinscan NXT:1950i: 193-nm Step-and-Scan, Retrieved from ASML web site, http://www.asml.com/asml/show.do?ctx=6720&rid=36951

[10] Schwenke, H., Knapp, W., Haitjema, H., Weckenmann, A., Schmitt, R., Delbressine, F., 2008, Geometric error measurement and compensation of machines – An Update, Annals of the CIRP, 57/2:660-675

[11] Kamalzadeh, A., 2008, Ph.D. Thesis: Precision Control of High Speed Ball Screw Drives. The University of Waterloo, Waterloo, Canada.

[12] Sriyotha, P., Nakamoto, K., Sugai, M., Yamazaki, K., 2006, Development of 5-Axis Linear Motor Driven Super-Precision Machine, Annals of the CIRP, 55/1:381-384

[13] ETEL S.A., 2010, Linear Motors Overview, Retrieved January 11, 2010, from ETEL web site, http://www.etel.ch/linear_motors

[14] Donmez, A., 1985, Ph.D. Thesis: A General Methodology for Machine Tool Accuracy Enhancement: Theory, Application and Implementation. Purdue University, West Lafayette, Indiana.

[15] Automation Creations Inc., 2010, Online Materials Information Resource, Retrieved, January 11, 2010, from website, http://www.matweb.com

[16] ETEL S.A., 2010, Torque Motors, Retrieved January 11, 2010, from ETEL web site, http://www.etel.ch/torque_motors

[17] Erkorkmaz, K., 2007, Course notes: Precision Control Theory, University of Waterloo, Waterloo, Canada.

[18] Tackeuchi, Y., Sakaida, Y., Sawada, K., Sata, T., 2000, Development of a 5-Axis Control Ultraprecision Milling Machine for Micromachining Based on Non-Friction Servomechanisms, Annals of CIRP, 49/1:295-298.

[19] New Way Air Bearings, 2010, Vacuum Preloaded Air Bearings, Retrieved January 2010, from website, http://www.newwayairbearings.com/Vacuum-Preloaded-Air-Bearings

[20] Shinno, H., Hashizume, H., Yoshioka, H., Komatsu, K., Shinshi, T., Sato, K., 2004, X-Y-Θ Nano-Positioning Table System for a Mother Machine, Annals of the CIRP, 53/1:337-340.

[21] Cortesi, R., 2000, M.Sc. Thesis: An Easy to Manufacture Non-Contact Precision Linear Motion System and its Applications. Massachusetts Institute of Technology, Boston, Massachusetts.

[22] ITP Group, 2010, Reconditioned and Pre-Owned Coordinate Measuring Machines, Retrieved January 11, 2010, from ITP group web site, http://www.itpgroup.co.uk/products/reconditioned_cmms/reconditioned_cmms.html

[23] Moylan, S., July 2009, Private communication, National Institute of Standards and Technology.

[24] ISO-230-1:1996, Test Code for Machine Tools, Part 1: Geometric Accuracy of Machines Operating Under No-load or Quasi-Static Conditions, ISO, Geneva.

[25] ASME B5.54-2005, Methods for Performance Evaluation of Computer Numerically Controlled Machining Centers.

[26] Stone, J.A., Zimmerman, J.H., 2010, Index of Refraction of Air, Retrieved January 10, 2010, from NIST website, http://emtoolbox.nist.gov/Wavelength/Documentation.asp

[27] ISO 230-6:2002, Test code for machine tools, Part 6: Determination of Positioning Accuracy on Body and Face Diagonals (Diagonal Displacement Tests), ISO, Geneva.

[28] New Way Air Bearings, 2006, Air Bearing Application and Design Guide, Retrieved January 10, 2010, from New Way Air Bearing web site: http://www.newwayairbearings.com/Detailed-Product-Information

[29] Devitt Machinery Company, 2010, Moglice: Moldable Bearing Material, Retrieved, January 11, 2010, from website, http://www.moglice.com

[30] New Way Air Bearings, 2010, Product Line Comparison: *Flat Round Air Bearings*, Retrieved January 10, 2010, from New Way Air Bearing web site: http://www.newwayairbearings.com

[31] ETEL S.A., 2010, Ironless Linear Motor: ILM06-060, Retrieved January 11, 2010, from ETEL web site, http://www.etel.ch/documents/showFile.asp?ID=2005

[32] Vierck, R.K., 1979, Vibration Analysis (2nd Edition), Harper & Row.

[33] Banks, C., 2007, Fourth year design report, High Precision Linear Motor Coupling, University of Waterloo, Waterloo, Canada

[34] Thompson, D.C., 1989, The Design of an Ultra-Precision CNC Measuring Machine, Annals of the CIRP, 38/1:501-504

[35] Okwudire, C., Ph.D. Thesis: Modeling and Control of High Speed Machine Tool Feed Drives. University of British Columbia, Vancouver, Canada.

[36] Franklin, G., Powell, J.D., Emami-Naeini, A., 2005, Feedback Control of Dynamic Systems, (5th Edition), Prentice Hall.

[37] Weng, M.-C., Lu, X., Trumper, D.L., 2002, Vibration Control of Flexible Beams using Sensor Averaging and Actuator Averaging Methods. IEEE, Trans. On Control Systems Technology, 10/4:568-577.

[38] Skogestad, S., Postlethwaite, I., 2005, Multivariable Feedback Control – Analysis and Design (2nd Edition), Wiley.

[39] ISO 230-2:2006, Test Code for Machine Tools. Part 2. Determination of Accuracy and Repeatability of Positioning of Numerically Controlled Axes, ISO, Geneva